UNIVERSITY OF COPENHAGEN
FACULTY OF SCIENCE

Master thesis

Sif Fugger

Design and characterization of nano-mechanical quantum photonic devices

Advisors: Prof. Leonardo Midolo and Prof. Peter Lodahl

Handed in: October 15, 2021

Acknowledgements

The work presented in this master thesis is the result of research conducted in the laboratory of the Quantum Photonics group headed Professor Peter Lodahl, at the Niels Bohr Institute.
This project was initiated and led by Professor Leonardo Midolo who has been an amazing supervisor. I have learnt so much during this project under his guidance and I am very grateful for his support and inspiration. I would also like to thank Professor Peter Lodahl for the incredible opportunity to work in his lab during my master project.
My gratitude goes to Xiaoyan Zhou for her co-supervision for the first half of my project and her useful discussions about my simulations and help in designing the nano-mechanical phase shifters and setup to characterise them. I am grateful to Zhe Liu for fabricating the chips investigated in this project in the cleanroom facilities at the H.C.Ørsted institute and for showing me how to take SEM images of them. I would further like to thank Camille Papon for helping me the with wire bonding of the chips and for her continuous availability for my questions regarding daily work in the laboratory. I would like to thank Beatrice da Lio for the many hours she has spent working with me in the laboratory to get the setup working to successfully characterise the devices on the chip. Her contributions and our discussions have been invaluable to this project. I would like to also thank Rodrigo Thomas and Nicolas Høegh Pedersen for helping me in collecting and analysing data from their modified setup. I wish them all the best in their pursuit of further developing a nano-mechanical unitary gate!
I am grateful to my fellow master project students Carlos Faurby and Celeste Qvotrup for their encouragement, insightful discussions and good times during our weekly master project meetings. I would also like to thank the rest of the Quantum Photonics group for their suggestions and discussions during the group meetings and for being so welcoming towards me in the lab.
Lastly, I would like to thank my parents for doing their best to support me all the way from England during these strange covid times and my boyfriend João who has been a source of constant moral support through this past year and a half.

Abstract

Quantum computing requires the ability to generate, manipulate and detect many optical qubits simultaneously. In current free space setups, this is challenging as they are slow, expensive and large. Photonic integrated circuits are a much superior alternative platform for scalable quantum information processing as they are much smaller and efficient. These circuits are built on chips which contain Indium Arsenide quantum dots (QDs) which produce single, highly indistinguishable photons when cooled down to cryogenic temperatures (10K). It has been demonstrated that by embedding these QDs in Gallium Arsenide nanostructures the emissions of single photons from the QDs become near deterministic. To further manipulate emitted single photons and perform more advanced quantum protocols, ways to control and reconfigure the optical components of the photonic integrated circuits require switches and quantum gates which are compatible with cryogenic temperatures.

This project investigates how nano-opto-electro-mechanical systems (NOEMS) could be used to create a compact unitary gate which can be integrated onto the same chip as the source. Nano-opto-electro-mechanical systems are advantageous to other possible nano scale structures for controlling photons such as thermo-optical systems as they use a voltage, rather than thermal heat which makes them thermally compatible with QDs. The unitary gate proposed in this project consists of two cascaded directional couplers, one of which consists of two identical evanescently-coupled parallel waveguides and one which consists of two evanescently-coupled parallel waveguides with different waveguide widths. This project proves that theoretically, by changing the waveguide separation of the two directional couplers, a qubit can be rotated to any position on a Bloch sphere. This project also works towards the realization of this unitary gate by simulating and testing directional couplers which consist of waveguides with different waveguide widths to investigate to what extent such a device can work as a nano-mechanical phase shifter. This work demonstrated that a phase shift that was statistically different from phase drift could be measured with a novel optical setup when a range of 7V was applied to the chip. It also highlighted how the design of the nano-mechanical phase shifter could affect the range of phase shifts it could achieve and describes how the parameters of the design can be optimised.

Lastly, this project calls attention to the effects of fabrication errors on the ability to predict the phase shift achieved by a phase shifter using a 2D COMSOL simulation based on coupled-mode theory. It exemplifies the necessity for a 3D model which takes into account non-uniformity and loss to better predict the behaviour of the nano-mechanical phase shifter and, in due course, a unitary gate.

Contents

Chapter 1

Introduction to the project

This chapter lays out the aims of this project and introduces the concept of quantum information processing on a chip. Specifically, this chapter focuses on introducing how nano-opto-electro-mechanical systems can be used to control interactions between photons in a quantum circuit by routing photons.

1.1 Quantum photonic integrated circuits

In past few decades, the focus of quantum photonics research has been on how quantum photonics can be practically implemented for applications such as quantum cryptography or boson sampling. If successful, this could potentially surpass any current technology that uses classical processors [1]. To move towards this goal, just as classical processors require integrated circuits that depend on microelectronics to process classical bits of information, quantum photonic processors need an analogous integrated circuit to process quantum bits of information (qubits). Qubits are two-level systems that are used as fundamental bits of information in quantum computing and quantum communication. They differ from bits used in classical computing by not being binary and can be in a superposition. This is very useful for speeding up the computation of simulations of quantum systems and also for encrypting information in a solid-state or hybrid quantum network. In quantum photonics, single photons fulfil the role of qubits. Photons are ideal candidates for the job because (i) they can be indistinguishable, (ii) their spin states can be used to store information, (iii) they can travel between nodes in a network at room temperature and (iv) they are also robust to decoherence. Unitary gates are another essential component for a quantum photonic integrated circuit to do quantum computing. This is because they can perform arbitrary rotations of qubits, leading to the development of truly scalable unitary gates for multi-mode interference, entanglement generation, and ultimately quantum simulation. In 1994, Reck and Zeilinger published a paper stating that it was possible to create a unitary gate in an experimental set-up consisting only of beam splitters and phase shifters [2]. To underpin this statement, they demonstrated an algorithmic proof that any discrete finite-dimensional unitary gate can be constructed in a laboratory using optical devices. The project in this thesis aims to demonstrate that if these optical devices were scaled down in size, then they could form a unitary gate which could be integrated into a quantum photonic circuit which could, as a result, be scaled up to include multiple unitary gates to control the states of multiple qubits and create a multi-photon state. The rest of this chapter aims to

explain the theory behind the different components, which would facilitate the realization of a unitary gate which could be integrated along with a single-photon source into a single chip possible.

1.1.1 Aim of this project

This project aims to move towards the goal of realizing a photonic unitary gate that can be reconfigured in real-time using mechanical motion to change the waveguide separation between two coupled waveguides.

To achieve this goal, this project has two main objectives:

- Modelling and optimizing different components of the unitary gate using coupled-mode theory.
- Characterization of the optical response of a fabricated nano-mechanical phase shifter.

The unitary gate which this project works towards developing consists of two cascading directional couplers. The first of these directional couplers consist of two identical parallel waveguides (symmetric) and the second of two parallel waveguides of different widths (asymmetric). The nano-mechanical photon router acts as a beam splitter and the asymmetric one as a phase shifter. The main focus of this project has been on examining the properties of the asymmetric directional coupler as a phase shifter. Whilst phase shifters that rely on thermal heat to change the phase of qubits already exist, [3] they have a flaw that is overcome with the phase shifter developed in this project. The flaw is that the thermo-optical phase shifters have to be kept separate from the source of indistinguishable single photons as they are thermally incompatible, which affects its efficiency. This is because the thermo-optical phase shifter requires heat to work and the emitter of single photons (in this case QDs) must be kept at a temperature of 10K[4] to behave as an artificial atom and emit single photons. The phase shifter being developed in this project relies on voltage controlled mechanical motion rather than heat, to change the phase of the photons, which means it can be integrated on the same chip as the QDs as it can be controlled at cryogenic temperatures and thus is more efficient than thermo-optical phase shifters. This thesis is divided into 6 chapters. The first of which contains background theory relevant to understanding the project, including what nano-opto-electro-mechanical systems are. The second chapter explains the principles of how an asymmetric directional coupler works as a phase shifter and how one could theoretically cascade one with a nano-mechanical photon router to create a reconfigurable unitary gate. The third chapter contains the results of simulations used to optimise the designs of the asymmetric directional couplers tested in this thesis and those from simulations run to test the theory behind the method used to extract the phase shift produced by the asymmetric directional coupler. Chapter 4 contains a short description of how the chips containing the devices for investigations were fabricated and a description of the experimental setup used to conduct the different tests made in this thesis to characterize the devices and measure the phase shift they produced. Chapter 5 outlines the measurement results obtained using the experimental setups explained in Chapter 4 and also describes how the data obtained in these measurements were analysed and discusses what their pitfalls were. The final chapter contains the measurement results which were

conducted on an improved version of the phase shift measurement setup after the results obtained and shown in chapter 5, and a summary plan for how to pursue the development of a unitary gate that can be integrated on the same chip as a single-photon source.

1.1.2 Quantum dots-an example of a single-photon source

Quantum dots (QDs) are small semiconductors. Figure 1.1 shows an illustration of the structure of a self-assembled InAs/GaAs QD and an example of a simple photoluminescence experiment. For simplicity, for the rest of this thesis, InAs/GaAs QD will be referred to as QDs. Figure 1.1 illustrates that a QD consists of many atoms, in fact, they typically consist of 10^5 atoms [5]. The Stranski-Krastanov method is the most commonly used procedure to make QDs. This method involves the self-assembly of InAs QDs on a GaAs substrate [4]. To protect the QDs from oxidation and prevent interaction with surface states, another GaAs layer is grown on top of the InAs. As the InAs has a 7 % larger lattice constant than GaAs, only a thin wetting layer of InAs can be placed on the GaAs substrate before the strain is relaxed by the nucleation of QDs, in the form of randomly positioned islands which can also be seen in Figure 1.1 part (a).
QDs have optical and electronic properties similar to that of a single atom because of the quantum containment of electrons to a nanometer length scale [6]. Thus, like single atoms, they emit coherent single photons with a narrow linewidth when cooled down to temperatures of 4 K or lower. At higher temperatures, thermal depopulation occurs, and the QD no longer acts as an 'artificial atom'. Because they are solid state emitters, they are ideal for integration with photonic nanostructures. By implementing the QDs inside the photonic nanostructures, one can more effectively enhance and control the single photons released by the QD and hence also the light-matter interactions they may be involved in as they can ensure that the photons preferentially couples to one well-defined optical mode [6]. There are many different types of nanostructures; the ones relevant for this project are called directional couplers, which are an example of a nano-opto-electro-mechanical system as explained in section 1.2.

1.2 Nano-opto-electro-mechanical systems (NOEMS)

NOEMS are structures made of photonic materials, which are designed to maximise both the opto-mechanical and electro-mechanical interactions at the nanoscale simultaneously [10]. These different electrical, mechanical and optical effects stem from the intrinsic properties of the materials they are made of and hence, by influencing one of these effects one can affect the other degrees of freedom. As an example, one can consider the change in the electric-optical effect which occurs when an electric field is applied to the structure. The atomic lattice gets deformed and hence induces a change in the refractive index of the same structure due to the photo-elastic effect. Figure 1.2 demonstrates the link between the electronic, mechanical and optical properties of the NOEMS and how different forces are used to modify and control different interactions between the different properties.

The optical and electric forces can be calculated from the Maxwell stress tensor, under the assumption that the electric field E and magnetic field B are known everywhere in space and hence there are no moving charges. This is because both forces follow the general theory of

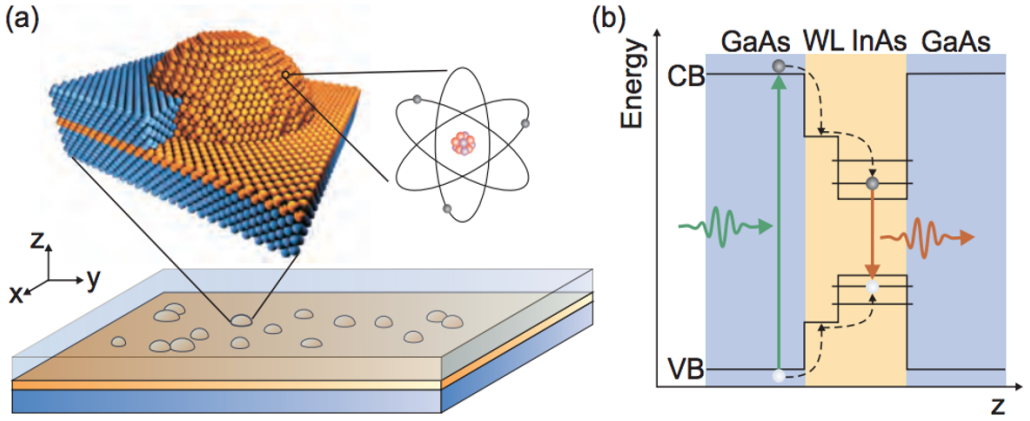

Figure (1.1) (a) This figure shows a self-assembled InAs QD (orange), consisting of thousands of atoms sandwiched between two layers of a GaAs substrate (blue). The QD forms out of the InAs layer (also called the wetting layer) due to a relaxation in the strain caused by the lattice mismatch between the wetting layer and the GaAs layer below the wetting layer. The top GaAs layer protects the QDs from oxidation and also prevents interaction with surface states. The placement of where these QDs form is random and the size of QDs can also vary. (b) This figure illustrates the band structure of a single QD created by the mismatch between the bandgap energies of InAs and GaAs that leads to 3D confinement potential for both electrons and holes. When the QD absorbs a photon (green) which has an energy that corresponds to the energy bandgap between the valence band (VB) and the conduction band (CB), an electron (grey circle) hole (white circle) pair is created. The dotted lines indicate the relaxation process of the electron-hole pair (exciton) where it falls from the conduction band to the ground state of the exciton via nonradioactive processes [7] before the exciton is annihilated through the release of a photon (orange). This optical transition is indicated in the diagram by the orange arrow. This optical transition leads to the QD being a robust, fast and narrow-linewidth source of on-demand photons [8]. These properties make QDs useful as single photon sources for quantum computations and unique as they are not shared by other emitters. This figure is taken from [9]

Lorentz forces. Processing the Maxwell stress tensor, however, requires a numerical analysis. Instead, one can use work-energy formalism to explain how mechanical motion can change the electrostatic or optical field and achieve the following three relations to describe the piezoelectric force, the electrostatic and optical forces respectively:

- $F_{PiezoEL}$: This inverse piezoelectric force can be found by considering the energy stored in a piezoelectric material which is the sum of the dipole energies. This sum is dependent on the distances between the charges in the material.
- $F_{el} = \frac{1}{2}Q\frac{\mathrm{d}V}{\mathrm{d}x}\,|_Q = \frac{1}{2}V^2\frac{\mathrm{d}C}{\mathrm{d}x}$: This electrostatic force is derived from considering the energy stored between two metal plates of an electromechanical capacitor. Here Q is the charge on the plates and V is the voltage between them and C is the displacement-dependent capacitance.
- $F_{optmech} = \frac{U}{L^{eff}}$: Here U is the potential energy and L^{eff} is the effective coupling length [11] which is defined as $L^{eff} = \left|\frac{1}{\omega}\frac{\mathrm{d}\omega}{\mathrm{d}x}\right|^{-1}$ where ω is the electromagnetic resonance frequency.

There are several advantages to using NOEMS, for the purposes of controlling the propagation of light. These include:

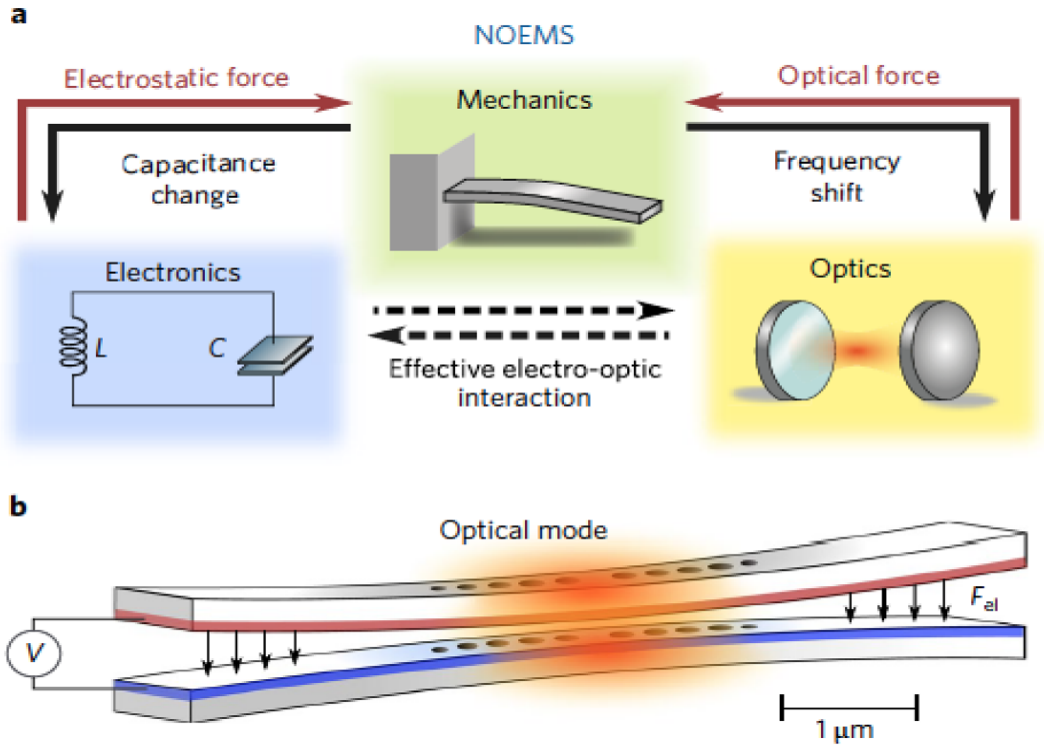

Figure (1.2) (a) This figure illustrates the three degrees of freedom which a NOEMS contains and the direct and inverse effects which are shared between them.(b) This figure contains an artist's interpretation of what a NOEMS looks like. It demonstrates the electrostatic forces F_{el} between two electrodes, along with the optical forces in coupled subwavelength waveguides, couple charges and the mechanical displacement and the optical field. This figure is taken from [10].

- They can control the flow of light in nanophotonic structures, at high speed.
- Due to their nanoscale, have more substantial opto-electro-mechanical effects compared to larger opto-electro-mechanical systems which makes them capable of being used e.g. sensing, signal transduction and optical routing independent of their intrinsic electro-optic coefficient.
- Due to their scale being reduced compared to larger structures, the voltage required to drive the structure is also greatly reduced as the electrostatic forces scales inversely with the square of the charge separation. This means low power consumption.
- By taking advantage of the bulk piezo-electric and photo-elastic effects, it is possible to control the mechanical response. Thus, in the presence of distributed forces, a solid system responds with a deformation which is linear for small deformations (strain within a few per cent).
- NOEMS have the potential for highly efficient, low-noise transducers between microwave and optical signals, in both the classical and the quantum domains [10].

The NOEMSs designed and fabricated in this project consist in part of two parallel and evanescently coupled nanophotonic waveguides which have different widths. The optical modes which these waveguides support have a coupling constant which depends on the waveguide separation distance. As discussed in section 1.2, this distance can be changed by

applying a voltage across the electrodes to which the waveguides are tethered to as shown in Figure 4.1. The theory behind why this type of NOEMS acts as a phase shifter is explained in section 2.2.

1.2.1 Nano-mechanical photon router

Why does this work as a beam splitter?

It has been previously successfully demonstrated that a directional coupler, consisting of two identical nanophotonic waveguides can route single photons [12]. Figure 1.3 shows a SEM picture of a nano-mechanical photon router and how it would be ideally integrated as an on-chip quantum node in a larger quantum circuit such as a demultiplexing scheme. The advantage of using electrically controlled switches rather than thermo-optical switches appears from Figure 1.3 as it shows how an electrically controlled switch can still be operated when integrated on the same chip as a QD. This is contrary to thermo-optical switches which are not thermally compatible with QDs as they cannot be operated at the low temperatures (10K) needed for a QD to produce single photons.

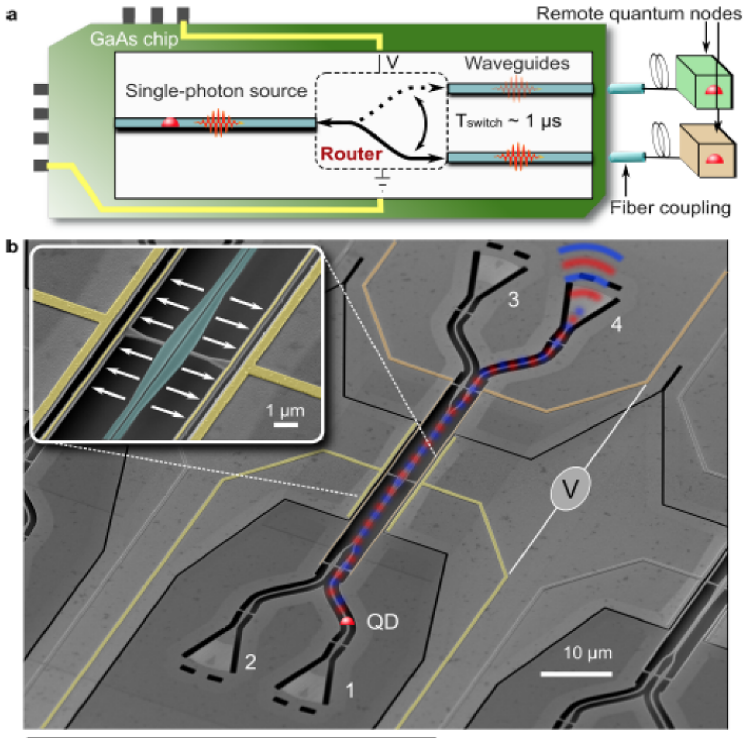

Figure (1.3) (a) This figure illustrates how an on-chip quantum node, based on a quantum emitter integrated with a fast single-photon router could be part of a greater quantum circuit consisting of multiple quantum nodes. (b) A false-colour scanning electron micrograph of nano-mechanical photon router which is demonstrated to act as a single photon router. The yellow lines highlight the position of the electrodes to which the parallel, nanophotonic waveguides are tethered and which, by applying a voltage (V) across, deform the distance between the waveguides as shown in the inset. In this way, the coupling between the two waveguides is changed and hence also the routing of the single photons emitted by the QD which lies inside the directional coupler. The QD is represented as a red spot and the optical electric field emitted from it is overlaid on the figure. The white numbers 1 and 2 indicate the input ports and 3 and 4 the output ports of the directional coupler.This figure is taken from [12].

Before cooling down the chip to 10K, [12] demonstrated, with the use of a CTL laser, that the devices were able to reconfigure the splitting ratio (SR) of the light being emitted out of the directional coupler when the size of the gap separating the waveguides was modified. Figure 1.4 demonstrates how, at different applied voltages, the SR is changed at the output ports T and R as a result of the different voltages displacing the waveguides by different quantities. To explain why changing the gap size of a symmetrical directional coupler changes the SR of the light and hence why it can be used as a tunable beam splitter (and single-photon router), one can look at coupled-mode theory [13].

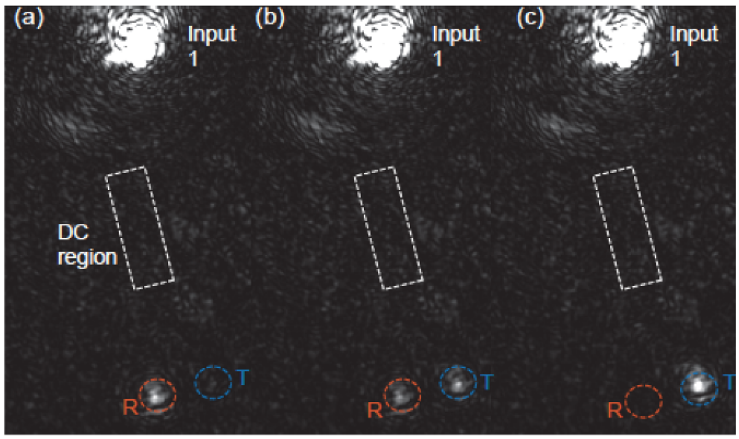

Figure (1.4) This figure shows a series of snapshots taken with a CCD camera used to observe one of the devices on a chip in a cryostat to show the full power transfer between the output ports that one of the fabricated nano-mechanical photon routers can achieve. A CTL laser at the wavelength 940.5nm was focused and coupled through input port 1 (labelled in white in the image) and voltages in the range of 0V to 8V were applied across the electrodes shown in Figure 1.3 to change the coupling across the two waveguides of the directional coupler. (a) Shows that the total power is coming out of output port R of the directional coupler at 0V (b) Shows that the total power coming out of the output ports T and R of the directional coupler is split approximately 50:50 at 5V (c) Shows that the total power is coming out of output port T of the directional coupler at 8V. This figure is taken from Camille Papon's master thesis [14]

Before the directional couplers investigated in Camille Papon's master thesis [14] were fabricated, coupled-mode theory was used as a basis for creating an analytical model to predicted how the SR of a symmetric directional coupler would change as a function of waveguide separation depending on different parameter values such as waveguide width and coupling length. Figure 1.5 illustrates how in the case of a nano-mechanical photon router with a waveguide width of 180nm and coupling length of 15 μm, the transmission through the two output ports (and hence the SR) can be reconfigured by changing the waveguide separation. What is also important to observe from this figure is that in a model, which assumes no loss, the power can be switched from 1:0 to 0:1 meaning that complete power transfer can be achieved between the two waveguides and thus the power in one output port can be made fully extinct. The mathematical basis and coupled-mode theory used in developing such a model are explained in section 2.1. Coupled-mode theory is also used to model the phase shifter properties of the asymmetric directional couplers investigated in this project.

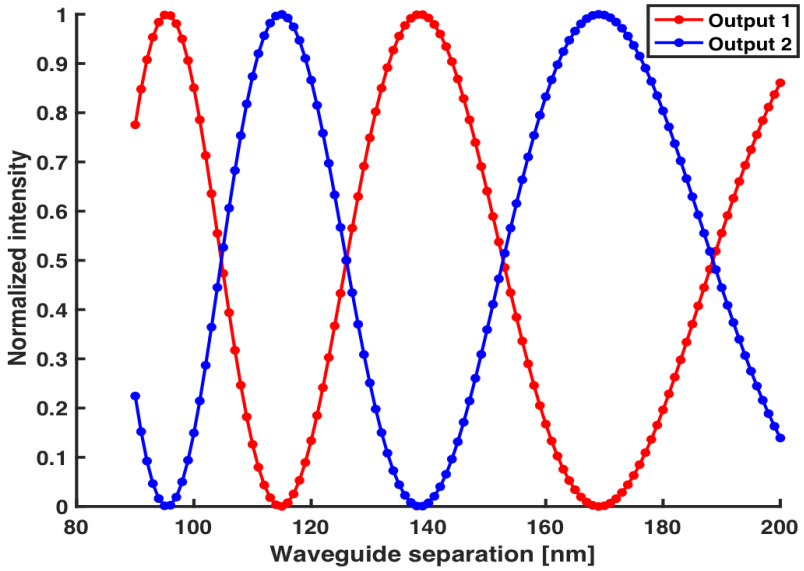

Figure (1.5) This figure shows how the intensity at the two output ports of the nano-mechanical photon router changes as a function of waveguide separation when the input state of the device is kept constant.

1.2.2 TE and TM modes

TE modes are waveguide modes which are dependent on the transverse electric waves which stem from the electric field being transverse to the direction of propagation of the mode. In this case, the magnetic field is always normal to the direction of propagation of the mode [15]. The gratings used in the fabricated devices to couple light in and out of the devices are designed to only allow TE modes through and not TM modes. This is not an issue since the QDs that would be used as single-photon sources, and integrated into the devices have their dipole moment strictly in-plane and as they are also situated in the middle layer of the waveguide, they will only couple to the TE mode anyway. The rate at which the QD couples to the TE mode can be denoted as γ_{wg}. This rate can be used to define the β factor which indicates the strength of the light-matter interactions in a waveguide [16].

Chapter 2

Design principles of a nano-mechanical phase shifter and reconfigurable unitary gate

This chapter explains how coupled-mode theory can be used to create a simulation for calculating the phase shift generated by an asymmetric directional coupler as well as model a unitary gate consisting of a cascaded nano-mechanical photon router and phase shifter which can perform any arbitrary rotation of a qubit.

2.1 Coupled-mode theory

The directional coupler in this project consists of two parallel waveguides which are capable of confining modes of similar phase velocities. This means that if the two waveguides are brought close enough together, the wave can move from one waveguide to the other as there is a significant overlap with the evanescent portion of the wave. This process is called electronic tunnelling [17]. Coupled-mode theory is ideal to describe this process as it is a perturbational approach for analysing the coupling of vibrational systems such as the opto-mechanical directional couplers investigated in this project. To show how coupled-mode theory can be applied, one can begin by looking at two guided modes, one going through each waveguide. Assuming the waveguides to be isolated, the modes can be written as $a_{10}E_1(x,y)e^{-j\beta_1 z}$ and $a_{01}E_2(x,y)e^{-j\beta_2 z}$ for waveguides 1 and 2 respectively. Here β_1 and β_2 are the propagation constants, $E_1(x,y)$ and $E_2(x,y)$ are the fields ,and a_{10} and a_{01} are the amplitudes of the two guided modes. When the two waveguides are brought close together, the fields overlap with both waveguides. This means that the mode $a_{10}E_1(x,y)e^{-j\beta_1 z}$ extends to waveguide 2 and $a_{01}E_2(x,y)e^{-j\beta_2 z}$ to waveguide 1. When the boundary conditions are different for the two waveguides (like in the case of an asymmetric directional coupler), the two modes do not satisfy the boundary conditions of the waveguide they have extended to. Therefore two modes will be perturbed by the waveguides they have extended to. This perturbation becomes weak however if the waveguides are sufficiently close together. Under weak perturbation, the field of the coupled waveguides can be written as:

$$E(x,y,z) \approx a_1(z)E_1(x,y)e^{-j\beta_1 z} + a_2(z)E_2(x,y)e^{-j\beta_2 z} \tag{2.1}$$

Where $a_1(z)$ and $a_2(z)$ are the two amplitude functions. To further define these amplitude functions, they can be rewritten in terms of normal modes. This requires however that instead of regarding the waveguides as isolated from each other, they must be considered as a composite waveguide structure which the modes are guided through. For a nano-mechanical photon router, the two normal modes fields shared by the two waveguides are symmetric and anti-symmetric respective to the centerline through the gap separating the two waveguides. For an asymmetric directional coupler, the mode fields are no longer symmetric and anti-symmetric as can be shown in Figure 2.1. To show how coupled-mode theory can still be used to explain the propagation of light through such a device, the normal modes for an asymmetric directional coupler will be annotated as anti-symmetric and symmetric (i.e a_{a0} and a_{s0}) for simplicity in this chapter. To describe the evolution of a_1 and a_2 as a function of position along waveguide (z), one must obtain a set of differential equations which can be found partly using, the Marcatili relation, as well as considering the wave equation for two isolated waveguides as put forward in chapter 6 of Foundations for Guided-Wave Optics [18]. This section contains a summary of the key points of the derivation of these coupled-mode differential equations which are the key for the construction of the simulations used to design the directional couplers investigated in this project.

The derivation begins by establishing the two wave equations which the two waveguides must satisfy when considered as two isolated waveguides and when considered as a composite structure respectively. Beginning with the case where the two waveguides are considered isolated from each other, waveguide 1, which for this derivation will have its index variation defined as $\delta n_1(x, y)$ (which is different from the index (n) of the medium which the waveguide is inside of), must satisfy the following wave equation with the following boundary conditions:

$$\{\nabla_2^t + 2k^2n^2\delta n_1(x, y) + 2kn(kn - \beta_1)\}e_1(x, y) \approx 0 \tag{2.2}$$

Here, ∇_2^t is the transverse Laplacian operator defined as:

$$\nabla_t^2 = \frac{\partial}{\partial x^2} + \frac{\partial}{\partial y^2} \tag{2.3}$$

And $\delta n_1(x, y)$ is so small everywhere that β_1 is approximately kn. Likewise, for waveguide 2, the same approximation can be made for β_2 and the fields and propagation constants of modes guided through that waveguide can be found using the following equation:

$$\{\nabla_2^t + 2k^2n^2\delta n_2(x, y) + 2kn(kn - \beta_2)\}e_2(x, y) \approx 0 \tag{2.4}$$

Having deduced the propagation constants β_1 and β_2 as well as $e_1(x, y)$ and $e_2(x, y)$ from these wave equations as well as supposing that the fields are normalized so that

$$\int_s e_i(x, y) \cdot e_i(x, y)ds = 1 \tag{2.5}$$

where i= 1 and 2 is true. One can proceed to use these values to find what happens to the field when it travels through a composite structure. In this composite structure, both $\delta n_1(x, y)$ and $\delta n_2(x, y)$ are present at the same time. In this situation $e(x, y)$ and the propagation constant β must satisfy the following wave equation:

$$\{\nabla_2^t + 2k^2n^2[\delta n_1(x, y) + \delta n_2(x, y)] + 2kn(kn - \beta)\}e(x, y) \approx 0 \tag{2.6}$$

This wave equation is difficult to solve so coupled-mode formulation helps to find ways by which $e(x, y)$ and β can be approximated. The Marcatili relation plays a crucial role in this. It is obtained by applying Greens theorem [19] to an integral that is created by integrating the following expression over the entire cross section S of the composite waveguide:

$$\int_S [e_2(x,y) \cdot \nabla_t^2 e_1(x,y) - e_1(x,y) \cdot \nabla_t^2 e_2(x,y))] ds \tag{2.7}$$

and is defined thus:

$$g_1 - g_2 = c(\beta_1 - \beta_2) \tag{2.8}$$

Where g_1 and g_2 are the coupling constants the dictate the coupling through waveguides 1 and 2 respectively and c is the overlap integral. The formal definitions of these three quantities are:

$$g_1 = kn \int_s [\delta n_1(x,y)] e_1(x,y) \cdot e_2(x,y) ds \tag{2.9}$$

$$g_2 = kn \int_s [\delta n_2(x,y)] e_1(x,y) \cdot e_2(x,y) ds \tag{2.10}$$

$$c = \int_s e_1(x,y) \cdot e_2(x,y) ds \tag{2.11}$$

As this project centres mostly around investigating asymmetric directional couplers, it is important to highlight how the mismatch between the propagation constants β_1 and β_2 that arises from the different widths of the 2 waveguides, comes into play in the Marcatili relation. To do this one can begin by defining a mismatch parameter 'd':

$$d \equiv \frac{\beta_1 - \beta_2}{2\sqrt{g_1 g_2}} \tag{2.12}$$

which is half the difference of the propagation constants which has been normalized in respect to the geometrical mean of the two coupling constants g_1 and g_2 of the two waveguides. Using this mismatch parameter, the Marcatili relation can be rewritten as:

$$\frac{g_1}{g_2} = (cd + \sqrt{1 + c^2 d^2})^2 = e^{sinh^{-1} cd} \tag{2.13}$$

It is now clearer that the ratio between the coupling constants is only dependent on the parameters c and d. Due to the design of most directional couplers, the product of c and d is close to zero as either $\beta_1 \approx \beta_2$ or the distance is so great that the overlap integral 'c' is close to zero meaning that g_1 is almost equal g_2. Of interest to this project is if this assumption of $g_1 \approx g_2$ will hold true for the larger asymmetries tested and if this will affect the accuracy of the coupled-mode theory used to predict the evolution of the field inside the directional coupler. This mismatch parameter is useful as well for writing the approximate solution to the wave equation shown in equation 2.6. As stated earlier, the wave equation is very difficult to solve directly so instead, to get an approximate solution one must approximate $e(x, y)$ thus:

$$e(x,y) \approx e_1(x,y) + r e_2(x,y) \tag{2.14}$$

This approximation assumes that the two waveguides are far enough away from each other that the field guided by the composite structure can be written as a linear combination of e_1 and e_2 where r is a parameter which must be defined. Following the derivations in 6.4.3

of chapter 6 in Foundations for Guided-Wave Optics[18], one can see how in solving for r one defines the normal modes r_s and r_a.

$$r_{s,a} \approx \sqrt{\frac{g_1}{g_2}}(-d \pm \sqrt{1+d^2}) \tag{2.15}$$

Where d is the mismatch parameter defined in equation 2.12. Using these roots, the propagation constants of the symmetric and antisymmetric modes can be defined in terms of the mismatch parameter d as well as the propagation constants β_1 and β_2 and the coupling constants g_1 and g_2.

$$\beta_{s,a} \approx \frac{\beta_1 + \beta_2}{2} \pm \sqrt{g_1 g_2 (1+d^2)} \tag{2.16}$$

Using the definitions of the coupling constants and the propagation constants for the symmetric and antisymmetric modes for a composite structure shown in equations 2.9, 2.10 and 2.16 and the definitions of the two normal modes r_s and r_a, the following equation can be written to describe the field being guided through the composite structure:

$$E(x,y,z) \approx a_{s0}[e_1(x,y) + r_s e_2(x,y)]e^{-j\beta_s z} + a_{a0}[e_1(x,y) + r_a e_2(x,y)]e^{-j\beta_a z} \tag{2.17}$$

From here one can get the same equation as in equation 2.1 by defining the amplitude functions $a_1(z)$ and $a_2(z)$ as:

$$\begin{aligned} a_1(z) &= (a_{s0}e^{-j\sigma z} + a_{a0}e^{j\sigma z})e^{j\delta z} \\ a_2(z) &= (a_{s0}r_s e^{-j\sigma z} + a_{a0}r_a e^{j\sigma z})e^{-j\delta z} \end{aligned} \tag{2.18}$$

Where a_{s0} and a_{a0} are the amplitudes of the normal modes and σ is defined as:

$$\sigma = \sqrt{g_1 g_2 (1+d^2)} \tag{2.19}$$

Where again, d is the mismatch parameter defined in equation 2.12. By having a_1 and a_2 defined in terms of the normal modes, it is now possible to describe the evolution of a_1 and a_2 as a function of z, i.e. the progression along the waveguides, by first differentiating a_1 and a_2 with respect to z:

$$\begin{aligned} \frac{\mathrm{d}a_1(z)}{\mathrm{d}z} &= -jg_2 a_2(z)e^{j2\delta z} \\ \frac{\mathrm{d}a_2(z)}{\mathrm{d}z} &= -jg_1 a_1(z)e^{j2\delta z} \end{aligned} \tag{2.20}$$

One can simplify these differential equations by rewriting them in an equivalent form where the terms $a_1(z)e^{j2\delta z}$ and $a_2(z)e^{j2\delta z}$ are equated to $A_1(z)$ and $A_2(z)$ respectively so that they look like so:

$$\begin{aligned} \frac{\mathrm{d}A_1(z)}{\mathrm{d}z} &= -j\beta_1 A_1 - jg_2 A_2(z) \\ \frac{\mathrm{d}A_2(z)}{\mathrm{d}z} &= -j\beta_2 A_2 - jg_1 A_1(z) \end{aligned} \tag{2.21}$$

For a nano-mechanical photon router, the overlap of the evanescent fields from waveguide 1 to waveguide 2 is equal to the overlap of the evanescent field of waveguide 2 to waveguide 1. This means that the coupling constants for each of the waveguides are equal. Using this assumption and that of the uniformity of the two waveguides, and one can simplify the transfer matrix by equating the coupling constants g_1 and g_2 thus [12]:

$$g_1 = g_2 = g = g_0 e^{-\kappa d_1} \tag{2.22}$$

Here g_0 denotes a constant that is dependent on the different properties associated with one isolated waveguide, κ denotes the photon tunnelling constant of the evanescent mode in the gap region between the two parallel waveguides and is defined as

$$\kappa = \sqrt{\beta^2 - 1} \tag{2.23}$$

where β here is the propagation constant of an individual waveguide (which is the same for both waveguides in this case as they are identical) and lastly, d_1 is the waveguide separation between the two waveguides. Having explained how the coupling constant g is defined in the case of a nano-mechanical photon router, it can now be shown how the transfer matrix can be rewritten and applied to A_1 and A_2.

$$\frac{\partial}{\partial z}\begin{bmatrix} A_1 \\ A_2 \end{bmatrix} = -j \cdot \begin{bmatrix} \beta_1 & g \\ g & \beta_2 \end{bmatrix} \cdot \begin{bmatrix} A_1 \\ A_2 \end{bmatrix} \tag{2.24}$$

This same matrix can be also written in this way in the case of an asymmetric directional coupler, though it is necessary to define g differently as β_1 and β_2 are no longer equivalent. The method by which the coupling constant is defined and calculated in the case of the asymmetric directional coupler for this project is explained in the following section. In this same section, it is also shown how the phase shift induced by changing the waveguide separation is found using the transfer matrix derived from the coupled-mode theory introduced in this section.

2.2 An asymmetric directional coupler as a nano-mechanical phase shifter

To explain how an asymmetric directional coupler creates a phase difference between the two output ports of the directional coupler, it is important to consider the splitting of the modes passing through the directional coupler into symmetric and antisymmetric supermodes. Figure 2.1 illustrates what these two supermodes, which originate from the overlap of the evanescent field of one waveguide with the other, looks like in a directional coupler. Figure 2.1 part (a) and (b) show the results of a 2D COMSOL model of an asymmetric directional coupler with an asymmetry of 1.25nm. In this example, the field in the narrower waveguide is less contained in the waveguide than in the wider waveguide. This explains why for an asymmetric directional coupler, there does not exist perfectly symmetric and antisymmetric modes as the amplitudes of the modes in the two waveguides are not equal. For simplicity, these modes are still referred to as the symmetric and antisymmetric modes of an asymmetric directional coupler. Due to their different widths, these two waveguides have different propagation constants, β_1 and β_2. According to coupled-mode theory, by knowing the values of these propagation constants along with the coupling constant g, one can calculate the wave fields at the output of the directional coupler in accordance with the following matrix equation:

$$\begin{bmatrix} a_{1out} \\ a_{2out} \end{bmatrix} = \begin{bmatrix} \beta_1 & g \\ g & \beta_2 \end{bmatrix} \begin{bmatrix} a_{1in} \\ a_{2in} \end{bmatrix} \tag{2.25}$$

The values of β_1, β_2 and g used to solve this equation are found using a COMSOL simulation of the asymmetric directional coupler which calculates the β_1, β_2, β_S, β_{AS} of the device.

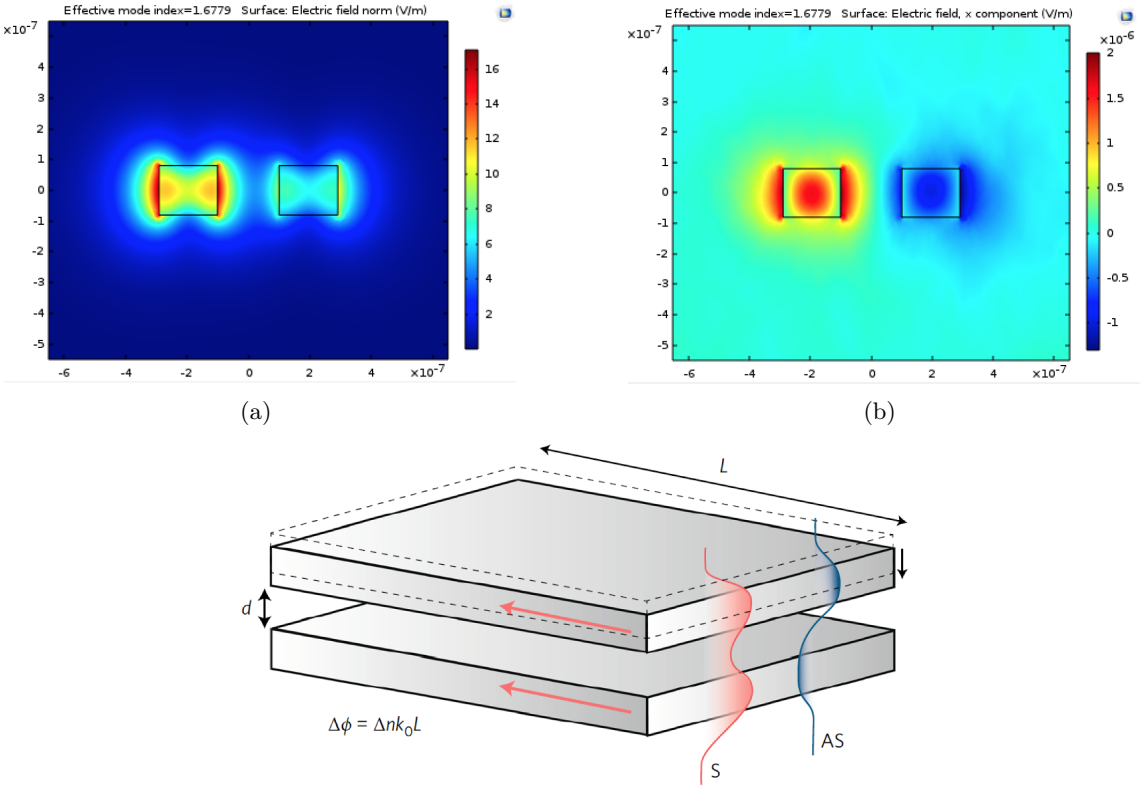

(a) (b) (c)

Figure (2.1) (a) This figure shows the symmetric mode from a 2D COMSOL model of an asymmetric directional coupler. (b) This figure shows the antisymmetric mode from a 2D COMSOL model of an asymmetric directional coupler.(c) This figure shows the symmetric (red S) and antisymmetric (blue AS) modes which originate from the evanescent coupling of the individual waveguides. L is the length of the two waveguides and d is the waveguide separation. The equation $\Delta\phi = \Delta n k_0 L$ shows the relation between the change in phase ($\Delta\phi$) and the change in effective index (Δn) of the directional coupler. The constant k_0 is the wavenumber in vacuum. Δn is controlled by changing the size of 'd' electro-mechanically. This is because d determines the overlap of the evanescent field between the two waveguides and hence also the coupling strength and the difference in the propagation constants between the modes. This figure is taken from [10]

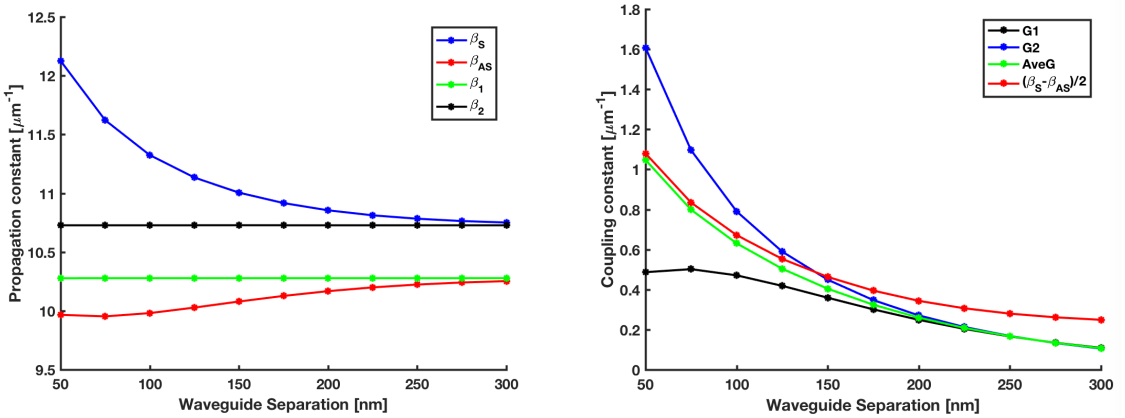

(a) (b)

Figure (2.2) (a) This figure shows the different propagation constants found by using a COMSOL 2D simulation to simulate an asymmetric directional coupler with the parameters: waveguide widths= 180nm and 184nm, coupling length= 30 μm. The propagation constants of the symmetric (β_S) and the anti-symmetric (β_{AS}) modes, as a function of waveguide separation, are plotted as blue and red dots respectively with a line connecting the respective dots as a guide for the eye. The propagation constants for the two waveguides of different widths, β_1 and β_2 are also plotted, as a function of the waveguide separation, as green and black dots respectively with a line of the same colour connecting them as a guide for the eye. In the simulation the wavelength of the light passing through the device was 945nm. (b) In this figure, the coupling constants G1 and G2 found from solving the equation 2.26 are plotted as black and blue lines respectively as a function of waveguide separation. The coupling constant used to simulate the behaviour of the asymmetric directional coupler as a function of waveguide separation is found by taking the average of G1 and G2 for each different waveguide separation and is plotted as the green line on this plot. The red line on the plot shows the coupling constant one would get as a function of waveguide separation when the same approximation for the coupling constant used in [12] was used.

Here β_S and β_{AS} are the propagation constants of the symmetric and antisymmetric modes. The values of these constants, as a function of waveguide separation for an asymmetric directional coupler are plotted in Figure 2.2 part (a). Because β_1 is no longer equal to β_2, it is more complicated to determine the value of g. Because when solving the matrix, one ends up with two eigenvector equations rather than one. For this project, therefore, the g used for modelling the change in phase as a function of waveguide separation was calculated by taking the average of the two values of g found by solving the two equations below, where the β values stem from the 2D COMSOL simulation at a given waveguide separation:

$$T = \begin{bmatrix} \frac{\beta_2}{2} + \frac{\beta_1}{2} - \frac{\sqrt{\beta_1^2 - 2\beta_1\beta_2 + \beta_2^2 + 4g^2}}{2} & 0 \\ 0 & \frac{\beta_2}{2} + \frac{\beta_1}{2} + \frac{\sqrt{\beta_1^2 - 2\beta_1\beta_2 + \beta_2^2 + 4g^2}}{2} \end{bmatrix} = \begin{bmatrix} \beta_{AS} & 0 \\ 0 & \beta_S \end{bmatrix} \quad (2.26)$$

The diagonal eigenvalue matrix here is labeled as T to simplify the notation of this matrix when it is inserted into the transfer matrix which is used to calculate the phase difference between the output ports which the asymmetric directional coupler generates. Figure 2.2 part (b) shows how the g values generated by the 2D COMSOL simulation change as a function of waveguide separation and how the average g value compares to the approximation that can be used for the coupling constant of a symmetrical directional coupler. In the MatLab script, after the 2D COMSOL model has generated the required propagation and

coupling constant, one can rewrite the equation 2.25 thus:

$$\begin{bmatrix} a_{1out} \\ a_{2out} \end{bmatrix} = Q^{\dagger} \cdot H \cdot Q \begin{bmatrix} a_{1in} \\ a_{2in} \end{bmatrix} \tag{2.27}$$

Here the matrix Q and its transpose are used to change the basis and back from a basis where the projected modes evolve independently with their eigenvalues given by T. Hence in this basis, one can use the diagonal matrix H to calculate the evolution of the system over the coupling distance which here is defined as L. Matrix H is thus defined as:

$$H = \begin{bmatrix} e^{-i \cdot T_{11} \cdot L} & 0 \\ 0 & e^{-i \cdot T_{22} \cdot L} \end{bmatrix} \tag{2.28}$$

Matrix Q is the eigenvector matrix of the matrix defined in equation 2.25 and is shown below in terms of β_1, β_2 and g.

$$Q = \begin{pmatrix} -\frac{g}{\sqrt{\beta_1^2 - 2\beta_1\beta_2 + \beta_2^2 + 4g^2}} & \frac{\sqrt{\beta_1^2 - 2\beta_1\beta_2 + \beta_2^2 + 4g^2} + \beta_1 - \beta_2}{2\sqrt{\beta_1^2 - 2\beta_1\beta_2 + \beta_2^2 + 4g^2}} \\ \frac{g}{\sqrt{\beta_1^2 - 2\beta_1\beta_2 + \beta_2^2 + 4g^2}} & \frac{\sqrt{\beta_1^2 - 2\beta_1\beta_2 + \beta_2^2 + 4g^2} - \beta_1 + \beta_2}{2\sqrt{\beta_1^2 - 2\beta_1\beta_2 + \beta_2^2 + 4g^2}} \end{pmatrix} \tag{2.29}$$

By taking the modulus square of the output fields, one can define the intensity at the two outputs thus:

$$\begin{aligned} Int_3 &= \left| a_{1out}^2 \right| \\ Int_4 &= \left| a_{2out}^2 \right| \end{aligned} \tag{2.30}$$

These intensities are plotted in Figure 2.3, for two different asymmetries in part (a) (2nm) and part (b) (4nm). The purpose of these plots is to demonstrate how the beam splitter properties decrease with an increase in asymmetry, as well as waveguide separation. This can be seen by observing how the maximum transfer of power decreases in both these cases. If the device acted as a perfect tunable beam splitter, it should be able to perform a full transfer of power between the output ports, like the nano-mechanical photon router is capable of as shown in Figure 1.5. The fields at the outputs a_{1out} and a_{2out} are complex numbers which can be written in exponential form like this:

$$\begin{aligned} a_{1out} &= r_1 e^{i\Phi_1} \\ a_{2out} &= r_2 e^{i\Phi_2} \end{aligned} \tag{2.31}$$

Doing so allows for the phase angle to be easily extracted from the two output waves which in this case are denoted as Φ_1 and Φ_2. The phase difference can be found by taking the modulo of the difference of Φ_1 and Φ_2 with 360 as the divisor, assuming that Φ_1 and Φ_2 are in degrees:

$$\Delta\Phi = (\Phi_1 - \Phi_2) \, mod \, 360 \tag{2.32}$$

This phase difference ($\Delta\phi$) is plotted in Figure 2.4 for two different directional couplers with different asymmetries to show how this affects the phase shifter properties of the device as a function of waveguide separation.

2.3 Model of cascaded nano-mechanical photon router and phase shifter as a reconfigurable unitary gate

In this section, the analytical model used to investigate what rotations of a qubit would be possible for a cascaded symmetric and asymmetric directional coupler to achieve is

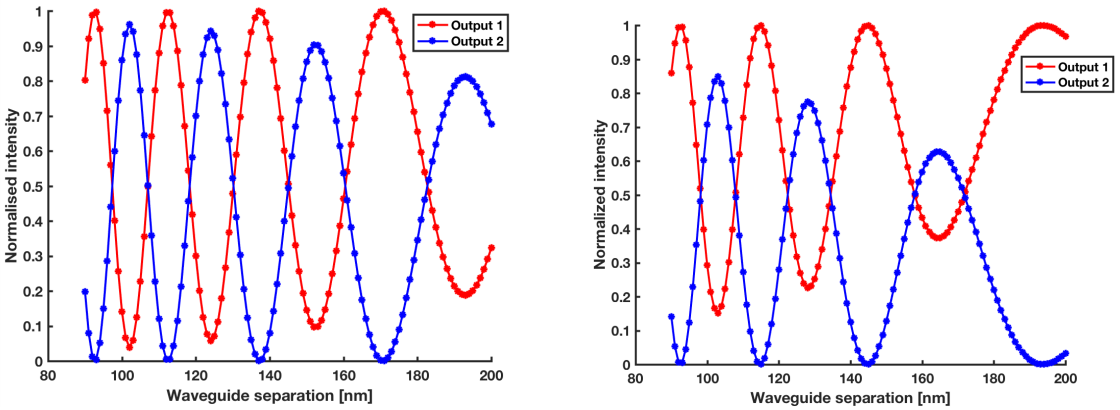

(a) (b)

Figure (2.3) (a)This figure shows how the intensity at the two output ports of the asymmetric directional changes as a function of waveguide separation. The asymmetry of the simulated device used to create this plot was 2nm (b) This figure shows how the intensity at the two output ports of the asymmetric directional changes as a function of waveguide separation. The asymmetry of simulated device used to create this plot was 4nm. As compared to (a), the increase in asymmetry corresponds to a decrease in the beam splitter qualities of the device.

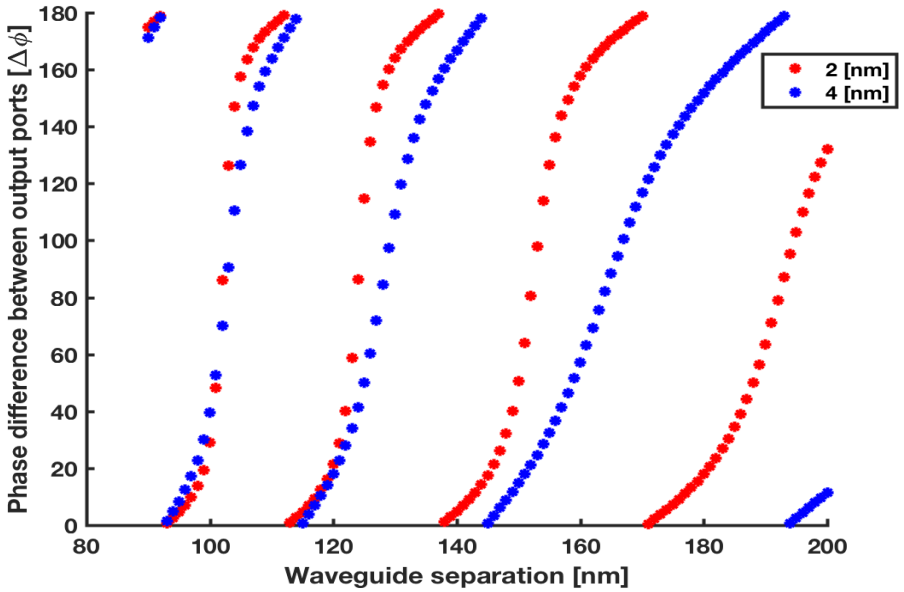

Figure (2.4) This figure demonstrates how the asymmetry of a directional coupler affects the gradient at which the phase difference between the output ports changes as a function of waveguide separation.

discussed. The goal of this investigation was to explore if by varying the combinations of the widths d_1 and d_2 (the respective waveguide separations of the two directional couplers), a qubit could be rotated so as to reach all points on a Bloch sphere. If possible, the device could act as a truly unitary gate and produce any arbitrary rotation of a qubit. Figure 2.5 part (a) shows a schematic diagram of the two cascaded directional couplers which was modelled. L_1 and L_2 are the lengths of the parallel waveguides of the two respective directional couplers which in the model discussed in this section are equal. Using coupled-mode theory, as described in section 2.1, one can obtain the fields at the output of both

a symmetrical as well as an asymmetric directional coupler. To model the unitary gate and how the two parts are cascaded, one combines these two models of the directional couplers into one where the fields being inputted into the asymmetric directional coupler is the fields outputted by the symmetrical directional coupler. The output of the asymmetric directional coupler is thus the result of light passing through both directional couplers. In Figure 2.5 part (b) one can see that by changing the length d_1 the qubit can rotate around the z axis of the Bloch sphere and by changing d_2 one can rotate the qubit around the xy plane. Angle ϕ represents the angle controlled by the asymmetric directional coupler and θ represents the angle represents the angle controlled by the symmetrical directional coupler. The asymmetric directional coupler, depending on its asymmetry, can also affect the angle θ as it still exhibits some beam splitter properties, however, this change in θ can be compensated for with the symmetric directional coupler and can be ignored in the simplified Bloch sphere diagram in Figure 2.5 part (b).

Figure 2.6 shows the results of the model where the widths d_1 and d_2 were varied to test which angles θ and ϕ were achieved for all the possible different combinations of d_1 and d_2 in a range of 80nm to 250nm. The blue and red spots overlaid on the 3D plots of angles θ and ϕ demonstrate which specific combinations of d_1 and d_2 achieve θ angles in the range of 1.5 to 1.55 radians and ϕ angles in the range of 3.1 to 3.13 radians respectively. Figure 2.6 parts (a) and (b) show within this range of d_1 and d_2 tested in the model, it was possible to achieve the full π rotation along the z axis and a 2π rotation along xy plane. These results were hence very encouraging to test if it would be theoretically possible to use a nano-mechanical photon router cascaded with an asymmetric one as an on chip unitary gate which is controlled electrically to mechanically change the waveguide separation of the two directional couplers and achieve any arbitrary rotation in the range of waveguide separation tested.

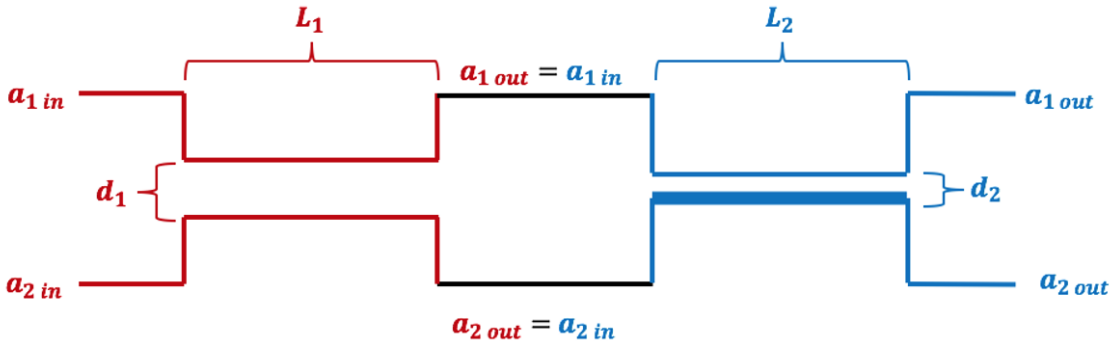

(a)

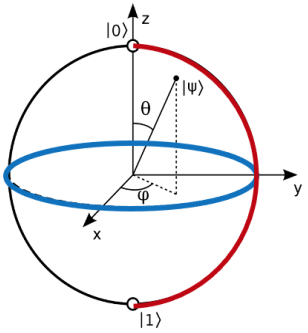

(b)

Figure (2.5) (a) This figure shows a schematic diagram of two cascaded directional couplers, one of which is symmetric (red) and the other is asymmetric (blue). Each of the directional couplers consists of two parallel waveguides which have a distance of d_1 and d_2 between them and length L_1 and L_2 respectively. Each of the directional couplers contains two input and output ports. By being cascaded the output ports of the red directional coupler are also the input ports of the blue directional coupler so that the output state emitted out of the red directional coupler is also the input state of the blue directional coupler. By changing the value of d_1 and d_2 the coupling of the light through the two directional couplers changes. Theoretically, this causes an arbitrary rotation of a qubit. (b) This figure shows a Bloch sphere and demonstrates how the two cascaded directional couplers are used to control the different axes which the qubit state can rotate around. It shows that one requires both of the directional couplers to achieve all arbitrary rotations of a qubit state. Depending on the asymmetry of the asymmetric (blue) directional coupler, the qubit state is rotated along the z axis, along with the xy plane when d_2 is changed as it can exhibit both phase shifter and beam splitter properties. However, in the cascaded model of a unitary gate, the symmetric (red) directional coupler can compensate for this with its own rotation around the z axis. This means that it is only the rotation along the xy plane that the blue directional coupler which is of interest for this project.

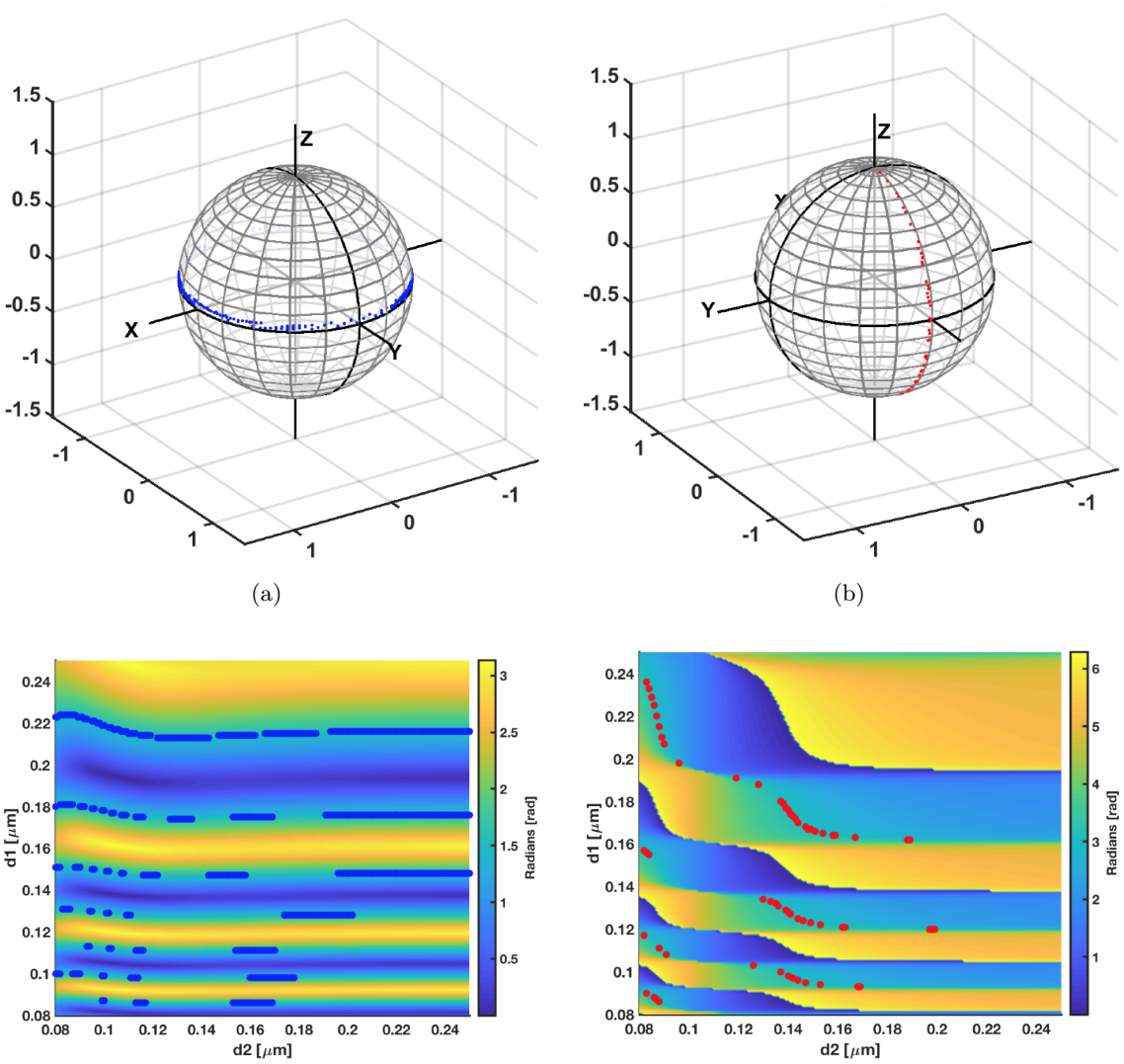

(a) (b)

(c) (d)

Figure (2.6) (a) This figure shows the points on the Bloch sphere, where the combinations of d_1 and d_2 lengths produce a ϕ angle in the range of 3.1 and 3.13 radians. (b)This figure shows the points on the Bloch sphere, where the combinations of d_1 and d_2 lengths produce a θ angle in the range of 1.5 and 1.55 radians. (c) This 3D plot shows the size of angle ϕ achieved by different combinations of d_1 and d_2. The blue stars indicate the d_1 and d_2 widths which achieve a ϕ angle that lies between 3.1 and 3.13 radians. (d) This 3D plot shows the size of angle θ achieved by different combinations of d_1 and d_2. The red stars indicate the d_1 and d_2 widths achieve a θ angle that lies between 1.5 and 1.55 radians

Chapter 3

Simulations

Before fabricating the asymmetric directional couplers, the design parameters were optimised using a COMSOL model to determine how to obtain a full pi phase shift between the light coming out of the two output ports. The goal was to achieve this phase shift within a range of waveguide separations which was neither too long nor too short to be able to observe the gradual change in phase as a function of waveguide separation in a phase shift measurement. It was also important to test how flexible the choice of the design parameters could be and still observe a full pi phase shift with the device. That is what this chapter will discuss as well as explain how the simulations of the method for measuring the phase shift produced by the devices fabricated in this project were constructed.

3.1 Optimization of parameters

Several parameters can be taken into consideration when trying to optimise an asymmetric directional coupler. In this project the parameters that were focused on were:

- The asymmetry of the two waveguides that make up the directional coupler
- the coupling length of the waveguides
- the relative width of the two waveguides

The focus was on these three parameters because they were thought to have the greatest effect on what phase shift the device would produce. Other parameters such as the shuttle width have already been optimised in previous projects [14]. Figure 3.1 shows how the phase difference between the two output ports changes with the intensity at one of the output ports as a function of waveguide separation. It shows how the phase shifter properties of the asymmetric directional coupler are related to its beam splitter qualities. To achieve a full pi phase shift, the intensity of the light at one output port must undergo a cycle switching. A full cycle consists of first having the input light coupled to maximise the intensity at one of the output ports. The waveguide separation is then changed by applying a voltage to the device which causes the coupling between the two waveguides to change and thus also the intensity of the light at the two outputs. The cycle ends when the intensity is once again maximum at the output port where it was at the beginning of the cycle. Because of this relationship, when choosing the parameters to fabricate the device, it is important to

consider how the asymmetry of the directional coupler will affect the beam splitter properties of the same directional coupler. This is because the more asymmetric the device, the greater the range of waveguide separation will be needed to complete a switching cycle of the output light and hence therefore also the range needed to get a full pi phase shift. The larger the waveguide separation range needed, the more voltage is needed to reach a full pi phase shift. This may conflict with the realistic ranges of voltage that can be applied to the device within a reasonable period of time where the asymmetric directional coupler would be efficient as a phase shifter. In contrast, if the device is not asymmetric enough, then the range of waveguide separation needed to achieve a full pi shift may be so small, that a gradual change in phase shift with small changes in voltage applied to the device will not be possible. This would reduce the range of rotations which could be done to a qubit if such an asymmetric directional coupler was used in a unitary gate.

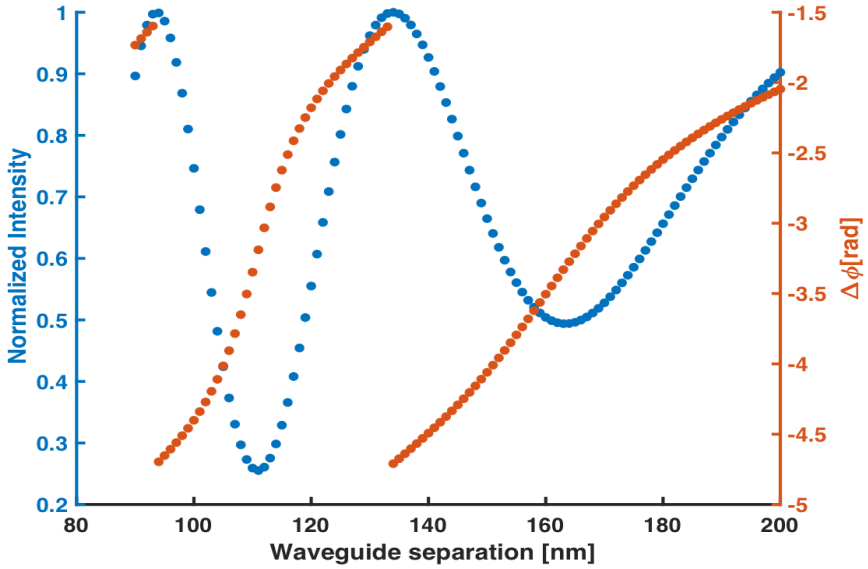

Figure (3.1) A plot showing the normalized intensity at output port1 as a function of waveguide separation (blue) and the phase difference between the two output ports as a function of waveguide separation (red)

Figure 3.2 illustrates the relationship between the asymmetry of the two waveguides and the range of waveguide separation needed to obtain a full phase shift. In the simulations that produced this plot the coupling lengths of the waveguides were kept the same (20 μm). The width of waveguide 1 was also kept the same throughout the different simulations (200nm), it is only waveguide 2 which changed in width to change the asymmetry of the device. From Figure 3.2 one can ascertain that an asymmetry between 1nm and 3nm results in a waveguide range that would be reasonable for a fabrication. This flexibility in which asymmetry allows for a reasonable range of waveguide separation is advantageous for fabrication purposes as errors in this process can result in the asymmetry being different from the design parameters.

To test how the coupling length of the two waveguides affected the range of waveguide separation needed to achieve a full pi phase shift, a simulation of an asymmetric directional coupler with an asymmetry of 3nm was repeated for varying coupling lengths. The resulting phase shifts are plotted in Figure 3.3 as a function of waveguide separation. It appears that

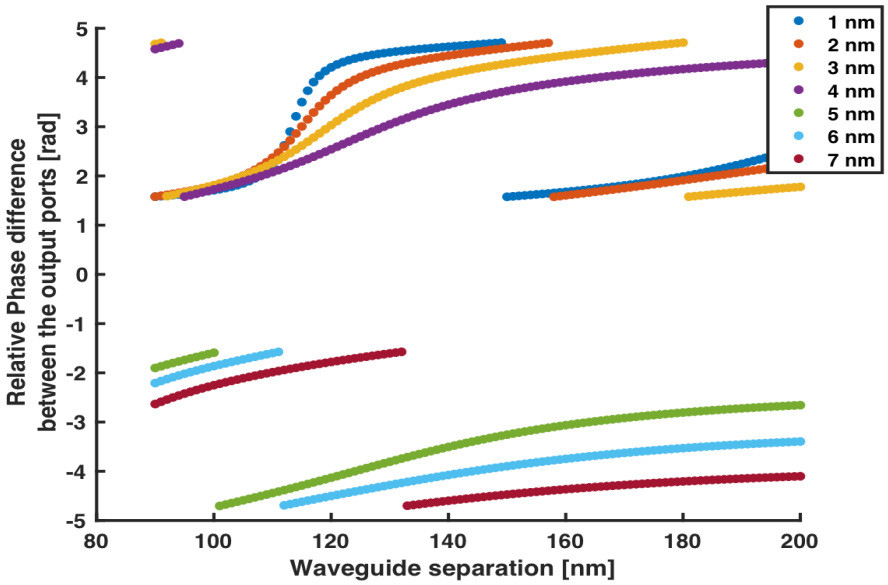

Figure (3.2) A plot showing the relative phase difference between the two output ports of an asymmetric directional coupler as a function of waveguide separation. In this plot the different colours indicate the difference in waveguide width of the device that produced that range of relative phase differences.

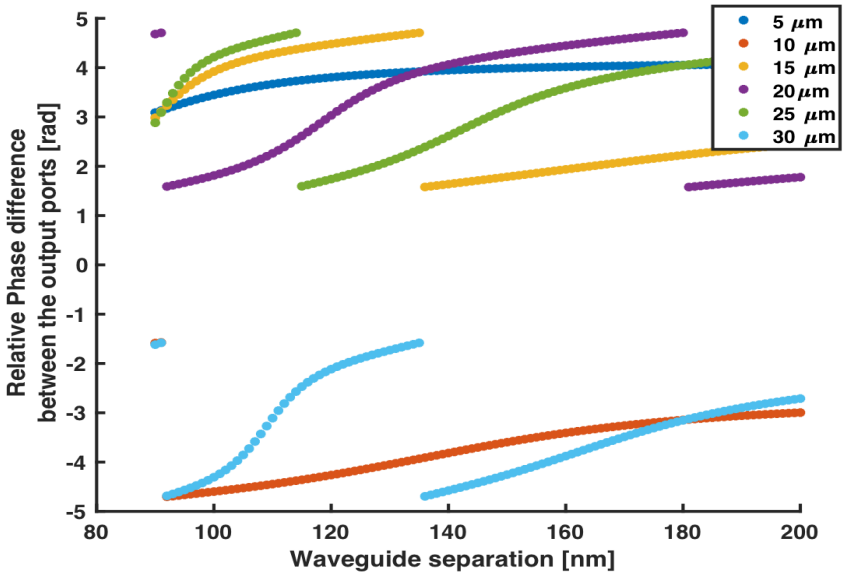

Figure (3.3) A plot showing the relative phase difference between the two output ports of an asymmetric directional coupler as a function of waveguide separation. In this plot the different colours indicate the coupling length of the device that produced that range of relative phase differences.

the longer the coupling length, the shorter the range of waveguide separation needed to achieve a full pi phase shift. This would suggest that in fabrication, it would be optimal to have as long a coupling length as possible to minimize the waveguide separation range in this way so that a greater range of asymmetry would be able to achieve a full pi phase shift within a reasonable waveguide separation range. Unfortunately, the longer the coupling length is the more vulnerable the device becomes to breaking, so this limits how long the

coupling length can realistically be.
Lastly, other than establishing how the coupling length affected the range of useful asymmetries, the narrowness of waveguide 1 was also found to have an effect. The simulation was run with the width of waveguide 1 being set at different values ranging from 225nm to 180nm. The results from when the width of waveguide 1 were 180nm and 225nm are shown in Figure 3.4 part (a) and part (b). This figure shows that the narrower the waveguide, the larger the asymmetry of the directional coupler could be and still achieve a full pi phase shift within a reasonable waveguide separation range. Again, like with the coupling length, fabrication becomes more difficult when the waveguides become narrower so this constrains how narrow the waveguides can be made and hence also the range of asymmetries which are able theoretically to fulfil the phase shifter requirements desired.

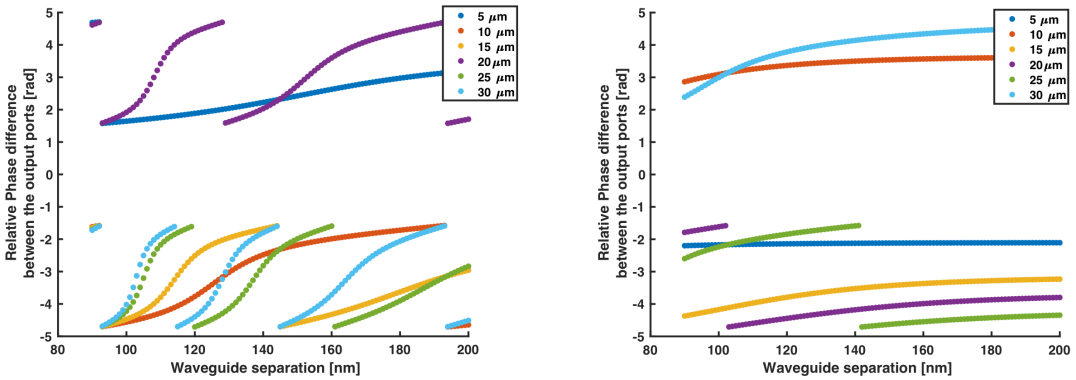

Figure (3.4) Two plots showing the relative phase difference between the two output ports of an asymmetric directional coupler as a function of waveguide separation. In this plot the different colours indicate the coupling length of the device that produced that range of relative phase differences. In (a), the width of waveguide 1 is 180nm and the asymmetry is 3nm while in (b) the width of waveguide 1 is 225nm and the asymmetry is 3nm. By comparing the results of (a) and (b), it appears that the devices with the narrower waveguides in (a) can have a shorter coupling length and achieve a full pi phase difference than the wider waveguides in (b).

3.1.1 What asymmetry is optimal?

Taking both the results of the device simulations and the fabrication results into account, it was concluded that a range of asymmetric directional couplers with varying parameters should be made. This was to ensure that if those which were optimised in terms of narrowness or length broke due to their increased fabrication risk, then there would still be some devices for measurements which although not optimised for all three parameters discussed in the previous section, still would retain one or two optimised parameters and yield informative results. The chip that was ultimately fabricated contained 144 different directional couplers. The waveguide width for the first 72 was 180nm whilst the remaining had a width of 200nm. For the first 72 of the devices, to make them more robust to compensate for their extra narrowness, the maximum coupling length of the waveguides was 35 μm. The minimum length was 27 μm. For devices 73 to 144, the maximum length was 43 μm and the minimum length was 35 μm. For both of the different widths of waveguide 1 of the devices,

the asymmetry was varied between 0 and 10nm. By having this range of asymmetry for both widths, the hope was that it would be possible to test if, like in the simulations, there would be a difference in the phase shift that was achieved within the same range of waveguide separation. The final parameter that was varied in the devices was the initial gap size between the two waveguides in the asymmetric directional coupler. Figure 3.3 shows that for length 30 μm that the smaller the initial waveguide separation the steeper the change in phase shift as a function of waveguide separation. The aim of varying this gap size was to test how small the gap size could be fabricated without the device collapsing as well as testing how large it could be and still observe a significant phase shift in the device when voltage was applied.
In conclusion, there was no one set of optimal parameters for an asymmetric directional coupler as the contributing parameters can be balanced in different ways to achieve the optimal range of waveguide separation that it takes for a full pi phase shift to occur. The most ideal parameters therefore can only be found through fabrication as these are the ones which fulfil the simulation optimised values as well as being the most robust in fabrication.

3.2 Simulation of phase shift measurement

3.2.1 Theory behind simulation

As discussed in section 1.1, linear-optical networks which consist of beam splitters, phase shifters and mirrors can be used to realise any NxN unitary operator. There exists several methods to characterize such a network, involving non-classical or coherent states [20] [21] [22]. One example of this is to perform quantum process tomography. An issue with this method of characterization is that it becomes slow and impractical for large optical networks. In the paper 'Direct characterization of linear-optical networks' [23] an alternative method of characterizing a quantum network using linear optical circuit is reported. It was this method that was used as inspiration for the characterization of the phase shifters in this project. In the setup shown in Figure 3.5, one can see how in the paper [23],an N-mode optical network is characterized by uniquely determining a NxN matrix which represents the network. The linear-optical network is represented by a linear transformation of input to output creation operators which are related thus:

$$a_j^\dagger = \sum_{k=1} M_{jk} b_k^\dagger \tag{3.1}$$

Where $a_j^\dagger$ and $b_k^\dagger$ are the input to output creation operators and M_{jk} is the corresponding characterization matrix element of the matrix M which represents the linear optical network. The matrix element M_{jk} can be written as a complex number $r_{jk}e^{i\theta_{jk}}$ where $0 \leq r_{jk} \leq 1$ and $0 \leq \theta_{jk} \leq 2\pi$. The characterization method begins by sending a coherent state with an intensity I to input mode j. The other input modes are at this point in the vacuum state and intensity I_k is measured from all output modes simultaneously. From this measurement, one can obtain all the moduli:

$$r_{jk} = \sqrt{\frac{I_k}{I}}, k = 1, 2..., N \tag{3.2}$$

The second step is to use a beam splitter as shown in Figure 3.5 part (a) to split the coherent state into two output states which are referred to as $|a_1\rangle$ and $|a_2\rangle$ [23].

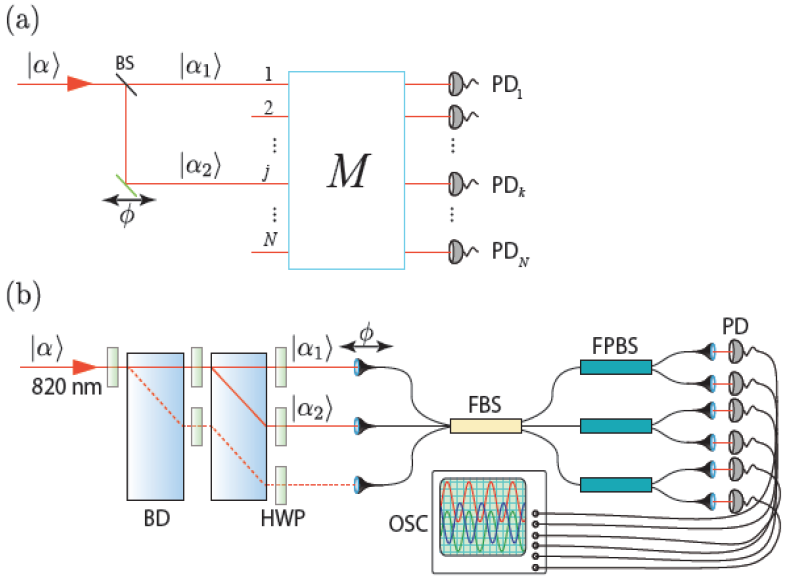

Figure (3.5) (a) A schematic diagram of the experimental setup used to determine all the phases that make up the matrix M. One can see a 50:50 beam splitter (BS) and a phase shifter (ϕ) which are used to create a dual-mode coherent state and sent through M. State $|a_2\rangle$ is sequentially inputted into the modes 2 through to N where in each case, the phase ϕ is varied over 2 pi to establish the θ_{jk} for each element of M. (b) A diagram showing the experimental realisation of the determination of the case investigated [23] where the matrix M constructed comes from testing a 3x3-mode fused-fibre beam splitter (FBS), which constitutes a 6x6 optical network which included polarization. The orthogonal polarization modes were resolved by using fibre polarization beam splitters (FPBS) at the outputs. In the figure one can see how the interferometric probe states between pair-wise input combinations were prepared with two polarization beam displacers (BD), as well as two half-wave plates (HWP). To monitor the outputs, fast photo-diodes (PD) were connected to an oscilloscope (OSC) while the phase ϕ was scanned. This figure is taken from [23].

Figure 3.5 part (a) shows an external phase shifter outside the network which can change the phase between $|a_1\rangle$ and $|a_2\rangle$ by ϕ degrees. Due to the beam splitter being 50:50, the intensities of the two states are equal and the state $|a_2\rangle$ can hence be written as $|e^{i\phi}a_1\rangle$ when the input mode is '1' and where ϕ is the phase added to $|a_2\rangle$. Inducing a phase difference between $|a_1\rangle$ and $|a_2\rangle$ leads to the two beams interfering inside the network and hence is considered as an interferometric method of characterization that has the advantage of not needing an external interferometer or non-classical interference and single photon detection. In the general case [23], the intensity of the output coherent states at the collection ports of the output of the optical network M can be written thus:

$$I_k = I\left|M_{1k} + M_{jk}e^{i\phi}\right|^2 \tag{3.3}$$

When k=1 thus simplifies to:

$$I_1 = I\left[r_{11}^2 + r_{j1}^2 + r_{11}r_{j1}cos(\phi)\right] \tag{3.4}$$

and when k≠1

$$I_k = I\left[r_{1k}^2 + r_{jk}^2 + r_{1k}r_{jk}cos(\phi + \theta_{jk})\right] \tag{3.5}$$

Where θ_{jk} is a nontrivial phase of the matrix M. It is this nontrivial phase which is of interest for this project and for characterizing the phase shifters fabricated in it. From

equation 3.4 one can see that I_1 achieves its maximum and minimum value when $\phi = 0$ and $\phi = \pi$ respectively. By sweeping the value of ϕ from 0 to 2π, one can find the maximum value of I_k and hence from equation 3.5, the unknown, nontrivial phase θ_{jk} can be found as:

$$\theta_{jk} = 2\pi - \phi \tag{3.6}$$

Figure 3.6 shows the results of a characterization of a linear-optical device from [23]. In Figure 3.6 parts (a) and (c) one can see the moduli r_{jk} of the experimentally measured M and the phases, θ_{jk}, of the measured matrix M. Part (b) of Figure 3.6 shows the representative experimental data which was used to obtain the value of θ_{jk} when injecting the variable-phase dual-mode coherent state into input modes 1 and 3. One can observe how the amplitude of the voltage at the output modes oscillates as the phase shift ϕ is swept. The red lines indicate the measured data and the blue lines are the theoretical fits to the function $A\cos(\phi - \theta_{jk})$.To obtain the results in Figure 3.6, a network consisting of one 3x3 non-polarizing fused fibre-optic beam splitter (FBS) with three 2x2 polarizing beam splitters at each of its output modes was characterized. The experimental setup used for the characterization is shown in Figure 3.5 part (b). From the results obtained, a matrix M could be constructed to represent the linear optical network. This matrix was verified in [23] by measuring two-photon interference inside the linear-optical network. Due to this method being a fourth-order interference effect, it was deemed a suitably independent verification for the validity of the matrix M that was obtained using the second-order interference method used to obtain the results in Figure 3.6.

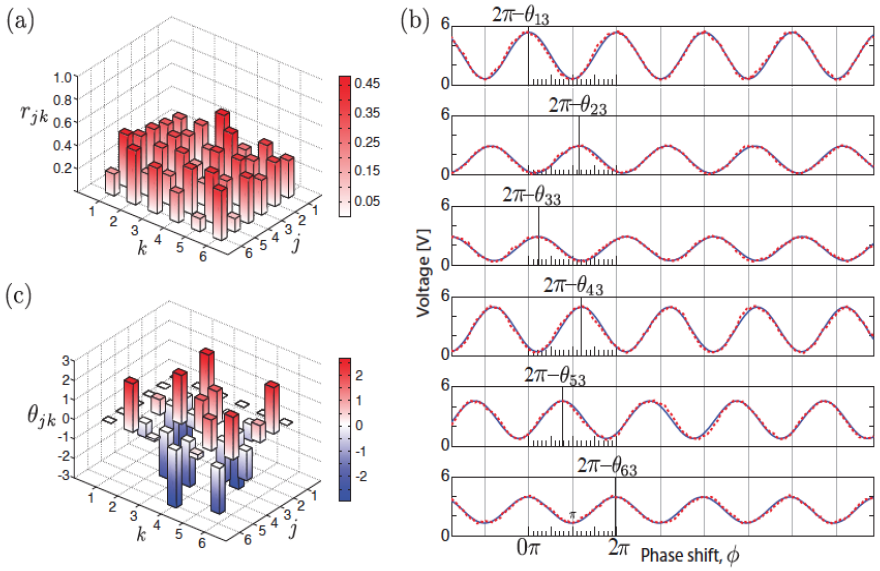

Figure (3.6) (a) The x and y axis represent the input and output modes measured and are denoted as j and k respectively and the z axis is the moduli r_{jk} of the experimentally measured M. (b) This figure shows an example of some of the experimental data used to obtain θ_{jk} where the variable-phase dual-mode coherent state was injected into input modes 1 and 3. The x axis represents the phase ϕ which is swept in tome and the y axis is the amplitude of the voltage at the output photo-diodes of the six output modes. (c) The x and y axis represent the input and output modes measured and are denoted as j and k respectively and the z axis is the phases θ_{jk} of matrix M. This figure is taken from [23]

This validation gave further confidence in the results of the second-order interference method of obtaining matrix M as it showed that the obtained interference visibility was in excellent agreement with those predicted by the matrix M constructed from the experimental results of the second order interference method. In Figure 3.7 one can see how in this project, the experiment is adapted and simplified to measure the phase shift achieved by an asymmetric directional coupler when the waveguide separation is changed. One can see, that rather than having to uniquely determine a NxN matrix which represents the network, one only has to determine a 2x2 matrix.

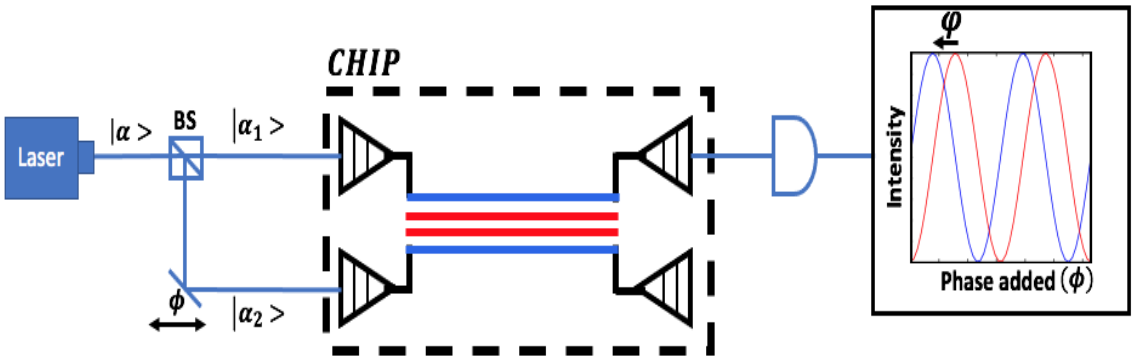

Figure (3.7) This figure shows a diagram of how the phase shift produced by the asymmetric directional coupler was measured in this project as inspired by the theory described in this section. One can see how the gap size between the two parallel waveguides (coloured blue and red to indicate the different waveguide separations) affects the relative positions of the interference curves (coloured blue and red to correspond to the gap size they represent) and how the phase shift achieved by the asymmetric directional coupler was obtained.

3.2.2 How failure to balance power inputs affects phase shift measurement

Inspired by the experiment discussed in section 3.2.1, simulations were run to test if a phase shift could be observed when changing the waveguide separation of the asymmetric directional couplers by inducing a phase difference between the two input states with an external phase shifter. Figure 3.8 shows the results of the simulations of the phase shift measurement for a nano-mechanical photon router compared to an asymmetric one. On the x axis, is the external added phase referred to as ϕ in the paper [23], and on the y axis is the normalised intensity measured at one of the outputs of the linear optical network. The output of the linear optical network in this case is one of the output ports of the directional coupler.

As shown in Figure 3.8 part (a), when the directional coupler is symmetric, there is no shift in the position of the peaks of the interference curves when the waveguide separation is changed. This is expected as the nano-mechanical photon router only acts as a beam splitter, and does not have any phase shifting properties. However, as it appears from Figure 3.8 part (b), that for a device that has an asymmetry of 1.75nm, there is a shift in the position of the peaks of the interference curves for the different waveguides separations.

In running the simulation for this experimental method of measuring the phase shift, it was also tested how changing the ratio of the input intensities would affect the measurement. This was important to check because, in reality, it would be very difficult to make

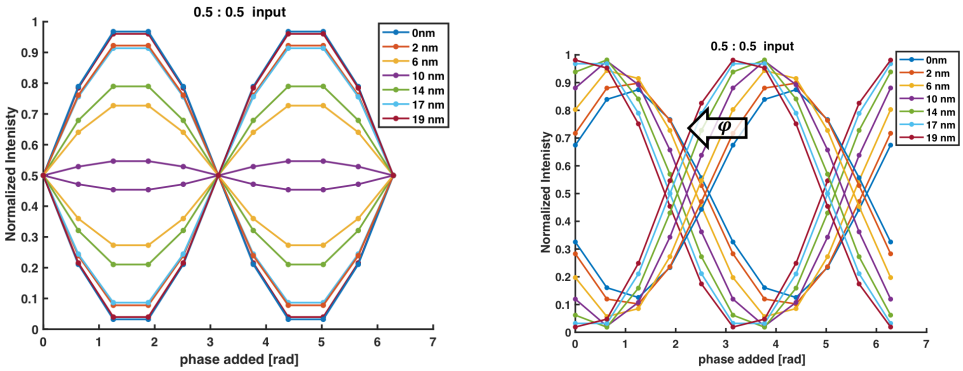

(a) (b)

Figure (3.8) (a) This figure shows how the visibility of the interference curves at both output ports changes depending on the waveguide separation when the ratio of the power entering the input ports is 50:50 for a nano-mechanical photon router. The key indicates the different waveguide separations of the interference curves by different colours. The two curves of the same colour represent the interference curve that would be measured at each of the respective output ports for the waveguide separation and input states. (b) This figure shows how the visibility of the interference curves at both output ports changes depending on the waveguide separation when the ratio of the power entering the input ports is 50:50 for an asymmetric directional coupler with an asymmetry of 1.75nm. By inspecting the positions of peaks of the interference curves for the different displacements compared to each other, one can see that for the case of the nano-mechanical photon router in part (a), the peaks overlap whereas in part (b) there is a shift in the peak position between the different displacements. This shift appears to increase with the displacement of the waveguide separation. This indicates that by increasing the waveguide separation of an asymmetric directional coupler, one can change the phase difference of the light between the output ports of the device. As this shift in the peaks is not present in part (a) one can see for a perfectly symmetrical directional coupler there is no observable phase shift between the difference waveguide separation displacements which is expected from coupled-mode theory as explained in section 2.1.

sure that the power going through the two input ports of the asymmetric device are equal. Thus one can only measure the power before the light is coupled into the microscope and onto the chip and after it has been coupled through the device and emitted through the output ports. This means there is no way to know if the light is equally well coupled through input ports and hence if the power being emitted through the device at each input port is equal to the other input port. Figure 3.9 shows a comparison of what the phase shift measurement looks like when the input power going into the two input ports is not balanced for a nano-mechanical photon router (Figure 3.9 part a) and for an asymmetric directional coupler with an asymmetry of 1.75nm (Figure 3.9 part (b)). One can observe that for Figure 3.9 part (a) as in Figure 3.8 part (a), when the directional coupler is symmetrical, there is no change in the position of the peaks of the interference curves when the displacement is increased. This suggests that unbalancing the power for a nano-mechanical photon router, does not change the phase shift (or lack thereof in this case) measured using this phase shift measurement technique. The difference that is observed when the input power is unbalanced rather than balanced is that there is a larger change in visibility of the interference curves when the displacement is changed over the same displacement range. This concurs with the results shown in Figure 3.9 part (b), where when compared to Figure 3.8 part (b) the change in visibility over the same displacement range was far larger when the input power was unbalanced compared to balanced. Indeed, it was found that the larger the difference

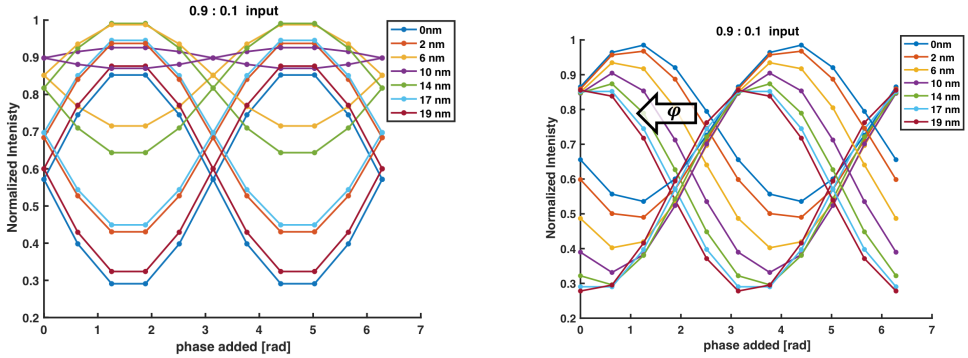

(a) (b)

Figure (3.9) (a) This figure shows how the visibility of the interference curves at both output ports of a nano-mechanical photon router changes depending on the waveguide separation when the ratio of the power entering the input ports is 90:10. The key indicates the different waveguide separations of the interference curves by different colours. The two curves of the same colour represent the interference curve that would be measured at each of the respective output ports for the waveguide separation and input states. As in Figure 3.8 part (a) the position of the peaks of the interference curves for the different displacements remains the same. However, unlike Figure 3.8 part (a) the visibility of the curves decreases significantly more as the displacement increases. (b) This figure shows how the visibility of the interference curves at both output ports of an asymmetric directional coupler with an asymmetry of 1.75nm changes depending on the waveguide separation when the ratio of the power entering the input ports is 90:10. Compared to the figure in (a), the peak positions of the interference curves do change when the displacement of the waveguide separation of the directional coupler is changed. This is the same change as is seen in Figure 3.8 part (b). However, unlike Figure 3.8 part (b) there is a significantly greater decrease in visibility as the displacement increases.

between the two input beams the greater the change in visibility over the same waveguide separation range. The phase shifts achieved by the asymmetric directional used to create the plots in Figure 3.8 part (b) and Figure 3.9 part (b) were found to be equal when the power was balanced and when it was unbalanced.

In conclusion, whilst having the input power balanced optimised the visibility of the interference curves throughout the phase shift measurement, it did not change the value of the ultimate phase shift measured. This was promising news for the realisation of this phase shift measurement method as it demonstrated that even if the input power balance is not optimised, it should not affect the resulting phase shift measured, assuming that the visibility remained high enough to be able to identify the peaks of the interference curves accurately.

Chapter 4

Experimental setup and fabrication

This chapter is split into two main sections. The first of which gives a run-through of the challenges faced with the fabrication of nano-mechanical phase shifters on a chip and a selection of SEM pictures which show different errors which occurred during the fabrication. The second section contains a summary of the different experimental setups used in this project to characterize the devices on the chip and to measure the phase shifts that they generated. It also contains information on the various challenges encountered when conducting these experiments and how various elements of the setup were added to minimize the effects of drift.

4.1 Overview of fabrication challenges

For this project, the chips that were designed by me were kindly fabricated by Zhe Liu; together we took SEM pictures of the chips to check the yield of the fabricated chip as well as which fabrication errors were most common. The chips that were fabricated each consisted of three columns of devices which were attached to electrodes which when wire-bonded to the cryostat, would allow voltage to pass through to the devices. In these three columns there were 144 different asymmetric devices in total. Next to the devices, their respective number and design parameters were etched to identify them for measurements. The chips were fabricated from the same QD dense wafer (B15242). Figure 4.1 shows an SEM image of part of column 1 on chip 1. In Figure 4.1 part (a) one can see how the devices are aligned between two metal plates which act as bonding pads, connecting the devices to the voltage source. Figure 4.1 part (b) shows more clearly how each device in the column is connected to the bonding pads through electrodes (yellow lines) which creates the deformation of the gap size between the two waveguides.
In between the pairs of bonding pads there were also nanobeams fabricated to help couple the light more easily through the devices and identify what wavelengths of laser light were able to pass through the grating of both the nanobeam and asymmetric directional couplers. The design parameters of the devices in the chips were identical. However, due to changes made by Zhe Liu to optimise the procedure of fabrication, the devices of the two chips with the same design parameters were not identical. The main reason for this was that in the case of chip 1, the method used to etch the devices caused them all to be undercut so that

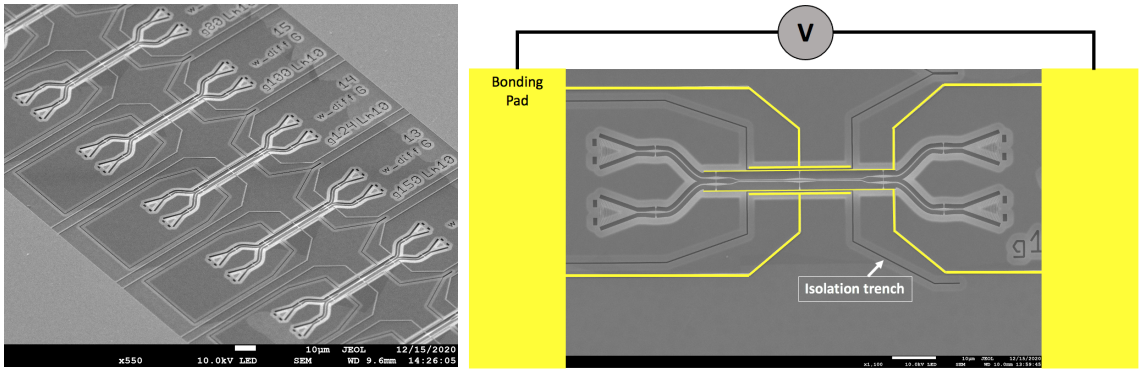

(a) (b)

Figure (4.1) (a) A SEM image of one of the columns on chip 1. In the photo, one can see that next to each device, the device number and the identifying design values of the device for easy identification are etched. (b) A SEM picture of one of the devices on chip 1 demonstrating how electrodes are used to modify the gap size of the device by applying a voltage across the device.

the waveguides were all 40nm narrower than their design parameters. This was not the case for the second chip where a different method of etching was used. The closeness of the actual parameters of the fabricated devices to those of the design parameters are not fully known as the chips could not be examined sufficiently close because it would result in the electrons of the SEM damaging the devices if the device were examined at the sufficient closeness. This was the case for device 144 in Chip 2, where after the widths of the two waveguides were found to be 191nm and 204nm (9nm and 6nm different from the design parameters), the waveguides collapsed as shown in Figure 4.3 part (d). Another difference between the two chips was how well the gratings were suspended. For chip 2 the etching time was increased from 40 seconds to 50 seconds, which led to an improvement in the grating shown in Figure 4.2. That the grating is not fully suspended even in chip 2 is not so much an issue. Despite it naturally affecting the efficiency of the device, it also makes the device more robust and may be one of the reasons why for both chips there was such a high yield of devices (close to 100%).

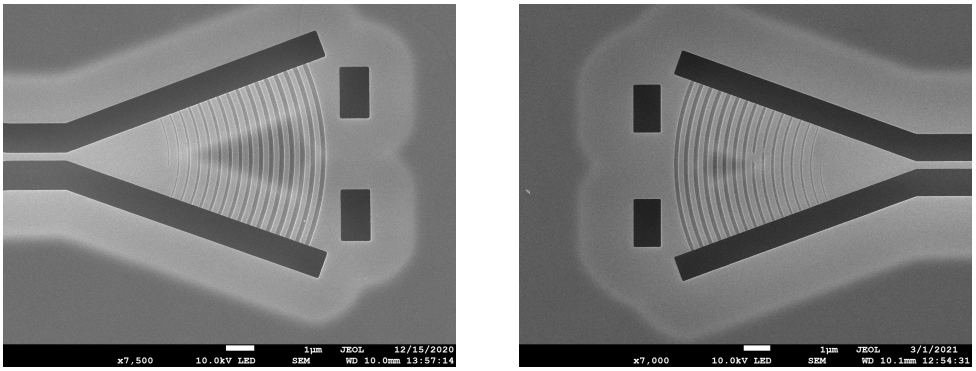

(a) (b)

Figure (4.2) (a) A SEM image of a shallow etch grating from Chip 1 showing how the centre is not fully suspended (b) A SEM image of a shallow etch grating from Chip 2 showing how the center, though not fully suspended, is far more suspended than that of shallow etch grating in Chip 1.

For chip 1, the main cause of loss of devices was a scratch in the first column of the chip

caused by an accident during the fabrication process. This led to 4 devices being damaged. In chip 2, due to particles being present on the surface of the chip during fabrication, some parts of the devices were left unetched as shown in Figure 4.3 part (e). This particular fabrication error is thought also to be the reason for one of the columns short-circuiting in chip 2 as the same column had some of the isolation trenches separating the electrodes of a device left unetched which provided a shorter pathway for the current to take instead of the one it should have taken. In the other remaining subplots of Figure 4.3 there is pictured an ensemble of other fabrication errors which occurred both in chips 1 and 2.

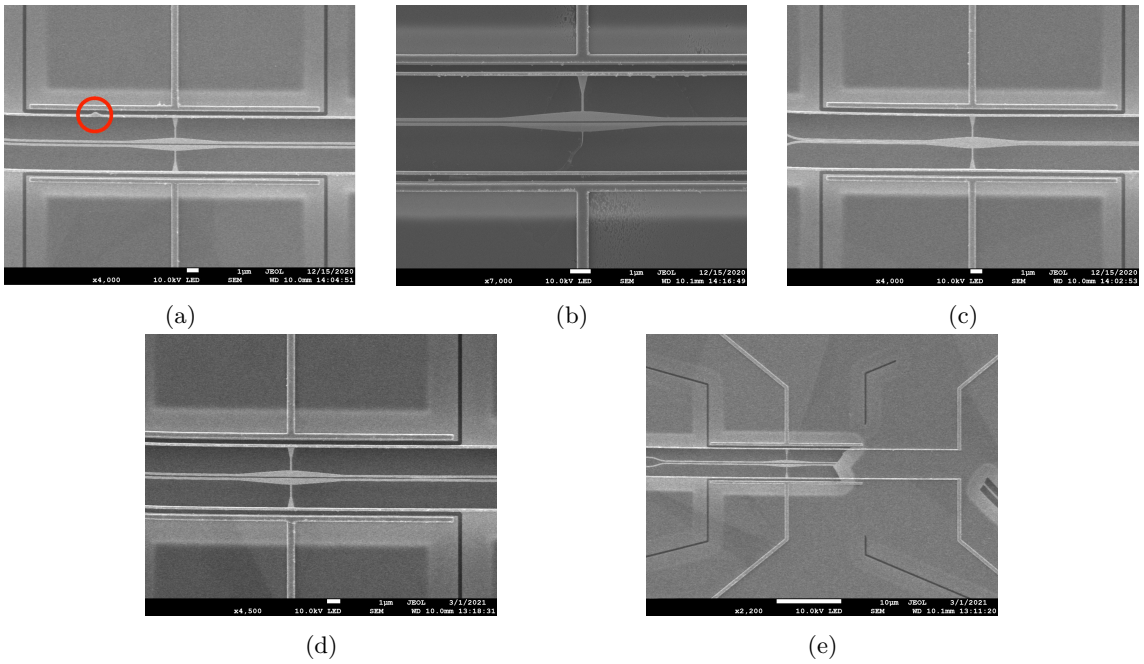

(a) (b) (c)

(d) (e)

Figure (4.3) A collection of SEM images illustrating different fabrication errors which occurred and decreased the yield of both chips. (a) In the red circle is a particle that lies in such a place that prevents the electrodes from moving as they should when a voltage was applied. (b) One of the tethers connecting one of the waveguides to an electrode is broken. (c) The two waveguides of this device are merged. (d) In this The two waveguides of this device have collapsed and there is no longer a continuous gap size between them. (e) A particle present on the surface of the chip early on in the fabrication process led to part of this device and the isolation trench being left unetched.

4.2 Experimental setup for interference measurement

To measure the phase shift, it was important to establish and optimise the interference measurement which was integral to finding the phase shift produced by the device. In this section, interference measurement method is explained and how various challenges were overcome. Figure 4.4 shows the experimental setup that was used to conduct the interference measurement where the light from a Continuously Tunable Laser (CTL) laser was coupled through a device on the chip in the cryostat. The red and green lines represent the two beams of laser light which originate from the same laser beam and which ideally should have a constant phase difference between them if the respective optical path lengths of their paths are not modified. The attenuation filter placed in the optical path of one of the input

laser beams is used to balance the power of the two input beams, this ensures that they produce the same counts collected at the output of the device by the Spectrometer to maximize the visibility of the interference measurement. The rectangle labelled P.M. represents a power meter which as shown, is connected to the computer and a PID (proportional integral derivative controller). These three elements together create a feedback system which removes power drift from the interference measurement. More details on the methods by which this setup was kept stable by minimising drift are discussed in section 4.2.1. The phase shifter used to change the phase difference between the two input laser beams is also shown in Figure 4.4. More details about the mechanics and design of this phase shifter are found in section 4.2.2. A step-by-step guide to how the interference measurements are conducted can be found in the appendix (section 7.1.1).

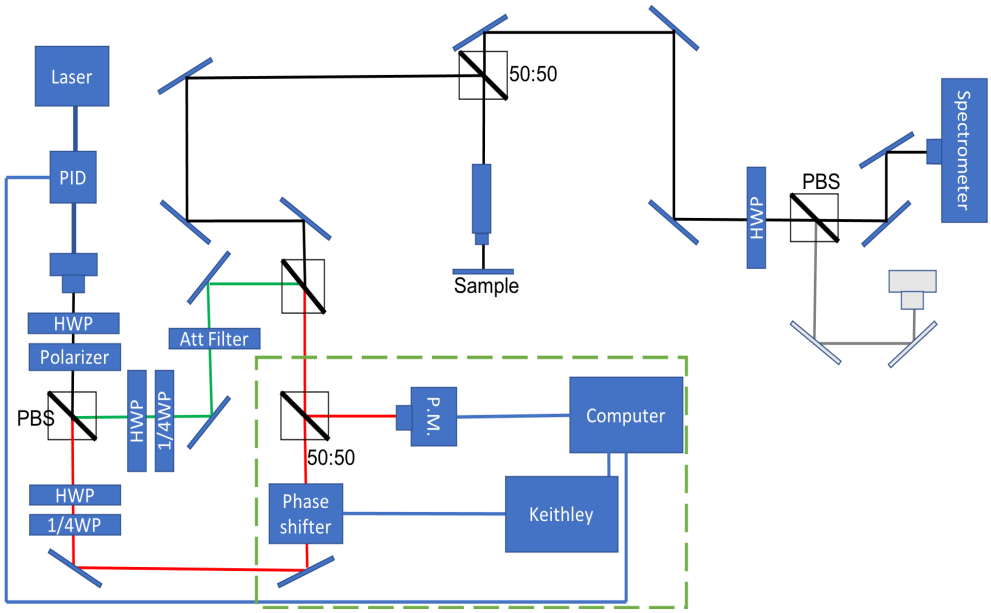

Figure (4.4) Experimental setup used for conducting the interference measurement where the light from the two input beams (red and green lines) are each coupled through one of the input ports of a device on the chip ('sample') inside the cryostat and the collected light from one of the output ports is collected into a fibre which is then measured with a Spectrometer. At the beginning of the setup the light from the laser transitions from inside a polarization maintaining fibre into free space where it remains through the rest of the setup until being collected into a fibre connected to the Spectrometer to measure the output light from the device. The blue rectangles labelled HWP and 1/4WP denote half and quarter-wave plates respectively. The polariser is used to force only one polarization of light to pass through the setup to minimize the polarization drift in the setup. PBS denotes a polarization beam splitter which in theory should split the beam of laser light into two equal beams (red and green beams). The black square with a diagonal line through it with 50:50 written next to it denotes a 50/50 beam splitter.

4.2.1 Phase and power drift

To keep the setup stable, it was necessary to minimize different types of drift that could affect the results. To overcome power drift, a PID was used to lock the power of one arm in such a way that the amount of power being sent through automatically compensated for any power drift or fluctuations to keep the power meter measuring the number of μ watt it had been locked at. To prevent polarization drift causing the power locking to unlock,

an extra polariser was added to force only one linear polarization from the laser to pass through the PBS that splits the beam into the two input beams. This ensures the ratio that the PBS splits the beam into is kept constant.

4.2.2 Selection of external phase shifter for phase shift measurement

Two different methods of inducing a phase shift in one of the input beams in the interference measurement were tested. The first method used a piece of glass attached to a rotatable mount (Figure 4.5).

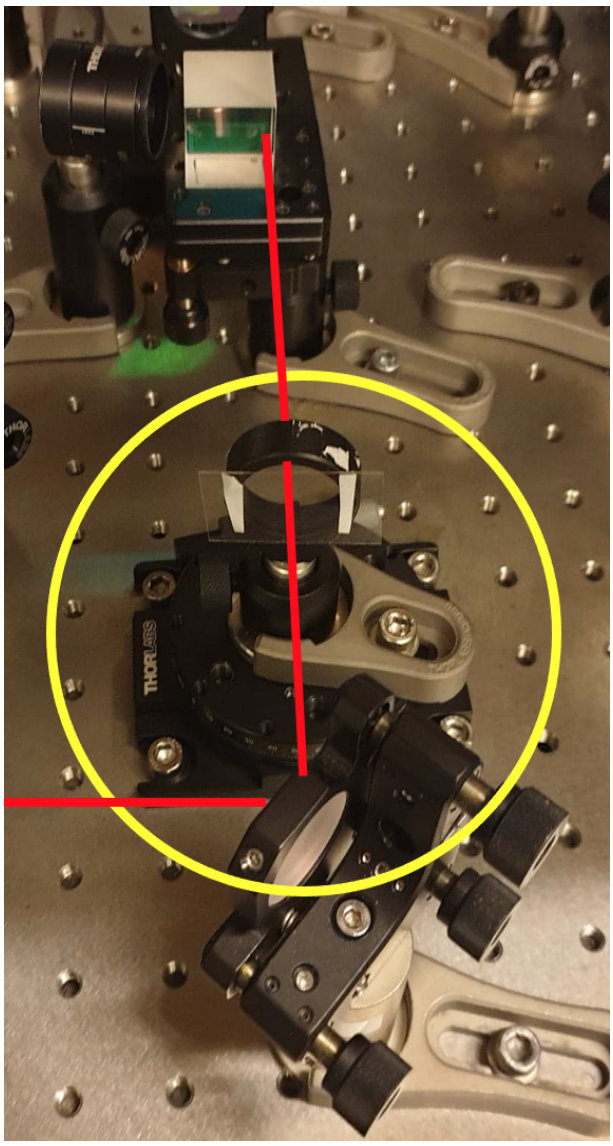

Figure (4.5) In the yellow circle of this photo, one can see how a thin piece of glass was attached to a rotation mount which could manually be rotated during the interference measurement. The red line indicates the optical path of one of the input beams whose length is changed by rotating the piece of glass.

In theory, by rotating the glass through which the light was passing, the optical path length

of the light should change as well. This can be shown in the following equation:

$$\Delta L = d \cdot (\frac{1}{cos(\theta)} - 1) \tag{4.1}$$

Where ΔL is the change in optical path length, θ is the angle the glass is rotated and d is the thickness of the glass. The phase change which is induced by the change in optical path length of the input beam of light was calculated with the following equation:

$$\Delta\phi = \frac{2 \cdot \pi \cdot \Delta L \cdot n_{glass}}{\lambda}; \tag{4.2}$$

Where $\Delta\phi$ is the phase change, ΔL is the change in optical path length, λ is the wavelength of light and n_{glass} is the refractive index of the glass. Figure 4.6 shows that when the relevant values for the glass used in this experiment are inserted into equation 4.2, one achieves a full 2 pi phase shift when the glass is rotated less than 6 degrees.

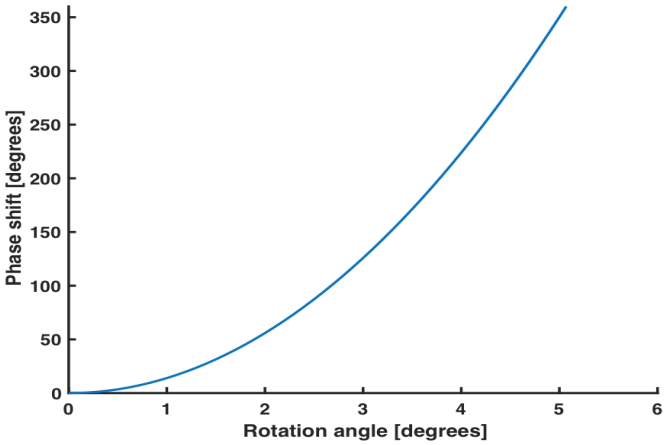

Figure (4.6) A plot showing how the phase shift in one of the input beams is changed by changing the angle when the piece of glass is rotated with help of the rotation mount.

There were several issues however when interference measurements were attempted with this type of phase shifter. One of the main issues was that the rotation mount was manual and hence it was difficult to keep conditions the same for consecutive interference measurements. Another issue was that when the input beam that did not go though the external phase shifter was blocked, so that only the output of the other input beam going through the piece of glass was being recorded, sharp changes in the counts measured at the output were observed when the glass was rotated. A plot showing this can be found in the appendix in Figure 7.1. As there was only one beam present, there was no interference and hence the power being measured should not experience sharp changes due to the glass rotating. One possible reason for this happening was that the beam was not going through the centre of the glass on the mount. If it is off centre and the glass is rotated, it can cause the beam to be displaced and hence affect the coupling to the device. Unlike the issue with the mount being manual, this issue was found more difficult to solve due to the sensitivity of the measurements to the laser beam being even slightly off centre. It was therefore decided that a different approach of inducing a phase difference between the two input beams was needed.

The second method of inducing a phase difference between the two input beams was by

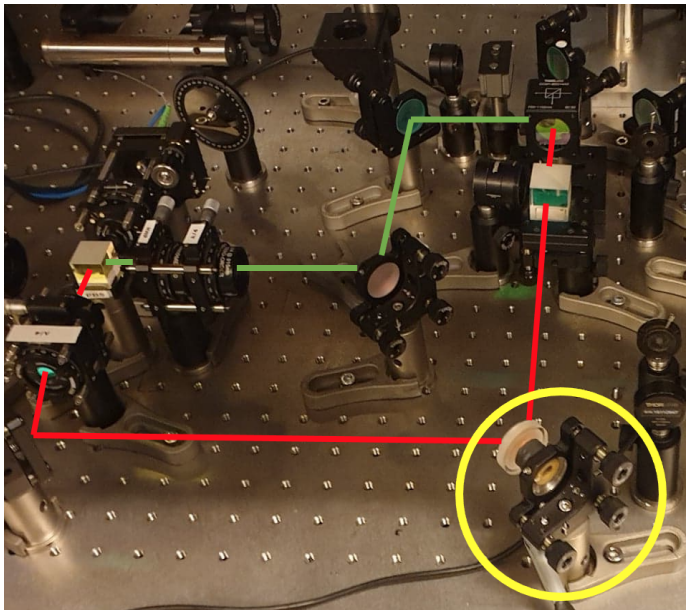

Figure (4.7) In this photo, the yellow circle highlights where the piezo mirror is inserted in the setup to modify the optical path length of one of the input beams when voltage is applied to it. The red and the green lines overlayed in this photo represent the path of the two input beams until the point where they are recombined in the PBS as in Figure 4.4

replacing one of the mirrors guiding one of the input beams with a piezo mirror as shown in Figure 4.7. By applying a voltage to this piezo mirror, its position would change and hence cause the optical path length of the red beam to change as well. To calculate the phase difference between the two beams, the relationship between the change in axial displacement and applied voltage had to be defined. Figure 4.8 shows the relationship between the axial displacement (Δ L) and the applied voltage (V). From the same source the following equation can also be found:

$$\Delta L_{axial} = d_{31(GS)} \frac{l}{t} V \tag{4.3}$$

This equation shows that there is a linear relationship between the axial displacement and the applied voltage and that it is both the tube wall thickness (t) and the transverse piezoelectric large-signal deformation coefficient ($d_{31(GS)}$) that determines the gradient at which the axial displacement changes as a function of voltage. Unfortunately, despite much searching, the value of the transverse piezoelectric large-signal deformation coefficient could not be found in any of the piezo motor specs. It was therefore necessary to make an approximation, using the available information to determine a value for the gradient relating the applied voltage and axial displacement. From examining the specs [25] it was found that in a range of 1000 V, a displacement of 15 μm could be achieved. From this knowledge, along with the fact that the axial displacement and applied voltage are linearly related, the following approximate relation could be made:

$$\Delta L = b_1 \cdot V \tag{4.4}$$

Where b_1 is $\frac{15[\mu m]}{1000[V]}$. Figure 4.9 demonstrates how the phase difference between the two input beams changes with the voltage being applied to the piezo mirror using the relation in 4.4. As can be seen, to achieve a full 2 pi phase shift between the input beams, a large

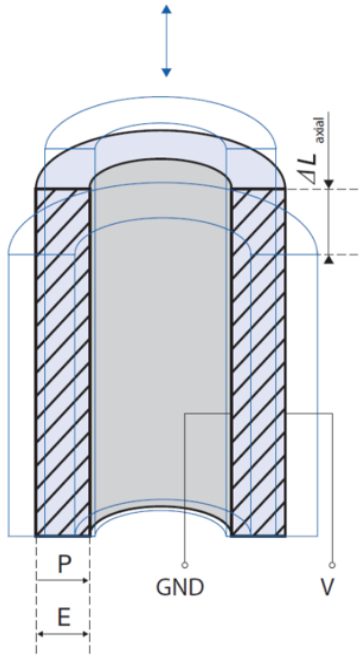

Figure (4.8) This diagram demonstrates how when applying a voltage to the tube actuator, which is the movable part of the piezo mirror, the axial displacement ΔL_{axial} changes.The blue double-pointed arrow indicates the direction in which the axial displacement moves. The voltage in this diagram comes from an external voltage source called 'V' which is grounded. P and E denote the polarization direction and electric field strength of the tube actuator respectively. This diagram is taken from [24].

voltage (about 60 V) is necessary. To achieve this large applied voltage, a Keithley voltage source was used with the interlocked bypassed to make a voltage range of 160 V available. This was found to be the best method of achieving a controllable phase difference between the two input beams. To make the interference more stable, however, it was necessary to use a CTL laser rather than a Ti-Saph laser. The reasons for this are discussed in section 5.1.1

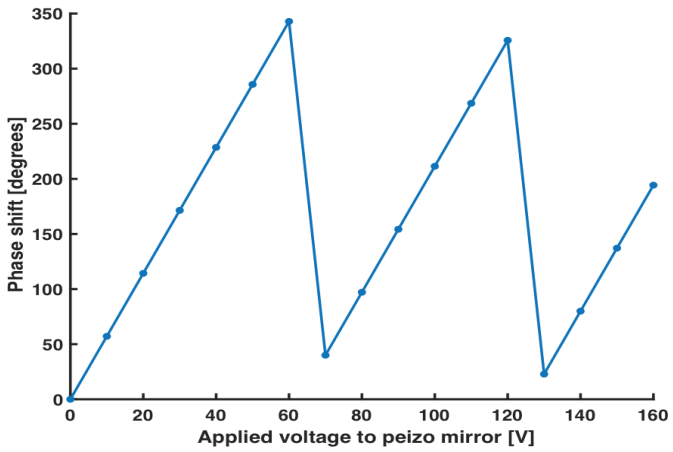

Figure (4.9) A plot showing the phase difference between the two input beams as a remainder of 360 degrees. It shows how the phase shift changes as a function of the applied voltage to the piezo mirror. To get a full phase 2 pi phase shift, approximately 60 volts need to be applied to the piezo mirror.

4.2.3 Free space interference setup and method

The method for the interference measurement in free space is very similar to that of the interference measurement described in the previous section. The only difference is that instead of the laser light being passed through a device on the chip in the cryostat and collected into a fibre to be measured with a Spectrometer, the light from the two input beams was aligned to overlap onto one spot on a power meter in free space. The change in the setup to perform the interference measurement in free space rather than through a fibre appears in Figure 4.10. Two pinholes were used to align the two input beams on the same spot on the power meter for collection and they can also be seen in Figure 4.10 inside the red dashed box. By making sure that both beams individually passed through these two pinholes, when the holes of both pin holes were minimized, one could make sure not only that the two beams were hitting the same spot on the power meter, but also at the same angle. In this way, the interference between the two beams was optimised.

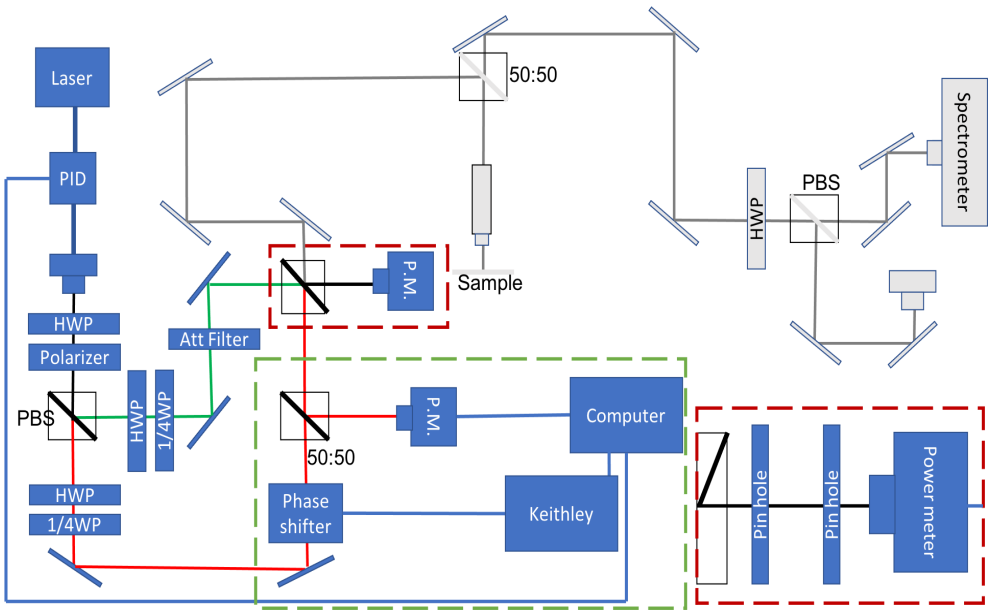

Figure (4.10) This figure shows a diagram of the experimental setup used for conducting the interference measurement in free space. Inside the red dashed box one can see how two pinholes were used to align the two input beams onto the same spot of the power meter used for the collection of the interfering light. The blue squares abbreviations HWP, 1/4WP, Polarizer, phase shifter, P.M., Att Filter etc, represent the same elements as they are used to denote in Figure 4.4

4.3 Experimental setup for transmission and reflection measurements used for characterization of devices

The setup used to perform the transmission and reflection measurements of the devices is shown in Figure 4.11. It should be noted, that whilst one of the measurements is being taken, one of the input beams is blocked so that there is only light from one input port being coupled through the device. The respective position of this input port compared to the output port which is connected to the Spectrometer determines if it is a transmission or a reflection measurement. This is explained further in Figure 5.4. Before the transmission

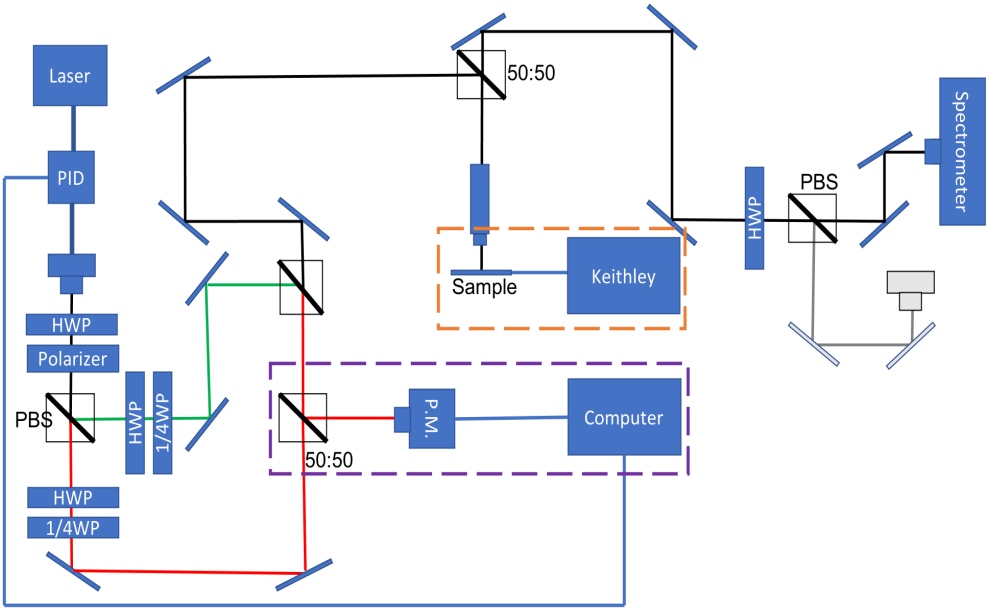

Figure (4.11) This figure shows the experimental setup used for taking transmission and reflection measurements used for characterizing the SR of the devices on the chip. The chip inside the cryostat has been wire bonded so that a voltage can be applied to the devices and change their gap sizes. The setup illustrates how a Keithley is connected to this wire-bonded chip and used as the voltage source. The blue squares abbreviations HWP, 1/4WP, Polarizer, phase shifter,P.M.,Att Filter etc, represent the same elements as they are used to denote in Figure 4.4

and reflection measurements can be obtained, the coupling of the light through the device had to be optimised. It was also necessary to optimise the collection from the output ports. To achieve this, the fibre coming from the laser was connected to one of the collection fibres of the outputs of the device to shine light into the output port of the device on the chip, through the reverse way of the setup. This made it possible to find where the collection spot on the chip was in comparison to the output port of the device. By adjusting the position of the mirrors at the collection, the position and angle of the collection spot on the chip can be optimised. Ideally, one should be able to see light coming out of the input ports of the device. The position of the focus spot along the z axis can also be adjusted so that it is aligned with the surface of the chip. Once the two collection spots have been optimally aligned this way, the optical fibre from the laser is disconnected from the collection fibre and reconnected to the correct input fibre (Figure 4.11) so that the light flows the correct way through the setup and hence also the chip. The Spectrometer is then connected to one of the output ports, ready for either a transmission or reflection measurement, depending on the position of the output port it is connected to compared to the input port where the light will be used. From the four series of measurements taken for each device, the SR as a function of voltage can be calculated. The purpose of this value is further discussed in section 5.2. A step-by-step guide to how the transmission and reflection measurements are conducted can be found in the appendix (section 7.1.2).

4.4 Experimental setup for phase shift measurement

For measuring the phase shift produced by the device when varying the gap size, two different Keithleys had to be simultaneously controlled throughout the measurement. One for controlling the position of the piezo mirror, and the other for controlling the voltage applied to the chip. This was achieved was by having two different computers simultaneously running two different MatLab scripts which communicated to each other using TCP/IP Server Sockets. One computer-controlled the two Keithleys via MatLab and the other controlled the Spectrometer and communicated to the first computer what and when it should set the voltage outputs of the two Keithleys to be a specific value. This complicated form of communication was needed because of communication issues which occurred when trying to control both Keithleys and the Spectrometer from the same computer. These communication issues would cause the Keithleys to freeze randomly during the measurements. This problem was due to the length of the USB cables needed to connect the Keithleys to the computer controlling the Spectrometer. The Spectrometer had to be connected to this particular computer because of the hardware requirements to run the program to control the Spectrometer. The Keithley that controlled the piezo mirror is referred to as Keithley 1 in this project and the Keithley that controlled the voltage applied to the chip is referred to as Keithley 2. Figure 4.12 shows the setup used for the phase shift measurement. The attenuation filter shown in Figure 4.12 was used to balance the two input beams so that the power measured at the output was the same for both inputs. The laser used for the measurements discussed in this section was a CTL laser set to a wavelength 945nm. In

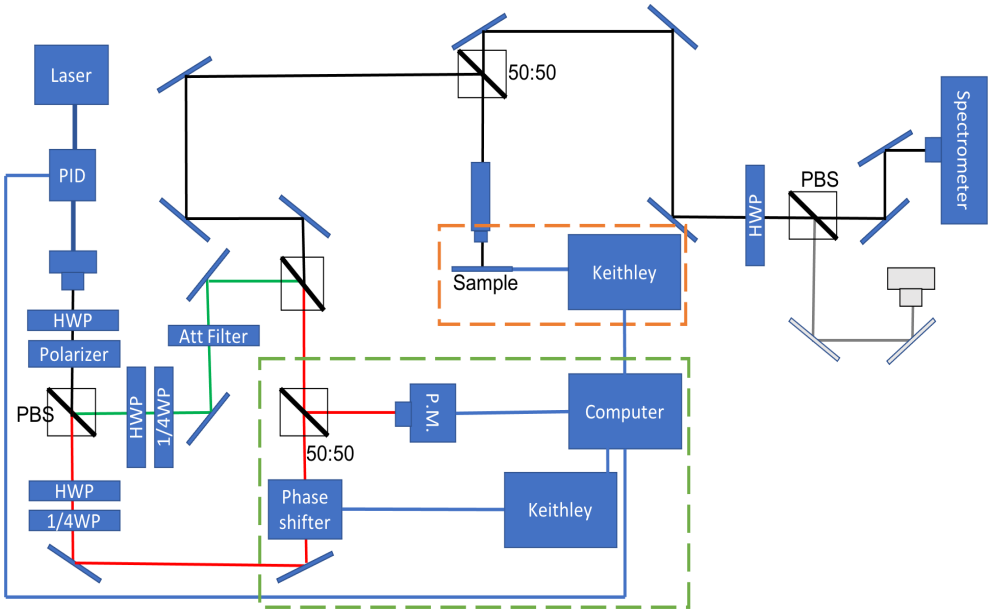

Figure (4.12) This figure shows the experimental setup used for taking the phase shift measurements in this project. It includes the phase shifter, used to change the interference between the 'green' and 'red' input beams which consists of a piezo mirror connected to a Keithley which is controlled through MatLab code by the same computer that controls the Keithley connected to the wire-bonded chip in the cryostat. The detector used to collect the light coming out of the output ports of the devices on the chip is a Spectrometer.The blue squares abbreviations HWP, 1/4WP, Polarizer, P.M., Att Filter etc, represent the same elements as denoted in Figure 4.4

this project, two types of phase measurements were done, one which was longer in duration

than the other. A full description of how the longer of the two was done can be found in appendix 7.1.3. The shorter phase measurement method is almost identical, apart from it skips over steps 4 to 7. The reason for these two different types of phase measurements is to test the effects of duration of the measurement on the phase shift measured and its variation. The formula for how both phase measurements can be summarised as:

- An interference measurement is measured with the Spectrometer by changing the position of the piezo mirror when there is no voltage applied to the chip.
- A voltage (or range of voltages) is then applied to the chip and another interference measurement is measured with the Spectrometer.
- The voltage applied to the chip is removed and a final interference measurement is measured with the Spectrometer.

Using this data collected by the Spectrometer, the positions of the peaks of the interference curves can be found through analysis. The shift in the position of these peaks relative to the peak position of the initial interference curve indicates the phase shift produced by the device when voltage is applied to the chip. In the appendix (Figure 7.2) one can find samples of the raw data collected with the Spectrometer before it had been analysed. To minimise drift whilst interference data was collected at the different applied voltages to the device, the number of measurements taken at each applied voltage to the piezo had to be limited to 10. The data was then analysed by taking the average of these groups of 10 measurements and fitting a sin curve to the normalised, averaged points of the interference measurement for each of the different applied voltages to the chip. Figure 5.14 and Figure 5.17 show plots which are examples of the product of this analysis.

Chapter 5

Setup characterization and measurement results

This chapter is split into 3 main sections. The first section discusses the results of the preliminary interference measurements taken with the setups shown in Figures 4.4 and 4.10 which were used to explore (i) how drift in the setup changes as a function of time and (ii) how the choice of laser affects the stability of the interference measurement. The second section details how the transmission and reflection measurements were used to characterize the devices and create tailored simulations of each device to predict the phase shift which they each should generate within a 7V range applied to them. The third section summarises the results of the phase shift measurement and compares them to the results of the simulations described in the second section.

5.1 Interference measurement

Two different types of interference measurements were performed and the results are reported separately in the next two subsections. The results in subsection 5.1.1 resulted from measurements taken in ' free space ' , where a power meter was used to measure the interference fringes where the beams were aligned in free space to hit the power meter on the same spot. This type of interference measurement was a characterization measurement used to characterize the free space visibility and stability and optimise these conditions in preparation for the second type of interference measurement taken. The results in subsections 5.1.2 and section 5.2 were obtained with this second type of interference measurement where the light from the laser was coupled through a device on the chip in the cryostat at room temperature, and then collected into an optical fibre connected to a Spectrometer, which measured the interference fringes. A Spectrometer was used because there was simply not enough power to be able to measure light with the power meter (i.e., the output light from the device was very weak). The reason behind this lack of power may be, among other possibilities, the gratings of the device not being fully suspended.

5.1.1 Free space interference measurement

The results of the free space interference measurement in free space led to two important discoveries which were used to optimise the setup for the phase shift measurements discussed

in the next section. The first of these discoveries was how to interfere the two beams of light with the piezo mirror working as a phase shifter to generate interference curves. The second was how to maximize the visibility of the interference curves. Initially, a Ti-saph laser [26] was used to conduct the free space interference measurements. The interference curves that were produced with this laser had a maximum visibility of 45%. This visibility was calculated using the following formula:

$$\nu = \frac{I_{max} - I_{min}}{I_{max} + I_{min}} \tag{5.1}$$

Where I_{max} and I_{min} are the maximum and minimum intensities of the interference fringes and ν is the visibility. It was also found that the interference fringes were very unstable as there were many occasions where it would seem the two beams would stop interfering and the interference fringes would suddenly disappear without cause. The relatively low visibility and instability of the interference curves produced when using a Ti-saph laser, were concerns as it would make completing a phase shift measurement very difficult. Specifically, as measuring the phase was very dependent on identifying the peaks of the interference curves, this made high visibility necessary for performing the phase shift measurements. Moreover, as the time taken by the phase measurement was significantly longer than that of a single interference measurement, the interference needed to remain stable throughout the whole phase measurement period. Initially, it was thought that the reason for both issues was that, despite using two pinholes to align the two beams to overlap on the same spot of the power meter, there was still an incomplete overlap. However, attempts to further optimise this failed to yield better results. Instead, exchanging the Ti-saph laser [26] with the CTL [27] laser solved the problem, as it led to a great improvement in visibility from the initial ‘free space’ interference measurement. To be certain however that this increase in visibility was reproducible, the free space interference measurement was repeated 5 times and the mean visibility was found to be 74 % when a CTL laser was used. Figure 5.1 shows how an example of how a successful interference measurement is done with the Ti-saph laser compares to one obtained with the CTL laser.

Through completing this series of consecutive interference measurements with the CTL, it was also found that this laser was capable of a far more stable interference than the Ti-saph laser, a difference resulting from the two lasers having different linewidths. By knowing the linewidth of the laser, the coherence length and time can be found using the following equation:

$$L_{coh} = c\tau_{coh} = \frac{c}{\pi\Delta\nu} \tag{5.2}$$

Where L_{coh} is the coherence length, c is the speed of light, τ_{coh} is the coherence time and $\Delta\nu$ is the linewidth (10kHz for the CTL and 1GHz for the Ti-saph). Using the specs of the two lasers [26] [27] the coherence lengths were found to be 9547.53m for the CTL and 0.095m for the Ti-saph laser. From these two values it is clear that the CTL has a far greater coherence length and in the case of the interference measurement setup is long enough to be stable along the setup's length where the Ti-saph has too short a coherence length and the coherence degraded along the length of the setup's optical path.

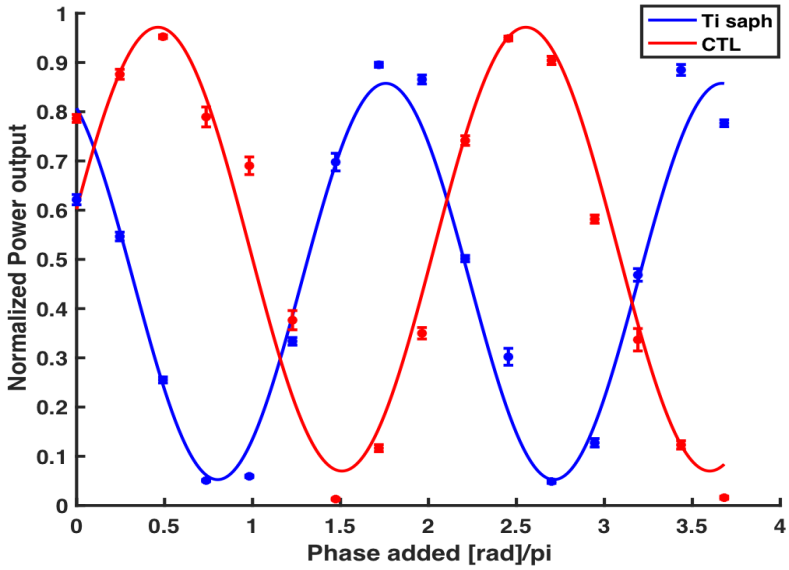

Figure (5.1) This figure shows an example of the interference fringes produced when using the CTL laser (red) which has a visibility of 80 % compared to Ti-Saph laser (blue) which has a visibility of 28%

5.1.2 Interference through directional coupler

To determine how stable the setup was in terms of phase drift in preparation for the phase shift measurement, the interference measurement was completed multiple times in different time intervals to test whether the position of the intensity fringes would drift over time without the gap size of the directional coupler being changed. Another important factor to explore was whether the amount of phase drift correlated with the time passed between consecutive interference measurements or whether it was random. Figure 5.2 is a plot illustrating how the amount of phase drift between interference measurements varied as a function of time.
From the available data, it is difficult to conclude how phase drift correlates with time but one can see that there is drift in phase between all the consecutive interference.

Figure 5.2 also shows, that there is considerable variation in the phase difference for consecutive measurements which have the same time interval between them. The size of the error bars indicate that the phase difference for consecutive measurements do not seem to follow any trend but instead are random in their variation as a function of the time interval. This supports the suggestion that phase drift is random and is not dependent on time intervals between measurements. If this was not the case then one would expect the error bars of the measurements done with smaller time intervals to be smaller than for those with larger time intervals.
Whilst these preliminary data are useful to explore if there was phase drift present in the setup, and hence if it was a factor to be taken into consideration when performing the phase drift measurement, they do not allow for making any firm conclusions on the following issues:

- To what extent this phase drift would impact the phase shift measurement
- If prolonging the time taken for the phase measurement to be completed would increase the impact of phase drift on the phase shift measurement.

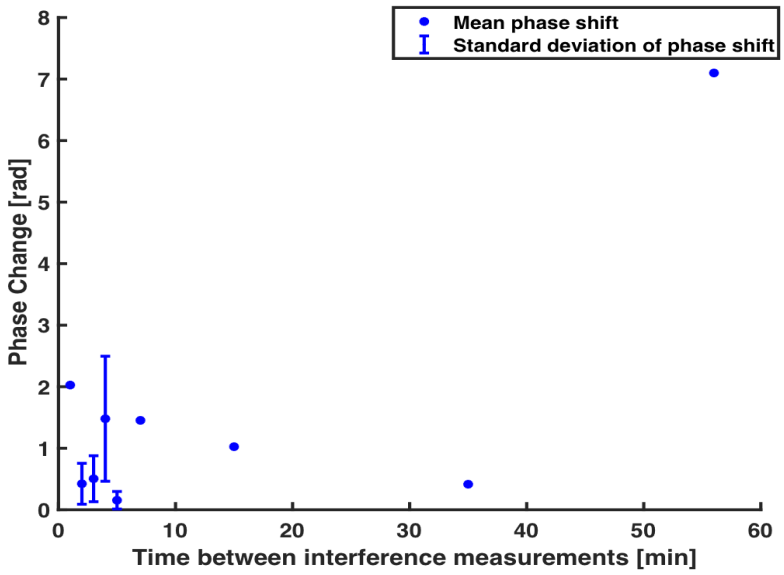

Figure (5.2) Plot showing phase changes between consecutive interference measurements where the time interval between the two measurements is varied.

To achieve this, more data should be collected to improve the statistical analysis of the phase drift as a function of time.

5.2 Splitting ratio calculation from transmission and reflection measurements

What is the splitting ratio (SR)?

The SR of a photonic device defines the ratio of the difference in power between the outputs of a coupler or beam splitter. For the asymmetric directional coupler, it would be expected that the SR changes as a function of the applied voltage. This is because when the gap between the two waveguides is deformed, the coupling changes and hence the ratio of power between the two output ports changes. Unlike with the nano-mechanical photon router, the device does not experience full extinction of one of its output ports due to its asymmetry, and this results in an asymmetric peak and dip when the SR is plotted as a function of wavelength.

What do we use the splitting ratio (SR) for?

To characterize the asymmetric directional couplers on the chip and decide which would be the best candidates for the phase shift measurement, transmission and reflection measurements were obtained to calculate the SRs of the devices. This data was compared with the results of a simulation which calculated the expected splitting ratio from an asymmetric directional coupler with the design parameters of the device which data had been collected from. By modifying the input parameters to optimise the fit of the simulation to the data, the total generated phase shift that should be expected from the device when the same range of voltage is applied to the device in the phase shift measurement could be extracted from the simulation. Using this information, it was possible to compare the phase shift

measured in the phase shift measurement with the predicted value from the simulation to see how they matched. This made it possible to estimate how predictable the phase shift produced by the device was. Predictability is an important property for the device to have for future purposes of rotating a qubit to an arbitrary position when the device is combined with a symmetric directional beam splitter to create a unitary gate.
In Figure 5.3 the four different ports of an asymmetric directional coupler on the chip are labeled. These labels are useful to keep track of which measurements are discussed when calculating the SR. As can be seen in the figure, ports 1 and 2 are the input ports and 3 and 4 are the output ports.

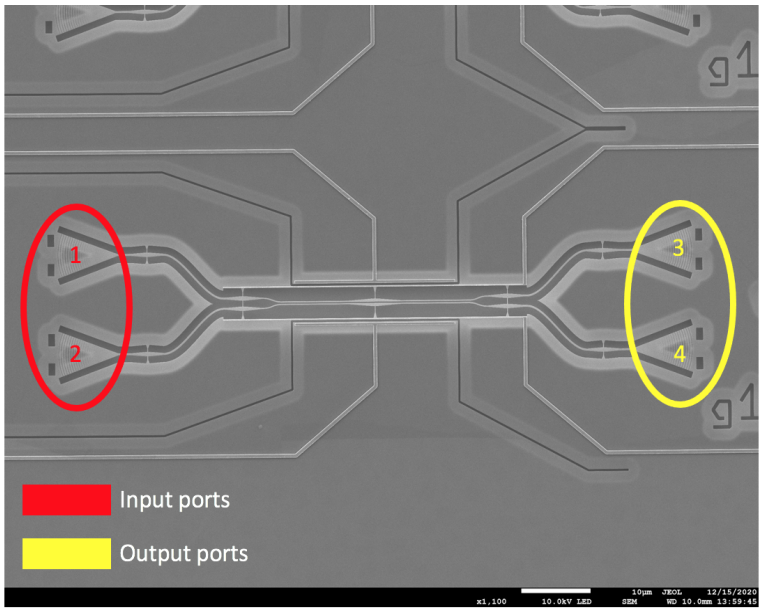

Figure (5.3) This SEM image shows the labeling of the four ports of a typical asymmetric directional coupler. 1 and 2 refer to the two input ports where light is coupled into the device and 3 and 4 refer to the two output ports where light is collected from.

To calculate the SR, four measurements must be made per device, for each voltage applied to the piezo mirror. The method by which these measurements are made is described in more detail in section 7.1.2 These four measurements consist of two transmission and two reflection measurements, where light from a powerlocked SuperK laser [28] (which is a supercontinuum laser) is coupled through one of the two input ports. The collected light measured at one of the two output ports is either the transmission or reflection measurement, depending on where the output port lies in reference to the input port that is being used. Figure 5.4 illustrates how to simplify the asymmetric directional coupler to a conceptual cube beam splitter to help define which output port can be characterised as the transmission port or reflection port depending on which input port is being used.
To show how the SR can be extracted from these measurements, one can begin by stating how the input and output intensities are related through the following matrix:

$$\begin{bmatrix} I_{out3} \\ I_{out4} \end{bmatrix} = \begin{bmatrix} \eta_3 T & \eta_3 R \\ \eta_4 R & \eta_4 T \end{bmatrix} \cdot \begin{bmatrix} \eta_1 I_{in1} \\ \eta_2 I_{in2} \end{bmatrix} \tag{5.3}$$

Here T and R are the transmission and reflection coefficients, η_1 and η_2 the in-coupling efficiencies of port 1 and 2, and η_3 and η_4 the out-coupling efficiencies of port 3 and 4.

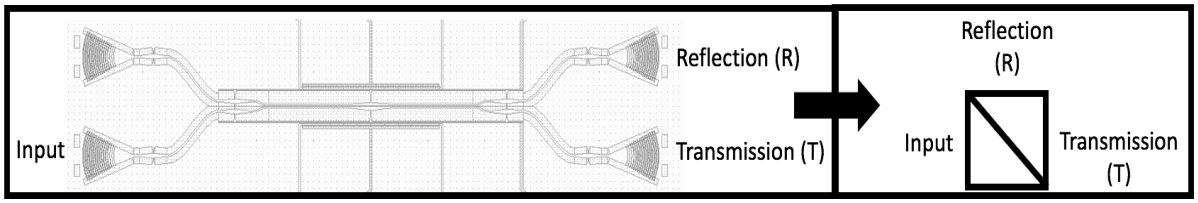

Figure (5.4) This diagram demonstrates how the input port that is being used to couple light through, determines which of the output ports are defined as the reflection or transmission port. One can imagine the asymmetric directional coupler as a conceptual beam splitter to illustrate why it is the port that is diagonal to the input port that is defined as the reflection port and the output port along the same plane as the input port that is defined as the transmission port.

These in- and out-coupling efficiencies take into account the shallow-etched grating and fibre-coupling efficiencies of the devices as well as setup optical losses. By setting the input of one input port to 0 and the other to 1, the matrix can be simplified to the two following expressions depending on which input port is set to 0:

$$\begin{aligned} \begin{bmatrix} I_{in1out3} \\ I_{in1out4} \end{bmatrix} &= \begin{bmatrix} \eta_3\eta_1 T I_{in1} \\ \eta_4\eta_1 R I_{in1} \end{bmatrix} \\ \begin{bmatrix} I_{in2out3} \\ I_{in2out4} \end{bmatrix} &= \begin{bmatrix} \eta_3\eta_2 R I_{in2} \\ \eta_4\eta_2 T I_{in2} \end{bmatrix} \end{aligned} \tag{5.4}$$

One can then define the relations dependent on the reflection and transmission coefficients to describe the intensity going through the device for all four different combinations of input and output devices.

$$\begin{aligned} I_{13} &= \frac{I_{in1out3}}{I_{in1}} = \eta_3\eta_1 T \\ I_{14} &= \frac{I_{in1out4}}{I_{in1}} = \eta_4\eta_1 R \\ I_{23} &= \frac{I_{in2out3}}{I_{in2}} = \eta_3\eta_2 R \\ I_{24} &= \frac{I_{in2out4}}{I_{in2}} = \eta_4\eta_2 T \end{aligned} \tag{5.5}$$

The ratio between the transmission and reflection coefficients of the device, along with a ratio of the out-coupling efficiencies can be extracted from the equations in 5.5:

$$\frac{T}{R} = \sqrt{\frac{I_{13} \cdot I_{24}}{I_{14} \cdot I_{23}}} \tag{5.6}$$

$$\frac{\eta_4}{\eta_3} = \sqrt{\frac{I_{14} \cdot I_{24}}{I_{13} \cdot I_{23}}} \tag{5.7}$$

From the transmission reflection ratio, it is simple to find the SR using the following formula:

$$SR = 10 \cdot log_{10}(\frac{T}{R}) \tag{5.8}$$

Figure 5.5 shows an example of what the transmission and reflection measurements look like for one of the devices on the chip where light is coupled through input port 1. It demonstrates how the spectrum of the light at the two output ports changes from its initial

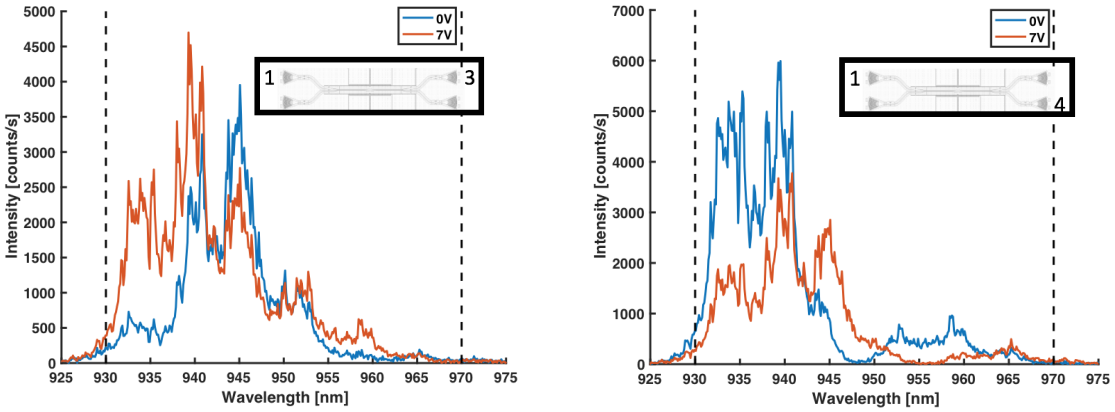

(a) (b)

Figure (5.5) (a) Shows the spectrum of light being coupled through device number 74 from input port 1 to output port 3 when 0 V is applied to the device (blue) and when 7V is applied to it (orange) (b) Shows the spectrum of light being coupled through device number 74 from input port 1 to output port 4 when 0 V is applied to the device (blue) and when 7V is applied to it (orange). The design parameters of device number 74 can be found in the appendix in Table 7.1.

profile when 0V is applied to the device until the final measurement where 7V is applied to the device.

As it appears from Figure 5.5, that by applying 7V to the device, one changes the profile of the spectrum of light being emitted through the two output ports. This is because the applied voltage causes the gap size between the two waveguides to change and hence the coupling of the light through the two waveguides to change as well. This causes the splitting ratio of the light being emitted out of the put output ports to change and thus the spectrum profile as a consequence. The change in intensity of the different wavelengths at the two output ports indicates the beam splitter properties of the devices. As expected, when a very asymmetric device was tested, it did not behave at all like a beam splitter. Figure 5.6 shows an example of the results of a very asymmetric directional coupler. It shows how there is almost no change in the profile of the spectrum of wavelengths being emitted through the two output ports when 7V is applied to the device instead of 0V. One can also see from Figure 5.6 that there is a large difference in intensity between the transmission and reflection measurements regardless of the voltage being applied to the device. This indicated that just how decoupled the two waveguides were as the large difference in intensity was due to very little light being transferred between the two waveguides. These results helped to establish more clearly which devices should have the most focus for the phase measurement, as clearly a device with an asymmetry of 8nm like in Figure 5.6 or more were not good candidates as there was not enough coupling between the two waveguides. The black dashed lines in Figures 5.5 and 5.6 represent the limits where the wavelengths beyond are not transmitted through the grating of the device. This is shown in the appendix in Figure 7.5 where the transmission spectrum of a nanobeam is plotted.

The remainder of this section will focus on device number 74 which was the most successful candidate of the devices tested to show what ideally the SR should look like and how it should be used in connection with the phase measurement of the same device. Figure 5.7 shows how the SR of device number 74 changes as a function of wavelength and voltage and the SR of the simulated data for the same device as a function of wavelength and dis-

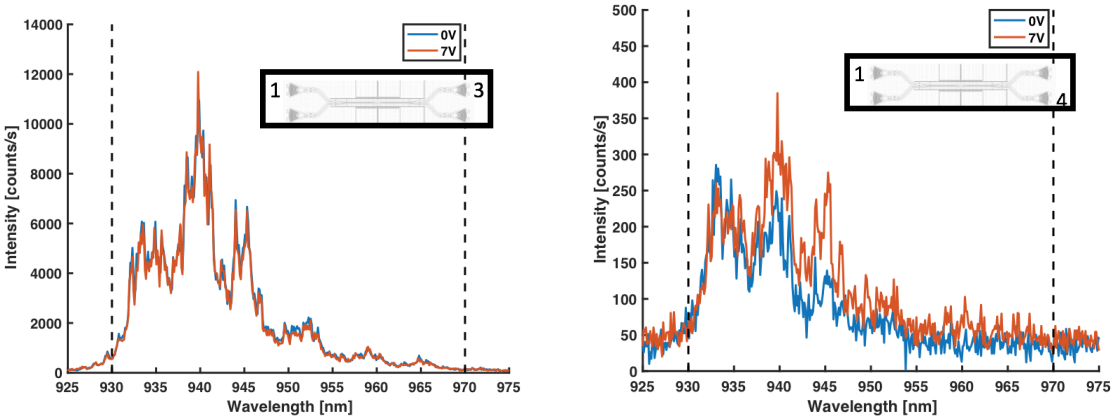

(a) (b)

Figure (5.6) (a) Shows the spectrum of light being coupled through device number 92 from input port 1 to output port 3 when 0 V is applied to the device (blue) and when 7V is applied to it (orange) (b) Shows the spectrum of light being coupled through device number 92 from input port 1 to output port 4 when 0 V is applied to the device (blue) and when 7V is applied to it (orange)The design parameters of device number 92 can be found in the appendix in Table 7.1

placement. It should be noted that displacement means the change in the gap size of the device from its initial gap size. By looking at the SR profile when there is 0V applied to the device and trying to overlay the SR profile of the simulation at 0nm displacement, it is possible to see if the input parameters of the simulation need to be modified to match the SR constructed from data optimally. In the case of device number 74, to get the SR profiles to match, the asymmetry of the device was increased to 1.75nm from the design parameter which was 0nm. The width of the two waveguides in the simulation was also reduced by 10.5nm. Figure 5.8 shows the final result of this overlay. In Figure 7.6 in the appendix one can see how the second derivative of the SR diverges greatly when the wavelength is either less than 930nm or greater than 970nm. It is due to this divergence that the SR data for these wavelengths can be ignored in the analysis of fitting the simulation of the SR to the one calculated from the collected transmission and reflection measurements.

These changes from the design parameters can be justified by taking into account fabrication errors that could have occurred and caused the asymmetry and widths of the waveguides of the devices to vary from the design parameters. This was especially the case for chip 1 where the devices were all undercut which caused the waveguides all to be 40nm narrower than their design parameters.

To test how the displacement and voltage applied to the device are related in the case of device number 74, the SR of the device at 1.8V,3.8V,5.8V and 7V were overlaid with the SR results from the same simulation used to overlay at 0V but at different displacements. By taking note of which displacements are used to overlay the SR plots at different voltages, a relation like the one plotted in Figure 5.9(a) can be made. This plot was fitted with an exponential function and shows that for device number 74, the maximum displacement was reached when a voltage range of 7V is applied is 19nm. In Figure 5.10 one can see how with the fit in Figure 5.9(a), one can now compare, the normalized intensities of the simulation to those calculated from the data with both being a function of displacement.

In this way, one can more precisely see how well the results of the transmission and reflection

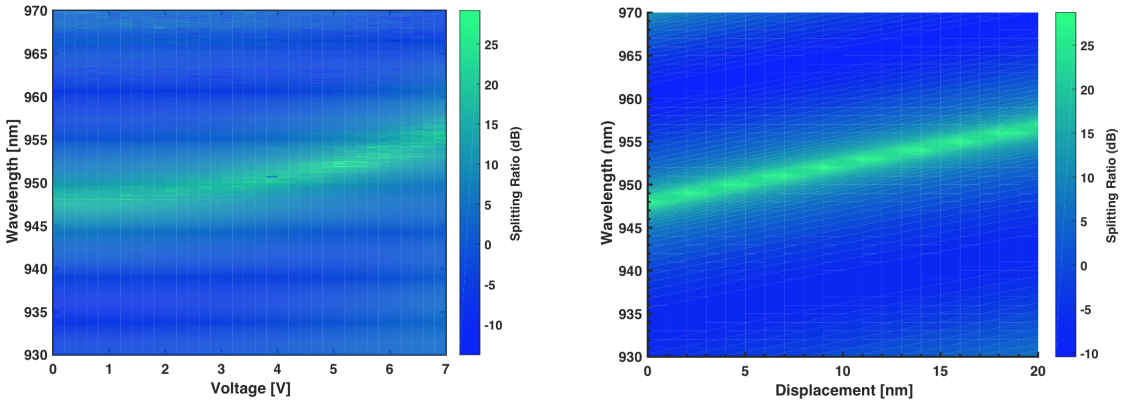

(a) (b)

Figure (5.7) (a) This 3D plot shows the measured SR of device number 74 as a function of both wavelength and applied voltage to the device. The SR is calculated from the normalised transmission and reflection measurements of device number 74 on chip 2. (b) This 3D plot shows the simulated SR of device number 74 as a function of both wavelength and displacement where the input parameters have been modified to optimise the match of the SR profile at 0V as a function of wavelength between the simulation and the SR calculated from the measurements taken of the fabricated device.

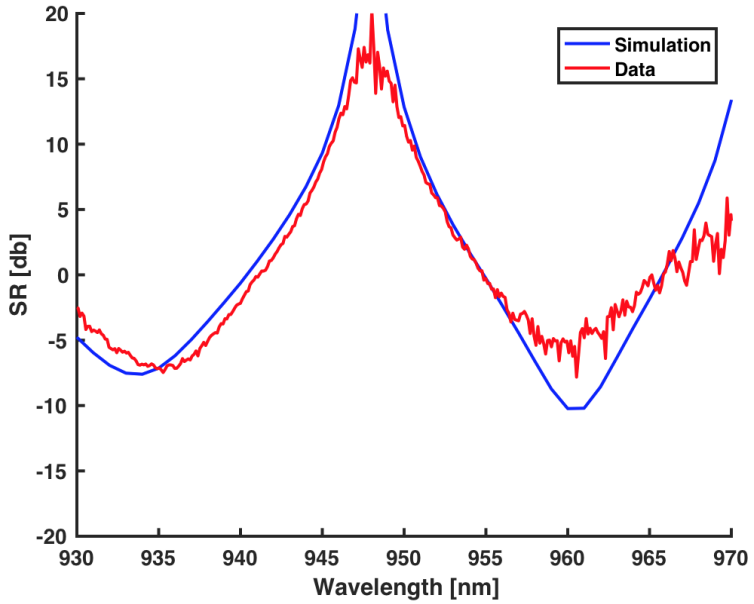

Figure (5.8) This plot shows how the SR of device number 74 looks like as a function of wavelength when 0V is applied to the device. It shows how well the peak and dip of the simulation of the SR (blue) fits with the SR calculated from the normalised transmission and reflection measurements taken of device number 74 on chip 2 (red).

measurements compare to the simulation. In Figure 5.10 the wavelength 945nm is drawn in the four different subplots. This is the same wavelength that the CTL laser is set to for the phase shift measurement as described in section 4.4. One can look along this dashed black line in the subplots to see how well they match. Figure 5.11 shows how the similarities between the simulated and measured transmission and reflection measurements at wavelength 945nm translates into how similar the SR at wavelength 945nm is in simulation compared to the normalized data. As can be seen, the fit of the data and the simulation is best at

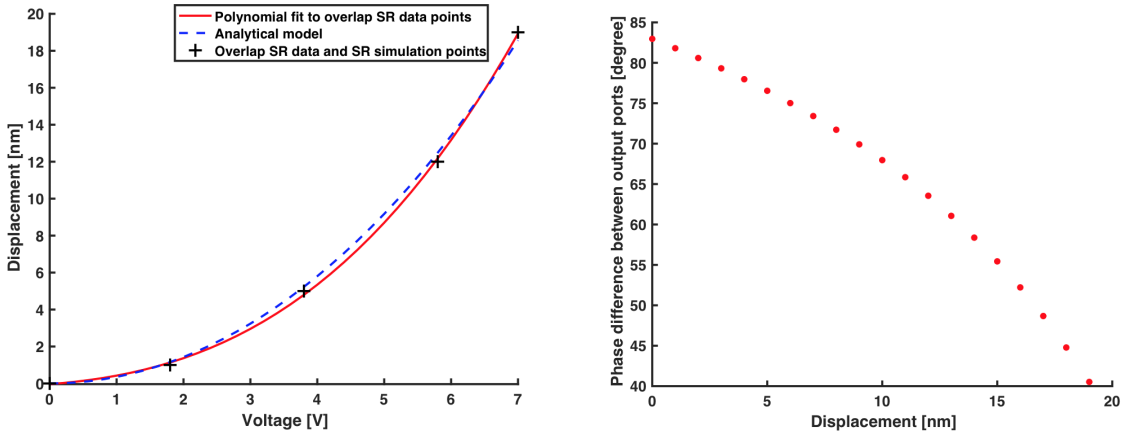

(a) (b)

Figure (5.9) (a) This plot shows which displacements of the SR simulation matched best to the SR made from the collected transmission and reflection measurements of device number 74 for 5 different applied voltages applied to the device. The red curve shows the cubic function that was fitted to these five data points to find the relationship between the applied voltage and the displacement. It shows that for device number 74, the maximum displacement achievable in the applied 7V range was 19nm. (b) This plot shows how in the simulation, the phase difference between the two output ports changes as a function of displacement. The phase difference change between 0nm and the maximum displacement (19nm) is approximately 42.2 degrees.

the smaller displacements and gets worse as the displacement increases. This corresponds with what is shown in Figure 5.10 where the simulation of the reflection and transmission measurements at wavelength 945 nm, match the measured intensity of light along the wavelength 945nm much less when the displacement is greater than 5nm. This could be due to the simulation being based on coupled-mode theory which assumes no loss and uniformity. This would mean that the simulation stops fitting the data when the device has become more lossy and non uniform when it is deformed by having a larger voltage applied to it. From the results of 5.9 part (a), the maximum phase shift the device could produce in a 7V range could be estimated in preparation for comparison to the results of the phase shift measurement. This was done by feeding the maximum displacement the device can achieve at 7V into the simulation and from the output of the simulation the resulting phase shift was given. Figure 5.9 part (b), shows how the simulation predicts how the phase difference between the two output ports will change as a function of displacement. From this plot it can be seen that the predicted phase shift from 0nm to 19nm displacement is approximately 42.2 degrees.

Electrostatic actuation

In Figure 5.9 part (a), the dashed blue line represents the relation between the displacement of the directional coupler and the voltage applied to it derived from the electrostatic actuation used to change the gap size of the device. The devices investigated in this project used electrodes attached to each waveguide of the device by tethers to create a displacement which moved the waveguides away from each other. As stated earlier, the displacement of the waveguides was induced by a voltage being applied to the devices. As a result, an attractive electrostatic force pulls the electrodes closer to each other and moves the waveguides

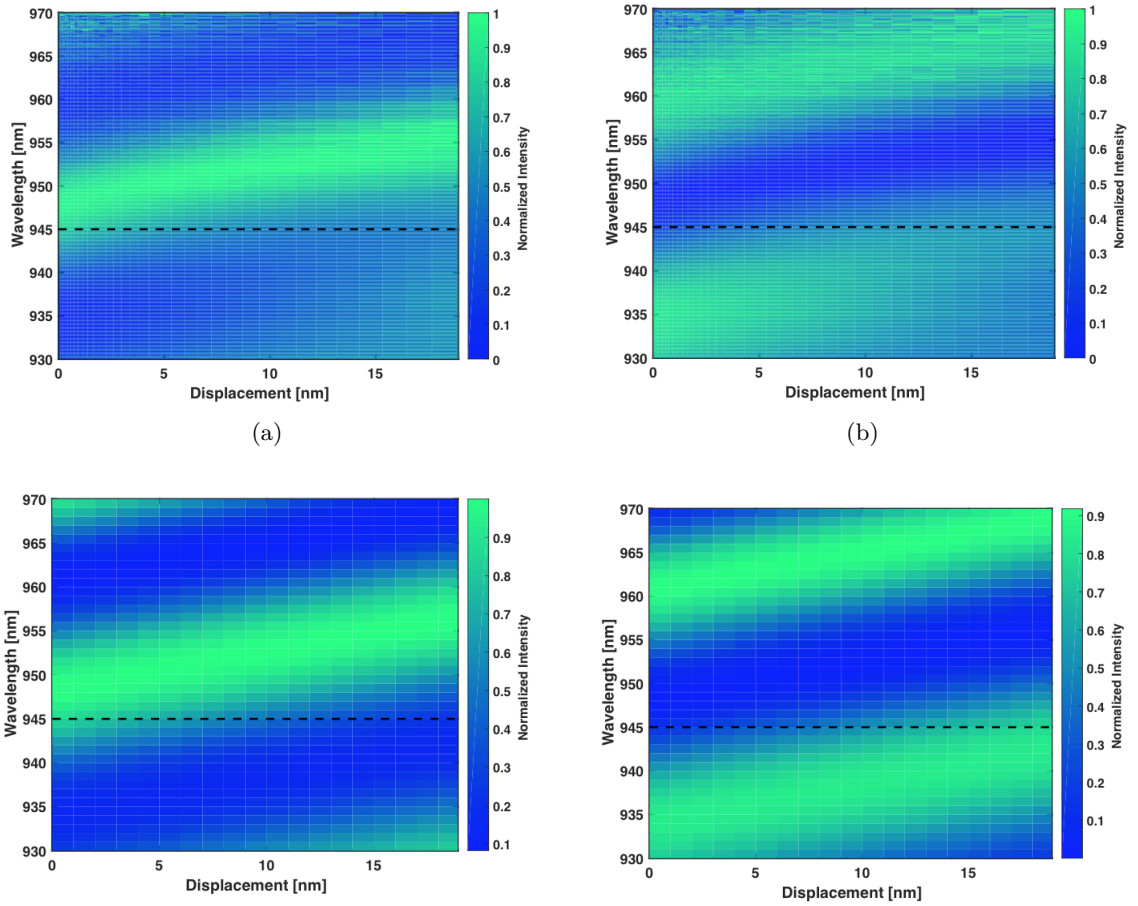

Figure (5.10) (a) Transmission measurement of device number 74, displayed as a function of wavelength and displacement.(b) Reflection measurement of device number 74, displayed as a function of wavelength and displacement.(c) Simulated transmission measurement of device number 74, displayed as a function of wavelength and displacement.(d) Simulated reflection measurement of device number 74, displayed as a function of wavelength and displacement. The coloured dashed lines in each of the four subplots represent the wavelength 945nm and are used to highlight in Figure 5.11 how the intensity changes as a function of displacement for one wavelength.

further away from each other. Figure 5.12 illustrates what this change in displacement looks like. To calculate how the displacement changes as a function of voltage analytically, one can begin by considering the actuators as two capacitor plates which are parallel to each other. In this case the total position-dependent capacitance of the system can be defined thus:

$$C_{tot}(y) = \epsilon_0 L_s \left(\frac{t_0}{d_0 - y} + \frac{t_m}{d_m - y}\right) \tag{5.9}$$

Where, ϵ_0 is the vacuum permittivity, t_0 and is the thickness of the GaAs beams and t_m the thickness of the metal lines. L_s is the shuttle length and d_0 and d_m are the distances at rest between the GaAs beams and metal lines respectively. If $t_m < t_0$ and $d_m > d_0$, then the capacitance of the system can be approximated to be $C = \epsilon_0 \frac{L_s t_0}{(d_0 - y)}$. A further approximation made in this analytical model is that the shuttle which is attached to the waveguide are two beams in parallel to each other with fixed ends and that the force applied to them is uniform. Having taken these approximations into account, the total stiffness of

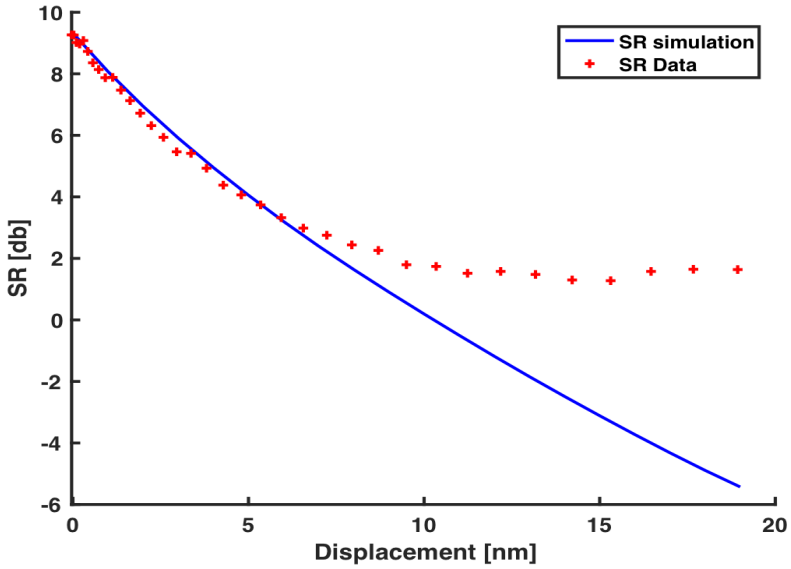

Figure (5.11) This figure shows how the SR for device number 74 changes for one wavelength (945nm) as a function of displacement. The blue curve represents the simulated SR and the red crosses are the SR constructed from the transmission and reflection measurements taken of device number 74. By plotting these two SR curves on the same plot, one can clearly determine how well the simulated SR and the SR calculated from the transmission and reflection measurements match. The plot shows that approximately after 8nm displacement the simulated SR values begin to diverge drastically from the data based SR.

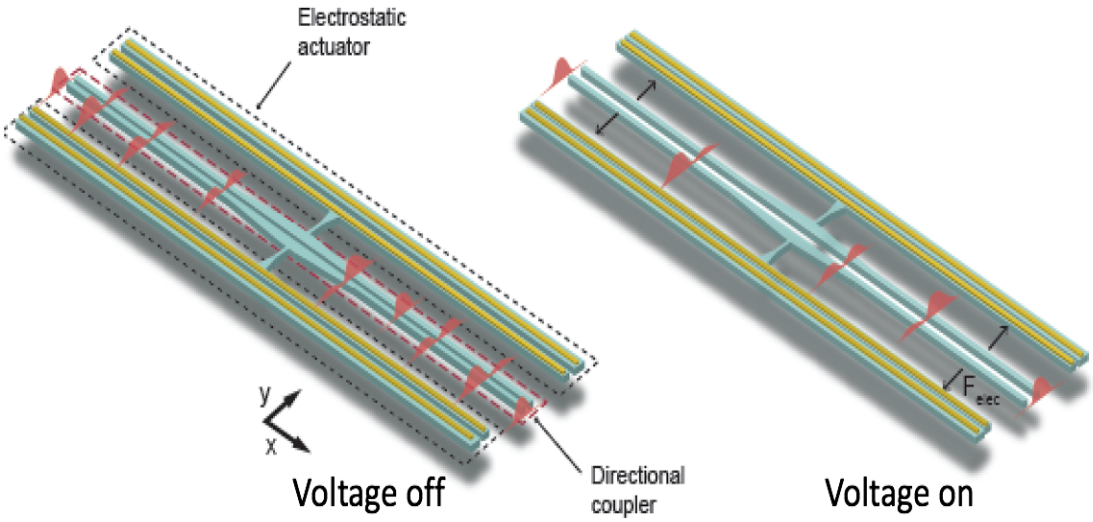

Figure (5.12) This figure shows how the two waveguides (blue) which make up the directional coupler are each attached by a tether to an electrode (yellow) which lies parallel to a second electrode. It shows that when the voltage applied across the electrodes is turned on, an electrostatic force (F_{elec}) pulls the electrodes towards their parallel partner electrode causing the distance between the waveguides to increase. The change in the coupling of the modes in the two waveguides is indicated by the transfer of optical power coming out of different waveguides when the voltage is turned on compared to off. This figure is taken from Camille Papon's master thesis [14]

the system can be defined as:

$$k_T = k_{wg} + k_s = 384E(\frac{I_{wg}}{L_{wg}^3} + \frac{I_s}{L_s^3}) \tag{5.10}$$

where E=85.9 GPa, which is the Young modulus of GaAs, I_s and I_{wg} are the moment of inertia of the shuttle and waveguide respectively along the y direction. Here inertia (I) is defined as $I = \frac{tw^3}{12}$. L_{wg} is the waveguide length which consists of the coupling length of the waveguide L_c and the taper length L_{taper}. Using these definitions for the stiffness and capacitance, the reactive force, that is induced by the electrostatic force between the electrodes when voltage is applied across the device, can be determined using Hooke's law. This means that the total potential energy ($\mathcal{E}$) which is stored in the approximated system under an applied voltage (V) is defined as:

$$\mathcal{E} = \frac{k_T y^2}{2} - \frac{\epsilon_0 L_s t_0 V^2}{2(d_0 - y)} \tag{5.11}$$

where y is the displacement that is evaluated at the centre of the shuttle. To get the static solution to this equation, one solves for the equilibrium equation which is obtained when $\frac{\mathrm{d}\mathcal{E}(y)}{\mathrm{d}y} = 0$. The following equation is obtained in this way:

$$y^3 - 2d_0 y^2 - d_0^2 y - \frac{\epsilon_0 L_s t_0 V^2}{2k_T} = 0 \tag{5.12}$$

To get the total displacement from the resting gap size of the directional coupler, one must also find the displacement (y2) from the centre of the other shuttle of the directional coupler with the same equation in 5.12 and add y and y2 together. It is this combined value which is used to plot the dashed blue curve in Figure 5.9 part (a). To generate these values the following parameters were inserted into equation 5.12 to find both y and y2:

- $d_0 = 300nm$
- $L_s = 26\mu m$
- $L_{wg} = 35\mu m$
- $t_0 = 160nm$
- $k_T = 1.15Nm^{-1}$

In earlier projects the value of k_T was found to be lower, approximately $0.7Nm^{-1}$ [14]. A reason why in this project the directional coupler was found to be so much stiffer could be due to the change in material from gold to chromium gold to fabricate the directional coupler. Using the same parameter values and equation 5.12, the plot in Figure 5.13 was also generated to show how the differential for the displacement as a function of voltage changes in accordance with $y_{pi} = \frac{d_0}{3}$. From this figure, it is clear to see that after a certain voltage, there are no longer any solutions for the equilibrium equation. When this is the case, the electrostatic force is greater than the restoring force. This is referred to as the 'pull in' effect [29]. It occurs when the voltage applied across the electrodes is greater than $V_{pi} = \sqrt{\frac{8k_T d_0^3}{27\epsilon_0 L_s t_0}}$, which, for the case of device number 74 is $V_{pi} = 15.80V$. If one applies a voltage to the device which is greater than V_{pi} then there is a risk that the surfaces of

the electrodes will touch and cause them to become stuck. Once this has occurred, the electrodes cannot become unstuck due to Van der Waals and electrostatic forces which are the dominant forces at that scale. To ensure this did not happen, as well as taking the fragility of the devices into account, only a voltage range of 7V was applied rather than going up to a higher voltage closer to V_{pi}.

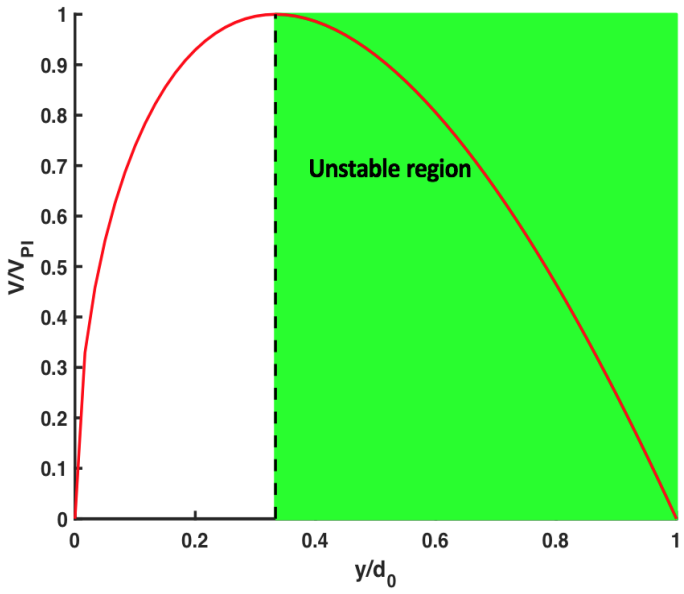

Figure (5.13) This figure shows that if a voltage is larger than what is needed to induce a displacement of the waveguides that is more than a third of the waveguide separation at rest (V_{pi}), then there is no equilibrium between the electrostatic force and the restoring force. Applying a voltage beyond this range, one enters the unstable region of displacement as indicated by the green coloured area of the plot where the pull-in effect occurs and hence limits the maximum displacement achievable.

In the phase measurement described in the next section, the maximum voltage applied to the devices tested was 7V. The reason why only a range of 7V, rather than one going up to a higher voltage closer to V_{pi} was because of the fragility of the chips. Whilst, chips with similar devices had successfully had had voltages applied as high as 10V without issues [14], during initial measurements of chip 1 in this project, a whole column of devices (one third of the devices on the chip) was lost when a voltage of only 5V was applied to it. As a precaution, to avoid this from occurring with any of the remaining columns, and the columns on the future chip 2, voltage was very cautiously applied to the chips. This meant never taking a voltage step larger than 0.2V at a time and manually testing the voltage range by checking the chip with the microscope camera every time a new maximum voltage was applied to the chip before taking any transmission and reflection measurements let alone phase shift measurements. After having completed this cautious process up to 7V it was decided that this was a sufficiently high voltage to characterize the phase shift of the different devices on the chip and low enough to minimize the risk of the damaging more devices with a high voltage.

5.3 Phase measurement

5.3.1 Introduction to phase measurement results

Due to chip 1 breaking before phase measurements could be taken for the devices on it, all phase shift measurements were taken on chip 2. Due to fabrication errors with chip 2, however, the column of devices which had been investigated in chip 1 was short-circuited in chip 2. This meant that the characterization of the devices with the use of transmission and reflection measurements had to be done from scratch in a different column for chip 2. Ideally, it would have been far more stringent to characterize the same devices as on chip 1 to be able to compare the results of the two different chips and thus test if they yielded similar SR results and hence determine how reproducible they were. The devices that were tested in chip 2 are listed in Table 7.1 in the appendix along with their design parameters. Across the devices tested, both the asymmetry and the initial gap size were varied. Measurements from these different devices were taken to test what range of asymmetry was successful in producing an observable phase shift. Another aim was to determine within these asymmetries, how large the gap size could be for the devices to still achieve an observable phase shift in the same voltage range. To define if a device was successful in producing a phase shift, it was necessary to prove that the change in phase observed in the measurement was not the same phase drift which is discussed in section 5.1.2. Another measure of success for the measurement was to analyse how close to the predicted phase shift from the simulation, the actual phase shift measured in the experiment was. In the next section, the results of device number 74 are discussed as this is the device which had the most data collected on it and therefore provided the best data for analysis.
In the next section, the results of the two different phase shift measurements performed in this project are discussed. These two phase shift measurements used the same setup but had different procedures. Though both had a maximum applied voltage of 7V to the chip, one took interference measurements at a larger range of applied voltages than the other which led to the two phase shift measurements varying in duration. This provided an opportunity to further investigate if the phase drift present in the setup was a time-dependent component of error in the phase shift measurement or random.

5.3.2 Results of phase experiment 1 compared to phase experiment 2

This section begins with the discussion of the faster of the two phase shift measurements and will be referred to as phase experiment 1. The slower phase measurement will be referred to as phase experiment 2. Figure 5.14 shows the results of two different phase experiment 1 measurements which both consist of three sequential interference measurements. The method by which this plot was created from the raw data collected during the experiment is shown in the appendix in Figure 7.3. The key difference between the two measurements in Figure 5.14 is that in Figure 5.14 part (b), the voltage source that should provide the voltage to the chip to change the gap size of the devices is disconnected. These results are useful for comparing with Figure 5.14 part (a), where the voltage source was connected. This was as it worked as a sanity check to test if the phase shift that was seen between the first and second interference measurement in Figure 5.14 part (a) was due to the difference in voltage applied to the device (7V) or if the shift was caused by phase drift independent

of any voltage applied to the device, as in the case of Figure 5.14 part (b). Another sanity check was to check if the third interference measurement in Figure 5.14 part (a) consistently had a smaller phase shift between the first and the third interference measurement than the first and the second interference measurement. This was expected as the first and the third interference measurements both had 0V applied to the device whereas the second had 7V applied to it. This means that the only phase shift that should be present between the first and the third interference measurements should be due to phase drift which should be less than a phase shift caused by the gap size changing due to 7V being applied to it.

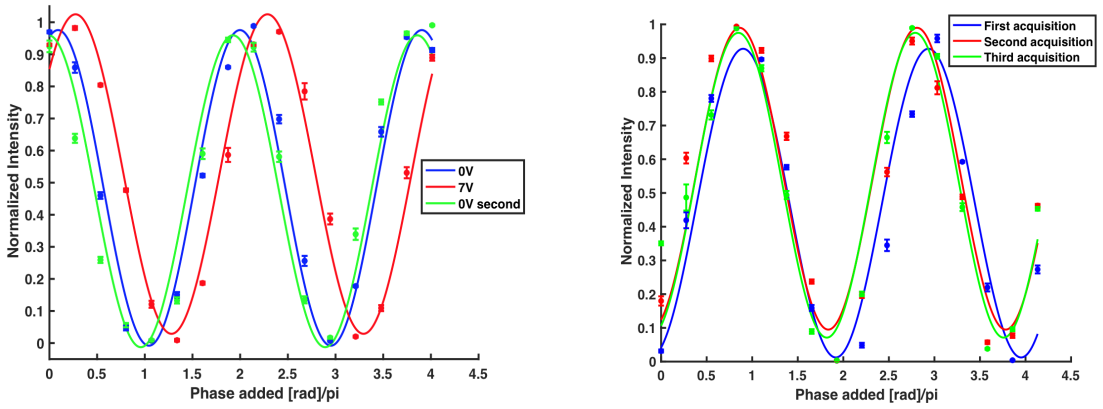

(a) (b)

Figure (5.14) (a) This figure shows the results of the three interference measurements which make up the phase shift measurement. The blue curve is the first interference measurement done where 0V is applied to the device, the red curve is the second interference measurements where 7V is applied to the device and the green curve is the third and final interference measurement, where like the blue curve, 0V is applied. The curves are generated by fitting a sin curve to the averaged intensity data points collected in the phase shift measurement. (b) This plot shows the results of a phase shift measurement done as in (a) but in this case, the voltage source is disconnected from the chip so that 0V is passed through the device in the red curve unlike in (a) where 7V is applied.

The measurements in Figure 5.14 were repeated 6 and 5 times, respectively, for each output. The resulting phase shift between the interference measurement taken at 7V and the interference measurements taken at 0V at the beginning and end of the phase shift measurement were recorded in both the cases where the voltage source was turned on and off for both outputs of the device. For the analysis of the phase shifts measured using phase experiment 1 for device number 74 the data sets collected from each of the two different outputs were combined into one data set. To prove why this was allowed, a Z-test [30] was conducted. The Z statistic that was calculated for this test was found using the following formula:

$$Z = \frac{(\bar{X}_1 - \bar{X}_2)}{\sqrt{\sigma_{X_1}^2 + \sigma_{X_2}^2)}} \tag{5.13}$$

Where X_1 is the mean value of the phase shift from output 3, X_2 is the mean value the phase shift from output 4, σ_{X_1} is the standard deviation of phase shift from output 3 divided by the square root of the number of data points and lastly σ_{X_2} is the standard deviation of phase shift from output 4 divided by the square root of the number of data points. The Z-statistic was in this case found to be 0.093. Generally, when the Z-statistic is below 2, it is assumed that the two samples that have been compared come from the same distribution.

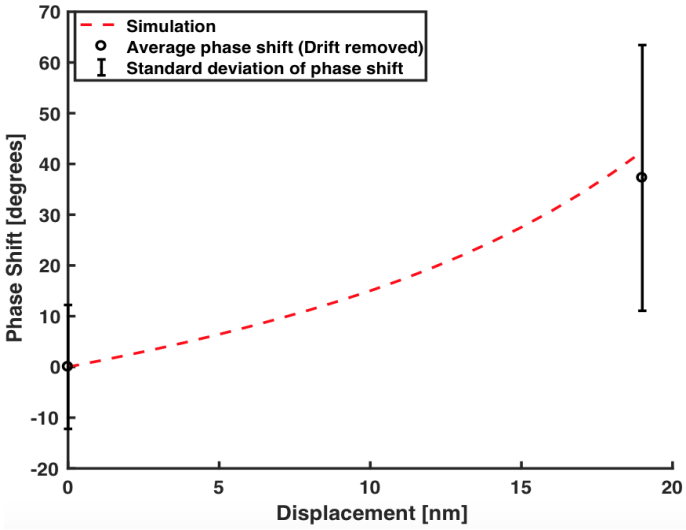

Figure (5.15) This figure shows the results of phase experiment 1 where the black circles are the average phase shifts measured between the initial interference measurement and the interference measurement taken at 7V (where the displacement was 19nm) and the second interference measurement taken at 0V where the displacement is assumed to be 0nm. The black vertical lines show the standard deviation of these same measured phase shifts. These values were calculated by combining the measurements taken at both output ports. The red dashed line shows the results of the simulation of how the phase shift is expected to change as the displacement changes. As this simulation assumes no drift, the average value of the phase drift that is measured between 7V and 0V interference curves when the voltage source is turned off is artificially removed from the phase shift measured when the voltage source is turned on to better compare the results of the simulation to those measured in phase experiment 1.

The mean phase shifts for when the voltage source is connected and disconnected are 55.5 degrees and 18.3 degrees respectively. The standard deviations are 26.2 degrees and 12.2 degrees respectively. In Figure 5.15 one can see the mean value of the phase shift achieved in phase experiment 1 when the voltage source is turned on with the phase drift removed to better compare it to the predicted value of the phase shift we get from the simulation. Here, the phase drift is assumed to be the average value of the phase shift measured between 0V and 7V when phase experiment 1 was conducted with the voltage source turned off. At 0nm displacement, one can see the standard deviation of this phase drift plotted as error bars and at 19nm displacement the error bars are the standard deviation of the phase experiment 1 measurements when the voltage source was turned on. One can observe in Figure 5.15 that the red dashed line which denotes the phase shift predicted by the simulation, fits closely to the measured value of the phase shift which is encouraging. However, one can also observe that the error bars for the phase drift and shift are both very large and hence questions how well the results of phase experiment 1 and the simulation fit together. Had there been more time and fewer issues with the Keithley (voltage source) freezing, more repetitions of phase experiment 1 would have been optimal to improve the statistics and thereby getting more confidence in what phase shift this device can achieve when 7V is applied to it compared to the simulations and the phase shift caused by phase drift in the same time period.

The phase measurement data collected when conducting phase experiment 1 when the voltage source was turned on and off respectively generated two data sets which were not

normally distributed. This was proved by plotting qq plots of the collected data which are shown in the appendix in section 7.4. This, along with the low number of measurements conducted, eliminated the possibility to perform a student t-test to test if applying voltage caused a significant phase shift in the device compared to phase drift.

Instead the Wilcoxon rank sum test [31] was used in this thesis to test if the data set of phase experiment 1 where the voltage source is turned on had a statistically different median from the data set of phase experiment 1 where the voltage source was turned off.The Wilcoxon rank sum test is equivalent to a Mann-Whitney U-test. The advantages of using this type of statistical test of significance are that firstly, it can be used for non-parametric distributions and secondarily, the two distributions it is comparing can be different sizes. The data of the two phase measurements also follows the two conditions in that they follow continuous distributions and are independent of each other. The p-value of the Wilcoxon rank sum test was found to be 0.00065 when comparing the two distributions of the phase shift between 0V and 7V when phase experiment 1 was conducted with the voltage source was turned on and off respectively. This means that at a 5 % significance level, the null hypothesis of the two phase shift measurements having equal medians can be rejected. This suggests that the voltage applied to the device does indeed cause a change in phase shift which is different from the phase drift which would have happened independently of the voltage being applied in the measurement. What is also interesting to see is if the phase shift measured between 0V and 7V in phase experiment 1 is significantly larger than the phase shift measured between the initial and the final interference measurement conducted at 0V. This would give a good indication that the phase shift caused by 7V being applied to the device is significantly different from the phase drift that the setup undergoes in the time that phase experiment 1 takes to complete. In Figure 5.16 part (a) there is plotted as two histograms, the phase shift measured between 0V and 7V for device number 74 and the phase drift measured between the first and the final interference curve measured at 0V for device number 74. In part (b) of this figure, one can see the same distribution of phase shift between 0V and 7V for device number 74, but unlike in part (a), this time the histogram is compared to the distribution of all the phase drift measurements between the two interference measurements conducted at 0V for phase experiment 1 from all of the different devices. The reason that the measurements of phase drift can be collected together into one distribution is that the drift measured is device independent. The advantage of combing the drift measurements from all the devices is that it increases the statistics significantly from those collected from device number 74 only. However, the advantage of comparing the phase shift of device number 74 to the phase drift of only device number 74, is that in the case where the drift is unexpectedly not device independent then one can still see if the median of the drift is significantly different than the phase shift measured with phase experiment 1 for device number 74.

For both of the pairs of histograms in Figure 5.16, a Wilcoxon rank sum test was performed. One for the phase shift and each of the two different groups of phase drift. The p-value for the Wilcoxon rank sum test between the phase shift and the phase drift collected only from device number 74 was found to be 0.0157 which for a 5% significance level means that the null hypothesis of the two medians being the same can be rejected. In the case of the phase shift and the phase drift collected from all the devices tested, the p-value was 0.00068 which again meant that the null hypothesis was rejected. These results help support the claim

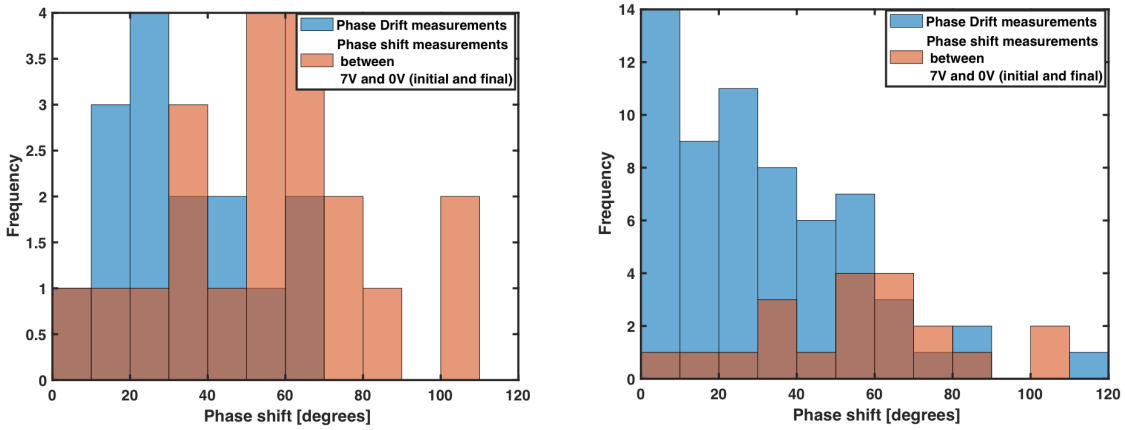

(a) (b)

Figure (5.16) (a) The orange histogram in the plot denotes the distribution of the phase shifts measured between the interference curve recorded at 7V and the interference curves measured at the beginning and end of phase experiment 1 for device number 74. The blue histogram in the plot denotes the distribution of phase drift recorded between the interference curves measured at the beginning and end of phase experiment 1 for device number 74. (b) The orange histogram in the plot denotes the distribution of the phase shifts measured between the interference curve recorded at 7V and the interference curves measured at the beginning and end of phase experiment 1 for device number 74. The blue histogram in the plot denotes the distribution of phase drift recorded between the interference curves measured at the beginning and end of phase experiment 1 for all the different devices which underwent phase experiment 1.

that in these time duration and applied voltage range conditions, it is possible to observe a phase shift caused by the device which is larger than the phase drift accumulated during the measurement.

Having established that the voltage applied to the chip causes a phase shift larger than phase drift present in the phase shift measurement setup when conducting phase experiment 1, one can see if this still holds true when conducting phase experiment 2 with the same setup but with a measurement with a longer duration in the following section. A comparison between the phase shift results obtained with phase experiments 1 and 2 and the simulation of the phase shift for all the tested devices will be discussed in section 5.3.3.

Results of phase experiment 2

In the case of phase experiment 2, Figure 5.17 exemplifies what the interference measurements look like in this procedure. As a sanity test to check that applying a larger voltage corresponds to a larger phase shift in the device, it can be observed that the peaks of the interference curves shift increasingly to the right as the voltage is increased and then moves back towards the original position of the first interference measurement when the voltage applied to the device is again 0V.

This measurement was repeated 6 times at each output to test if the pattern shown in Figure 5.17 was repeated in each of the iterations of the phase experiment, as should be expected. In Figure 5.18, the mean phase shift with the mean phase drift removed for each applied voltage measured in phase experiment 2 is plotted along with the phase shift which the simulation predicts the device will produce. It is clear to see from the mean values of phase shift, that the phase shift appears to increase as a function of voltage applied. One

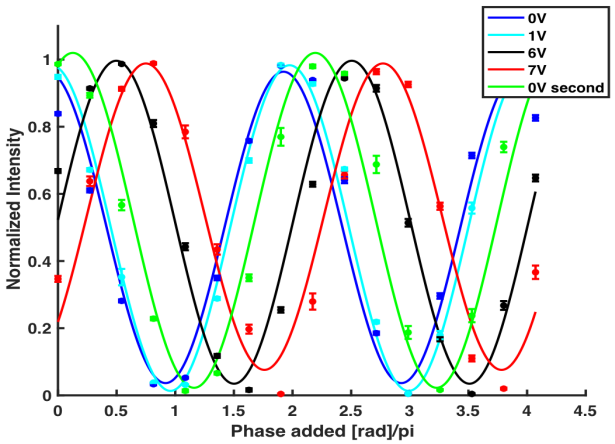

Figure (5.17) This figure shows an example of the five interference curves produced by a phase experiment 2. The blue curve is the initial interference measurement done at 0V, the turquoise curve is when 1V is applied to the device, black when it is 6V, red when it is 7V and green when 0V again at the end of the phase shift experiment.

can also observe from the error bars that there is a lot of variation in the size of the phase shift generated by the device when the same voltage is applied to it. It is also important to observe how large the variation in the phase drift, plotted at 0V on Figure 5.18, is for these measurements; specifically how the error bars overlap with the phase shift produced by applying 7V to the device.

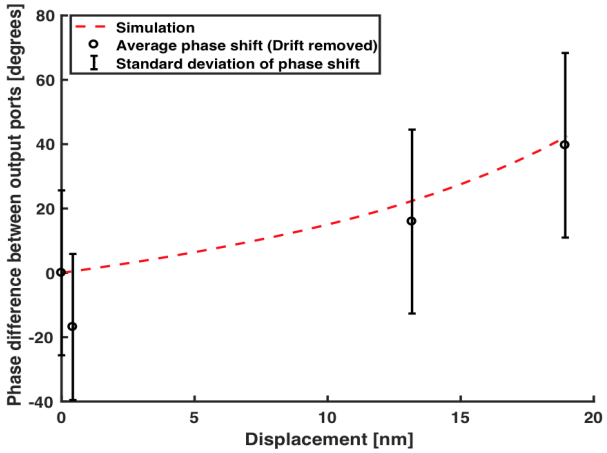

Figure (5.18) A plot to show the mean phase shift between the initial interference measurement of phase experiment 2 and the interference measurements done at 1V, 6V,7V and the second interference measurement done at 0V. The mean phase shift is calculated from the phase shifts taken from both output ports, as are the error bars, which represent the standard deviation of the different the phase shifts. The red dashed lines show the results of the simulation of how the phase shift is expected to change as the displacement changes. As this simulation assumes no drift, the average value of the phase drift that is measured between the two interference measurements taken at 0V is artificially removed from the average phase shifts found at the different applied voltages measured to better compare the results of the simulation to those measured in phase experiment 2.

This overlap is more closely examined in Figure 5.19 where the 6 phase measurements taken at the two different output ports of device number 74 are plotted along with the mean phase shift calculated only from the measurements of the respective output port that the mea-

surements were collected from. These plots emphasize the linearity of the data between 1V, 6V, and 7V, and the consistency of this effect over the different measurements for the same output. The one measurement that does not follow this trend is measurement number 6 in output 4. The reason for this is uncertain, however one possibility could be that the voltage source for some reason failed to apply the correct voltage to the device. This could be because of a current surge in the voltage source which would cause the voltage source to limit the voltage going to the device because of the current limit on the voltage source that was in place to protect the chip from a sudden increase in current. The trend for the phase shift caused by 1V being much smaller than 7V is a positive sign when considering Figure 5.9 which shows how the simulation predicts how the phase shift changes as a function of displacement which is regulated by the applied voltage. As the voltage and displacement are exponentially correlated, it means that for small voltages such as 1V, there is very small displacement compared to larger voltages such as 6V or 7V. This means that it can be expected that the phase shift generated by 1V is a lot smaller than that of 6V or 7V. While

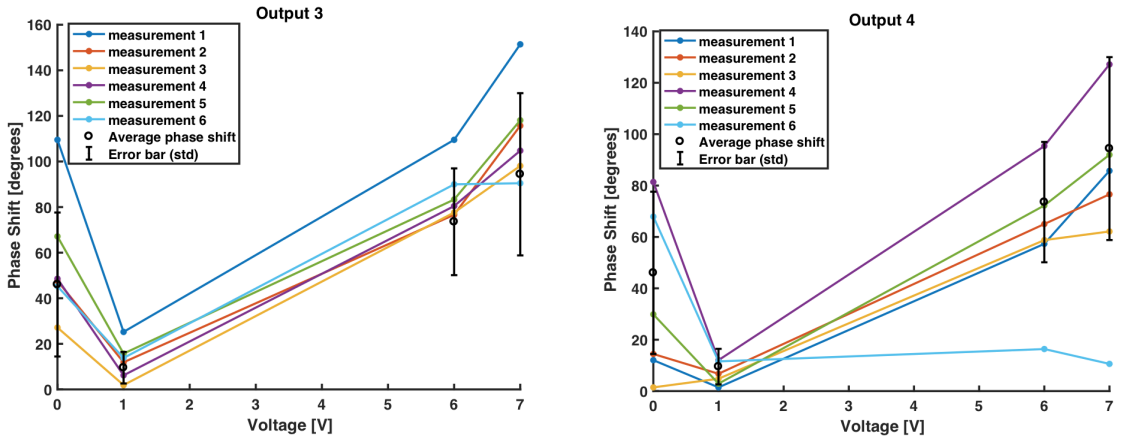

(a) (b)

Figure (5.19) (a) A plot to show the mean phase shift between the initial interference measurement of phase experiment 2 and the interference measurements done at 1V,6V,7V and the second interference measurement done at 0V. The mean phase shift is calculated from the phase shifts taken from output port 3, as are the error bars, which represent the standard deviation of the different phase shifts. The coloured lines represent the iteration of the phase shift experiment 2 done at output port 3 (b) A plot to show the mean phase shift between the initial interference measurement of the phase experiment and the interference measurements done at 1V,6V,7V and the second interference measurement done at 0V. The mean phase shift is calculated from the phase shifts taken from output port 4, as are the error bars, which represent the standard deviation of the different the phase shifts. The coloured lines represent the iteration of the phase shift experiment 2 done at output port 4

this repeatable linearity is promising in showing that applying a 7V voltage range to device number 74 produces phase shift, it must still be argued more quantitatively that this phase shift is not simply a change in phase drift. In Figure 5.20 part (a) the data of the phase drift between the two interference measurements taken at 0V is shown along with the phase shift from the interference measurement between the initial 0V and 7V and the one between the final 0V interference measurement and the one at 7V. The data shown in this histogram is used to determine if there is statistically significant evidence to conclude that the median of the phase shifts collected when 7V is applied is different from the phase shift caused by

phase drift in the setup between the two 0V interference measurements. A Wilcoxon rank sum test was used to test if the two phase measurements have equal medians or not. It was found that when only taking into account the phase drift measurements from device number 74, the p-value was 0.0014 which meant that the null hypothesis of the two medians of the two distributions plotted in Figure 5.20 part (a) being the same was rejected.
As the drift data sample collected for device number 74 was small, all the phase drift measurements for phase experiment 2 for all the different devices were taken into account and compared to the phase shift of device number 74 to see if by having a bigger and hence better representative sample of drift data would change the conclusion that the phase shift produced by applying 7V to device number 74 produced a significantly different phase shift than drift. Figure 5.20 part (b) shows these two different distributions plotted on one histogram. The p-value of the Wilcoxon rank sum test conducted between these two distributions was found to be 0.000000047 which is below the 5 % significance threshold. This means that the null hypothesis that the two medians are the same was rejected. This means, just like with phase experiment 1, where for the corresponding comparisons, the null hypothesis was rejected for both.

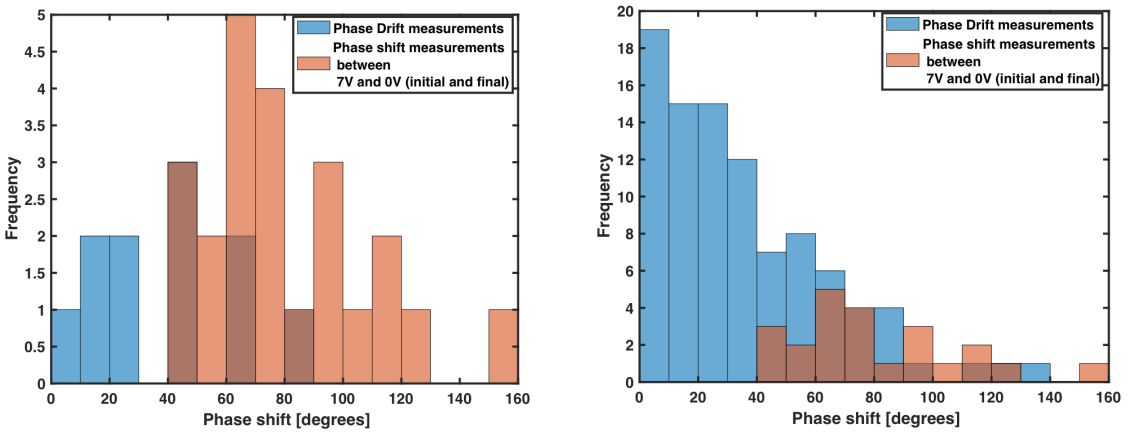

(a) (b)

Figure (5.20) (a) The two histograms in this plot show the combined phase shifts distributions between the interference measurement when 7V is applied to the device and the first interference measurement taken at 0V and the second interference measurement taken at 0V (orange) and the phase drift between the first and the second interference measurements taken at 0V (blue) for phase experiment 2 on device number 74. (b) Of the two histograms shown in this plot, the orange one shows the same as in part (a), and the blue histogram shows the phase drift between the first and the second interference measurements taken at 0V (blue) for all the devices where phase experiment 2 was performed.

To test if there was a difference in the phase drift between the two phase measurements, the two distributions of phase drift shown in Figure 5.21 were compared with a Wilcoxon rank sum test. The p-value of this test was found to be 0.6110 which means that for a 5 % significance threshold the null hypothesis cannot be rejected and the two medians of the distributions are equal. What this suggests is that the increase in the time to complete phase experiment 2 compared to phase experiment 1 did not affect the median value of the phase drift occurring during the experiments. This supports the finding of section 5.1.2 where the drift data collected is plotted in Figure 5.2 and appears to show no correlation between time and drift in the setup. This supports the assumption that the drift in the setup has

an inherent randomness. However, to conclude if the phase drift was time dependant or not, as mentioned in section 5.1.2, more phase measurements which vary in duration are needed. The two data times of the time duration of phase experiments 1 and 2 are simply not enough to suggest that the increase in phase drift in phase experiment 2 is due to it taking 8 minutes rather than 3 minutes like phase experiment 1. More data points would also have the benefit of adding confidence to the conclusion of the Wilcoxon rank sum test done with the currently available data.

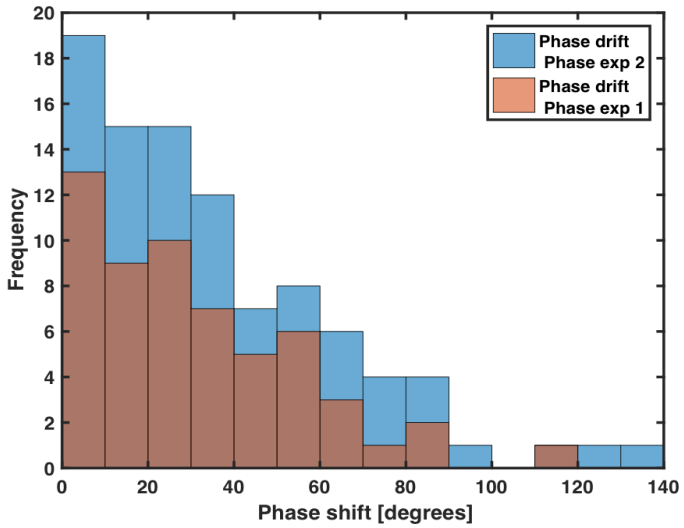

Figure (5.21) These two histograms show the distributions of phase drift measured between the first and the second interference measurement taken at 0V from phase experiment 1 (orange) and phase experiment 2 (blue) for all the devices tested for each type of phase experiment.

5.3.3 Comparison between measured and simulated phase shifts for tested devices

This section contains a summary of all the measured phase shifts achieved by the different devices investigated on chip 2. Table 5.1 contains the values of the mean phase shift with the mean phase drift removed when 7V was applied to the device for all the devices which underwent both phase experiments 1 and 2. The average drift was removed from the mean phase to more clearly compare the phase shifts achieved by the devices to the simulated phase shifts which are also in 5.1. The simulations have been fitted to the data of the devices in the same way as described in section 5.2. The simulated values are very different from those phase shifts measured using phase experiments 1 and 2 for all devices other than device number 74. This suggests that the simulation, despite being optimised for each of the devices, was not a good predictor of the phase shift produced by the devices tested on chip 2. Fabrication errors of the devices are a likely major source of causing sub-optimal prediction as they can cause (i) devices to have rough edges and (ii) non-uniformity which in both cases would make the simulation less capable of predicting the behaviour of the light in the waveguides as the coupled-mode theory used to create the simulation assumes that the waveguides are uniform and that there is no loss in the system. Evidence to suggest that fabrication errors may have been the cause of the difference between the obtained data and the simulated phase shifts is based on the observation that the parameters used to fit

the simulation to the SR data of the device varied greatly from the design parameters of the devices used to fabricate the devices. To get a better idea of what phase shift values should be expected of the devices, a more complicated 3D simulation must be made to factor in the effects of loss and non-uniformity.

Figure 5.22 part (a) shows the mean phase shift achieved by the different devices when phase experiment 1 was performed where the mean drift for each of the measurements has been subtracted. The error bars are the standard deviation of the mean values. Figure 5.22 part (b) shows the mean phase shift achieved by the different devices when phase experiment 2 was performed where the mean drift for each of the measurements has been subtracted. In Figure 5.22 part (a), when focusing on the average phase shift achieved by applying 7V to the device, it appears that for device numbers 90 and 96, there is very little phase shift, particularly for device number 96. This is expected as these devices have asymmetries so large that the waveguides are not well enough coupled to generate a significant phase shift in the voltage range that was tested. From Figure 5.6 one might imagine how the transmission and reflection spectrums displayed there for device number 92 would appear similar to those of device numbers 90 and 96 in that there would be very little change in the spectrum profile when 0V is applied to the device compared to 7V. This would indicate how weak the beam splitter properties of the device is and hence according to section 2.2 explains why the devices only produced a small phase shift. For device numbers 73 and 74, which from their design parameters were both supposed to be symmetric, Table 5.1 shows that both produce significant phase shifts which are different from each other by over 20 degrees. This suggests that both were asymmetric and hence differed from their design parameters. Device numbers 79 and 80 have design parameters with an asymmetry of 2nm, device number 82 of 4nm and device number 87 of 6nm. When looking at the average value of the phase shift at 7V, device number 79 achieves the greatest phase shift in the tested voltage range. Device number 82 does not seem to fit the theory that there is an optimal asymmetry for achieving the largest phase shift in a specific voltage range, where the further away it is from this optimal value, the smaller the phase shift achieved will be. It achieves a smaller phase shift than device number 87 which has design asymmetry which is 4nm different from device number 79 whilst device number 82 only has a difference of 2nm. One possible explanation might be due to the difference in the designed gap size which was 124 nm for device number 82 and only 100 nm for device number 87. As discussed in section 2.2, many factors can affect the phase shift produced by an asymmetric direction coupler. However, as, for example, shown in Figure3.4, the larger the gap size (waveguide separation) the flatter the slope of phase shift. Thus, the larger the initial gap size is, the smaller is the expected phase change over a defined increase in waveguide separation. Fabrication errors could have also exacerbated the difference in gap size between the devices. As exemplified for device number 82, the gap size could have been so large that the light was close to being uncoupled between the two waveguides and hence produced a phase shift closer to those produced by devices 90 and 96 where the light was uncoupled due to their excessive asymmetry. Figure 5.22 part (b) shows that it is necessary to apply a voltage larger than 1V to record a phase shift. Thus, the phase shifts (with the phase drift removed) for all the tested devices were negative when 1V was applied to the device. This indicates that the phase shift generated by applying 1V to the device was smaller than the average drift of the phase. When comparing the average phase shifts generated by applying 7V to the

Device number	Difference in waveguide width (design parameters) [nm]	Simulation Phase shift for 7V [degrees]	Phase shift for 7V [degrees] Phase experiment 1	Phase shift for 7V [degrees] Phase experiment 2
73	1	166.25	57.5±12.2	62.8±31.2
74	1.75	42.2	37.2±22.5	39.7±28.7
79	-1	215.9	86.4±21.8	81.2±19.3
80	0	149.28	83.2±26.0	78.6±33.4
82	-1.5	26.1	17.8±21.5	15.0±25.3
87	-2.5	24.96	76.2±24.0	72.6±32.4
90	0	0	-16.9±17.0	-9.4±19.0
96	2	0	4.4± 8.2	-8.3±23.2

Table (5.1) This table shows the phase shifts achieved when performing phase experiments 1 and 2 on 8 different devices after the phase drift of the measurement has been removed, as well as the phase shift which the simulation predicts they will achieve when it has been fitted to the SR data as described in section 5.2. In the table one can also see the difference from the design parameter of the asymmetry of the device to the asymmetry which the simulation ends up having to fit the SR data measured for each device.

devices displayed in Figure 5.22 parts (a) and (b), there is a consistent pattern for which devices produce the highest to the lowest voltage induced phase shifts. Particularly, and once again, device numbers 90 and 96 fail to produce a measurable phase shift larger than the drift in the tested voltage range as the phase shift remains negative even when 7V is applied. For the remaining devices, one an see that the average value of the phase shift increases between the applied voltages 6V and 7V for all the devices except device number 79. The reason for this could be an outlier measurement taken at 7V which skewed the average phase shift so that it appears to be lower than the average phase shift at 6V.
In conclusion, these results reflect the hypothesis put forward by the results of the simulations in section 3.1 that there exists an optimal design for a phase shifter which is not necessarily improved by increasing the asymmetry but by balancing the asymmetry with the other parameters of the device such as gap size. For the devices tested, the optimal asymmetry appears to be 2 nm when the gap size is 100 nm and the coupling length of the device is 35 nm. When inspecting the predicted phase shifts of the simulations of the device, it appears that the device that is expected to be the best phase shifter in the voltage range tested was device number 79.

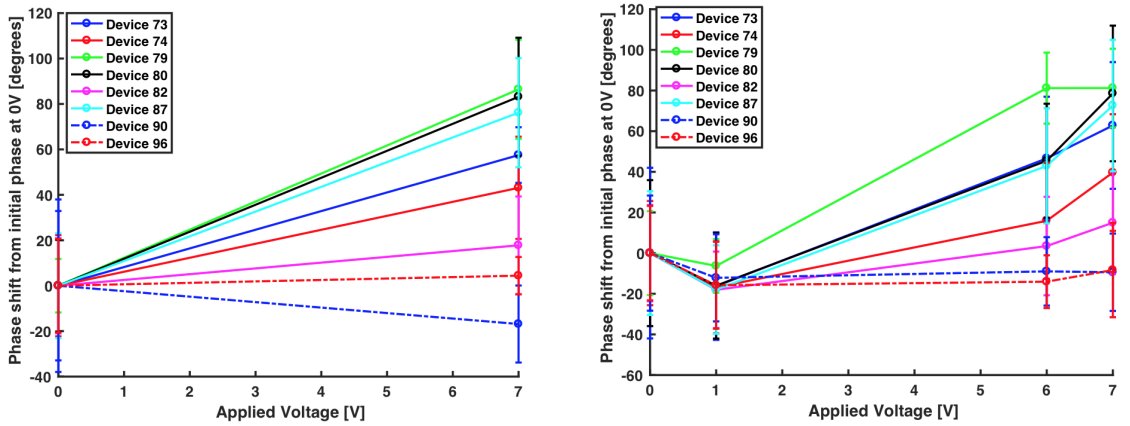

(a) (b)

Figure (5.22) (a) In this figure, one can see the phase shift achieved by performing phase experiment 1 for 8 different asymmetric phase shifters, all located in the same column of the chip. For each of phase shifts, the drift in phase that is independent of the voltage being applied to the chip is defined as the change in phase between the initial interference measurement at 0V and the final one and is subtracted from the phase shift between the initial interference measurement at 0V and the one taken at 7V. This allows for a better comparison of the phase shift produced by the different phase shifters when 7V is applied to the chip. The magnitude of the error bars shows that for all of the different phase shifters, there is considerable variation in the phase shift which they produced. (b) In this figure, one can see the phase shift achieved by performing phase experiment 2 for the same 8 devices as in part (a). The coloured points shown are the average value of the phase shift achieved for the different devices at the voltages 1V, 6V and 7V where the drift has been subtracted as in part (a). As with the phase shifts achieved in phase experiment 1, one can see that with device numbers 90 and 96, there does not appear to be an observable phase shift achieved in the voltage range of 7V. Another similarity with phase experiment 1 is that device number 79 achieves the greatest change in phase in a 7V range, though there seems to be no increase in phase shift between 6 and 7V which is neither observed with device numbers 73, 74, 80, 82 nor 87.

Chapter 6

Ongoing experiments and outlook

6.1 Improved phase shift measurement setup and results

The results reported and discussed in this section were obtained two months after the results described in the previous section. In these two months, modifications were made to the setup by Rodrigo A. Thomas and Nicolas Remy Høegh Pedersen, two other members of the Niels Bohr quantum photonics group. These modifications were done to increase the speed at which the phase shift measurements could be obtained. By decreasing the time period of the measurements they could successfully decrease the drift occurring throughout the measurement as will be described in this section. Figure 6.1 shows a schematic of the new experimental setup used to complete the phase measurements. The three main changes made to the setup are (i) the replacement of the two Keithleys previously used as voltage sources to control the piezo mirror and the voltage being applied to the chip with a function generator (ii) using a photodiode rather than a Spectrometer to collect the output signal used to measure the phase shift achieved by the device and (iii) exchanging the piezo mirror used in the previous phase shift measurements with one which required lower voltages to operate. An oscilloscope was used to visualize the voltage signals sent by the function generator to the piezo mirror and chip. The light signal measured by the photodiode was also converted by the photodiode into an electrical signal and sent to oscilloscope so that it could also be displayed on its screen for real-time observation. Figure 6.2 part (a) shows the function generator and how one can change the characteristics of the function of voltage applied to the different parts of the setup including the shape, frequency and amplitude. Figure 6.2 part (b) shows a photo of the oscilloscope where on the screen, the dashed orange and the solid pale blue lines represent the voltage functions generated by the function generator and sent to the chip and piezo mirror. The dashed blue lines show the signal collected by the photodiode at 0V and at the maximum voltage applied to the device by the function generator. As this signal was visualized in real-time by the oscilloscope, it was possible to observe how stable the phase shift between the two interference curves for the two different applied voltages was during the experiment.

From observing the interference curves on the oscilloscope screen in real-time, some noise seemed to resonate at a frequency of 50 Hz that made the amplitudes and relative positions of the two interference curves drift. To remove this noise from the measurement results, the phase measurement was conducted in a time period of 2 ms. In theory, making the time period even faster than 2ms would have given more precise phase measurements as it

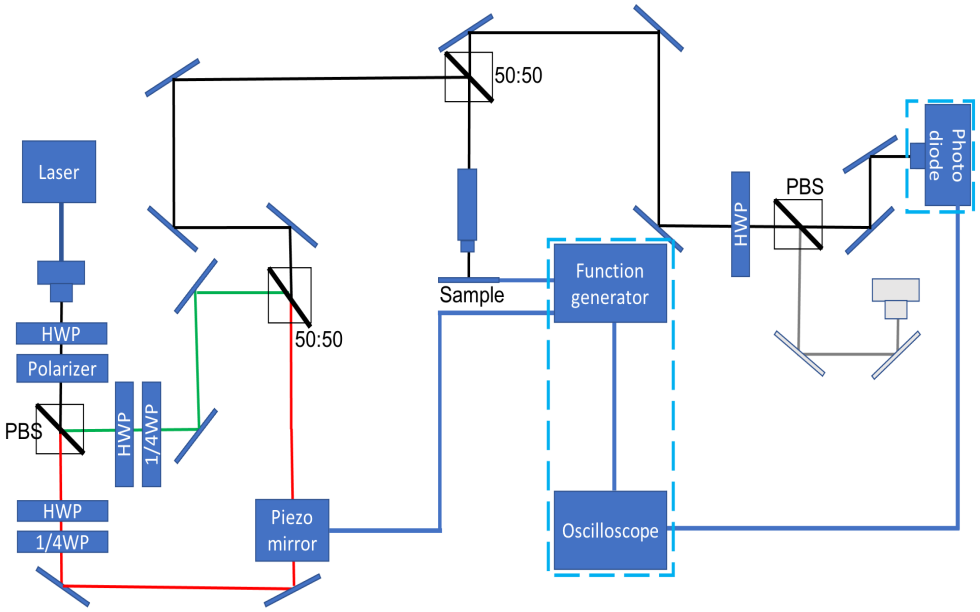

Figure (6.1) This figure shows a schematic diagram of the improved setup used to measure the phase shift properties of the devices on the same chip used to take the measurements discussed in section 6.1. As in the setup used to take the measurements in section 4.4, the light is coupled through the two input ports of the device of the chip inside the cryostat. A piezo mirror is used as an external phase shifter to apply a phase difference between the 'red' and 'green' paths (the two inputs to the device) to create interference curves which are used to calculate the phase shift achieved by the device when a 7V is applied to the chip compared to 0V. The first of the differences from the setup in Figure 4.4 is the implementation of one function generator rather than two Keithleys to control the piezo mirror as well as the voltage applied to the chip in the cryostat. The second difference is the method by which the signal output from the device is collected. In this setup a photodiode is used instead of a Spectrometer which is connected,along with the function generator, to an oscilloscope which displays the functions generated by the function generator as well as the signal collected by the photodiode in real-time. As the measurement time using this setup is only 2 ms, the need for the feedback system involving a power meter and PID is no longer necessary. This is because power drift is no longer considered to affect the phase shift measured as this type of drift is slower than the 2 ms time frame for the phase measurement.

would have decreased the possibility of drift affecting the phase shift measured even more. However, due to limitations of the speed at which the function generator could apply a linear triangular ramp function of voltage to the piezo mirror, a faster time period for the phase shift measurement was not possible. This is because if the voltage had not changed in a linear manner, it would have made it very difficult to extract the transition of phase shift as a function of applied voltage. Considering that the time frame of the phase measurements conducted in section 5.3.2 was in minutes, the time period of 2 ms with the improved setup is a considerable improvement. It was expected that as there was less time for drift to occur, the variation in the measured phase shift for the same change in applied voltage to the chip would be less. To test if this was the case, the phase shift caused by the change in applied voltage was measured by extracting the interference curves from the recorded data of the photodiode when the voltages applied to the device were 0V and 7V. This data was then filtered through a lowpass filter to eliminate noise and fitted with a sin function of this form:

$$a + b \cdot \sin(cx + \text{off}) \tag{6.1}$$

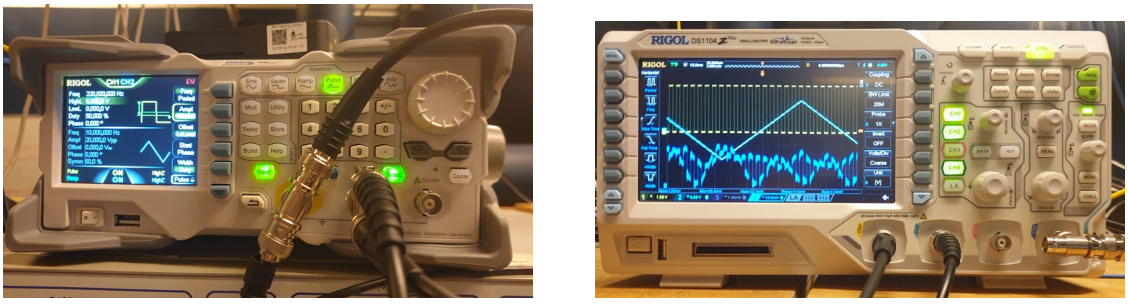

(a) (b)

Figure (6.2) This figure shows photographs of two of the new elements added to the experimental setup (a) This is a photograph of the function generator used to control the voltage applied to the piezo mirror in the setup and the chip. On the screen of the function generator one can see pictured the Tukey function (yellow) used to drive the devices on the chip and the triangular function (blue) used to drive the piezo mirror. On the screen one can also see how one can change different properties of the functions including the frequency and amplitude. (b) In this photograph one can see the oscilloscope used to display not only the functions generated by the function generator showing in figure a (blue and orange solid lines) but also the output of the photodiode, where the settings are as such, that the two overlapping dashed blue interference curves of two different amplitudes and phases, are the ones produced when there is 0V and, in this specific case, 7V to the chip. These dashed blue interference curves are produced in real-time.

Wavelength 945[nm] 6V	Wavelength 945[nm] 7V	Wavelength 940[nm] 7V	Wavelength 949[nm] 7V
41.6 ± 5.5 [degrees]	61.0 ± 1.6 [degrees]	72.5 ± 1.5 [degrees]	154.5 ± 3.7 [degrees]

Table (6.1) This table contains the average phase shifts measured by using the improved setup for three different wavelengths and two different voltage ranges. The error is the standard deviation of the phase shift measurements. The decrease in these values from phase experiments 1 and 2 show the improved consistency in the measurement of the phase shifts using this new method.

Here, the parameter 'off' for the two fitted functions was the one of interest for finding the difference in phase between the two fitted functions. The parameters a,b and c were set as free parameters for the fits. Figure 6.3 shows examples of the fitting of the interference curves taken at 3 different wavelengths ((a) 940nm, (b) 945nm and (c) 949nm) of the CTL laser used in the measurement where the maximum and minimum voltages applied to the chip in each case are 7V and 0V respectively. The measurements were obtained on the same device as the 'hero' device of section 5.2 (device number 74). For each wavelength, the phase shift measurement from 0V to 7V was measured 8 times consecutively, and in the case of wavelength 945nm, the phase shift was also measured for a maximum applied voltage of 6V 8 times. From the measurements, the averages and standard deviations for the different wavelengths and voltage ranges were recorded and can be found in Table 6.1.

This table shows that the standard deviations of the measured phase shifts for all three wavelengths are much smaller than those of the phase shifts measured using the phase experiment 1 and 2 methods. This indicates that this new method of measuring the phase shift is more consistent in its phase shifts measurements. This is in accordance with the prediction that, reducing the time frame of the measurement would reduce that time period where random phase drift could occur and hence affect the measurement of the phase shift. What is of further interest in the results table is that the average phase shift for

the measurement conducted at wavelength 945nm (the same wavelength used in the phase experiments described in section 5.3.2) is 17.9 degrees larger than the average phase shift measured for the same device (device number 74) using the phase experiment 1 method and 21.3 degrees larger phase experiment 2 method from section 5.3.2. One possible reason for this could be that the device was affected by being taken in and out of the cryostat, and the change in pressure it consequently was exposed to, in between the 2 months that passed between the measurements taken with the improved setup and those discussed in section 5.3.2. Another possible, but not mutually exclusive, reason could be that the large variance of the phase measurements reported in section 5.3.2 could have skewed the average value of the recorded phase shift. This could indicate that, had the improved setup been used instead of the original method, at that time those measurements had been conducted, then (i) those measurements would have been more consistent and (ii) the average phase shift value would have been a more reliable value to compare with the expected phase shift generated by the simulation and the average phase shift generated two months later. Considering, however, that the average phase shifts produced for device number 74 using phase experiments 1 and 2 were within -0.9 and 2.5 degrees of the simulated phase shift respectively, it would seem more likely that it was the functionality of the device which changed within the 2 months it was not used for phase measurements and affected the phase shift that it generated. One finding that does seem consistent with the results of phase experiments 1 and 2 of device number 74 is that the phase shift produced by 7V volts is consistently larger than that produced by 6V which is encouraging.

The average values of the phase shifts produced when using wavelengths 940nm and 949nm suggest that the phase shift produced by the device is sensitive to the wavelength of the CTL which is consistent with the predictions of the simulation which predict phase shifts of 91.77 and 156.28 degrees respectively. Both, though particularly the phase shift simulated at wavelength 940nm, are different from the average phase shifts recorded in Table 6.1. However, as discussed above, the values generated by the simulation after the 2 months break no longer match those generated by the device as the device may have been affected in some way to change its phase shifter properties so this was to be expected. Despite the simulation not being a good predictor of the phase shift generated by device, it can still be used to identify the theoretical effect that using different wavelengths of light has when performing the same phase shift measurement on a device.

6.2 Outlook on further characterization nano-mechanical phase shifters and unitary gates

For a unitary gate made of a cascaded nano-mechanical photon router and phase shifter to make any arbitrary rotation of a qubit, the phase shifter must be able to achieve a 180 degrees phase shift. It appears from Table 5.1 where the phase shifts measured by the devices tested in this project at wavelength 945nm are recorded, that none of these devices were close to reaching such a large phase shift. To achieve such a large phase shift, a voltage range that goes beyond the limit where the pull in effect occurs would most likely be needed. In the future therefore, one could consider modifying the design of the nano-mechanical phase shifters to increase the coupling length of the device whilst keeping everything else about the devices constant. This would increase its beam splitter properties

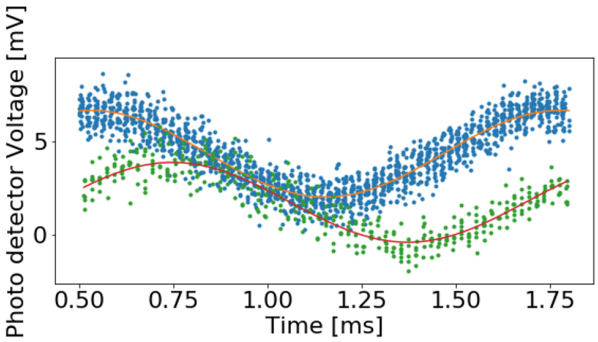

(a)

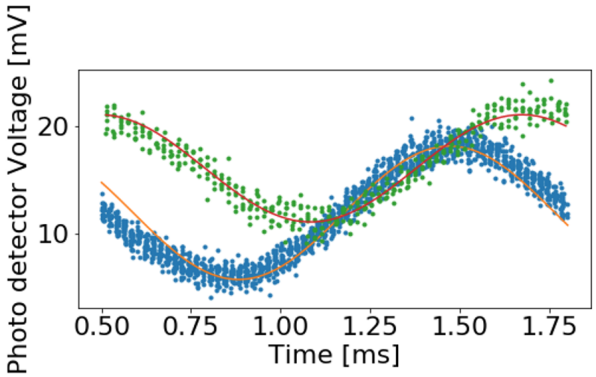

(b)

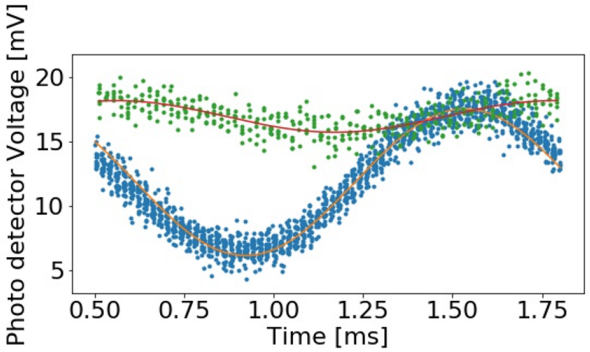

(c)

Figure (6.3) These three figures represent the snippet of the two inference curves produced at 0V and 7V for three different wavelengths of a CTL laser (940nm, 945nm and 949nm). The yellow and red lines represent the sin curves used to fit the data points produced by the two different voltages (0V (yellow) and 7V (red)). By extracting the difference in phase from these two fits, the phase shift produced by the change in applied voltage to the chip could be extracted. On the y axis one can see the voltage output produced by the photodiode used to measure the interference and on the x axis the time period in which the voltage output was recorded. This time period corresponds to the time period where the voltage ramp applied to the piezo mirror was linear. The wavelengths of the CTL laser used for (a) was 940nm, for (b) 945nm and for (c) 949nm

and hence decrease the waveguide separation range needed to produce a large phase shift. There are however certain difficulties involved with increasing only the coupling length when it comes to fabrication. These include the increased fragility of the device which make it more prone to breaking and the increased risk of the waveguides having rough edges and being non-uniform. The issue with increased fragility is the smaller of these two issues as

(discussed in section 4.1) even if the devices were more fragile with longer coupling lengths, then the yield would probably still be good. The bigger issue is that the devices will be more non-uniform which will make it much more difficult to predict the phase shift which the device would produce as coupled-mode theory assumes no loss in the system and thus would not be an accurate way to model the device. Instead more complex 3D models which take roughness and loss into account could be made with COMSOL to model the behaviour of the nano-mechanical phase shifters. This same 3D COMSOL model could also be used to check what wavelength of light would improve the range of phase shift the most as it appears in Table 6.1 that for device number 74, when the wavelength of the CTL was 949nm a much larger phase shift (close to 180 degrees) was generated than when the wavelength was 945nm.

Furthermore, once these new phase shifters have been characterized with the optimal method for measuring phase shift described in section 6.1, then the cryostat which the chip with the nano-mechanical phase shifters is in should have the temperature adjusted to 10K. This would (i) test the durability of the devices by observing if they could cope with this process without breaking (ii) test if single photons emitted from QDs embedding in the structures could be coupled through and manipulated by the phase shifters, and finally (iii) test if at low temperature the devices produce the same phase shifts as at room temperature.

Having thus fully characterized the properties of the nano-mechanical phase shifter, the next step would be to combine it with a nano-mechanical photon router on a chip and test if it is possible to control both of these parts of the unitary gate to produce an arbitrary rotation of a qubit. One likely challenge is the difficulty in fabricating a directional coupler with identical waveguide widths. This is exemplified in Table 5.1 where both devices 73 and 74 which were supposed to be symmetric but instead both exhibited phase shifter qualities which indicated an asymmetry in their waveguide widths. This would mean that the nano-mechanical photon router would have phase shifter properties which would cause the qubit to rotate differently than desired. It will therefore be important to establish a method of predicting and compensating for this extra added phase.

6.3 Conclusion

The aim of this project was to work towards developing a reconfigurable nano-mechanical unitary gate. This aim has been successfully met by demonstrating not only that an asymmetric directional coupler can be used as a phase shifter but also that the phase shift that it produces can be changed by altering the voltage applied to the chip which is a crucial element needed to develop the unitary gate modelled in this project. As a first step to reach this goal, the project began with simulations based on coupled-mode theory to test if in theory, an asymmetric directional coupler could be used as a phase shifter and if combined with a nano-mechanical photon router, could perform any arbitrary rotation of a qubit. After investigating this, further simulations were then run using COMSOL to explore how to optimise the design of the phase shifter before they were fabricated. These devices were then inserted into a cryostat and characterized at room temperature which required several different experimental setups to be constructed. It was shown that by decreasing the time duration of the phase shift measurement, the precision of the phase shift was greatly improved. This was a very important next step towards developing a reconfigurable unitary

gate. This is because by being able to serially replicate the same phase shift when applying the same voltage, it is easier to control the rotation of the qubit. Lastly, simulations were run to calculate the expected phase shift that the phase shifters should have achieved in the voltage range tested and compared the phase shift measured for the different phase shifters. These comparisons made clear the issues with the fabrication process of the devices which rendered the coupled-mode theory an inaccurate theory to describe the behaviour of the phase shifters. These issues of non-uniformity, loss and difference in waveguide width from the design parameters due to fabrication errors are important to address to better predict the phase shifts which the phase shifters are expected to achieve. Other modifications as discussed in section 6.2 could also be tested to increase the range of phase shifts achievable by the phase shifter within a certain voltage range as none of the devices tested in this project were able to produce a phase shift close to 180 degrees. This improvement to the design of the phase shifter would be necessary to perform an arbitrary rotation of a qubit as shown in Figure 2.5. In conclusion, the added value of this project is that it has shown that applying a voltage to an asymmetric directional coupler induces a phase shift which can be measured and is statistically different from phase drift in the setup. This knowledge can be applied to future experiments where similar devices to those used in this project are combined with a nano-mechanical photon router on the same chip and test if the theoretical unitary gate put forward in this project would work in reality.

Chapter 7

Appendix

7.1 Methods of characterizing nano-mechanical phase shifters.

7.1.1 Method: Interference measurement

The interference measurements were performed in a step-wise fashion. The following bullet points below outline the main steps. It should be noted that after the first step, the remaining steps are all automated and run through a MatLab code.

1. Balance counts at output as the devices are supposed to be symmetric to ensure that the input power was equal at the two input ports to maximize visibility
2. Start measurement: take spectrum measurement with Spectrometer and integrate over the spectrum (delta function) to get one measurement number of the peak of counts at one voltage applied to the device.
3. Repeat this measurement 9 more times to test how in this time frame the peak drifts in value.
4. After 10 measurements, increase voltage applied to piezo mirror by 10V.
5. Repeat 10 spectrum measurements.
6. Repeat steps 4 and 5 until maximum voltage (160V) applied to piezo mirror has been reached.
7. Repeat 10 spectrum measurements one final time.
8. Interference measurement is over after 1 minute.

7.1.2 Method: Transmission and reflection measurements

1. Lock the PID at 7 μ watts and block one of the input arms.
2. Rotate the HWP before the collection fibres to maximise the collection at the output connected to the Spectrometer.
3. Adjust the positions of the mirrors at the input, before the light goes into the cryostat to maximise the peaks of the spectrum and hence also the amount of light being coupled through the device.

4. Start measurement through MatLab. Take spectrum measurement with the Spectrometer and increase the voltage applied to the device by 0.2 V before taking another spectrum measurement.

5. The MatLab code continues this series of measurements up to 7V at which point it takes one final spectrum measurement before bringing the voltage applied to the device back to 0 V and the code finishes.

6. The Spectrometer is disconnected from the output that has been measured and connected to the second output.

7. The HWP is rotated once again to maximize the output collected at this second output.

8. Rerun the code for taking spectrum measurements for the same series of applied voltages as described in earlier steps.

9. The input arm which is blocked is now switched and the transmission and reflection measurements at the two outputs are repeated for this second input.

10. Once these 4 measurements are completed, the stage controlling the position of the chip is moved to maintain the relative positions of the input and output spots whilst changing the device which is aligned with them. This makes it easier to optimise the coupling of the light through new devices.

11. The mirrors at the input and output are adjusted to maximise the output of the Spectrometers whilst the power is locked at 7 μ watts.

12. Steps 1 to 9 are repeated for the new device.

7.1.3 Method: Phase shift measurement

1. Lock the PID at 7μwatts

2. Rotate the HWP before the collection fibres to maximise the collection at the output connected to the Spectrometer.

3. Complete interference measurement as described in 4.3.1 and then set the voltage applied to the piezo mirror back to 0V.

4. Using Keithley 2, ramp up to an output voltage of 1V applied to the chip in steps of 0.2V

5. Complete interference measurement as described in 4.3.1 and then set the voltage applied to the piezo mirror back to 0V.

6. Using Keithley 2, ramp up to an output voltage of 6V applied to the chip in steps of 0.2V

7. Complete interference measurement as described in 4.3.1 and then set the voltage applied to the piezo mirror back to 0V.

8. Using Keithley 2, ramp up to an output voltage of 7V applied to the chip in steps of 0.2V

9. Complete interference measurement as described in 4.3.1 and then set the voltage applied to the piezo mirror back to 0V.
10. Using Keithley 2, using the cool down function in MatLab, ramp down to an output voltage of 0V applied to the chip.
11. Complete interference measurement as described in 4.3.1 and then set the voltage applied to the piezo mirror back to 0V.
12. The phase measurement for one output of the device is now complete. Repeat steps 1 and 11, 5 more times for examination later on and to test how reproducible the results of the phase measurement are.
13. Connect the Spectrometer to the second output and rotate the HWP infront of the collection fibre so as to maximise the collection at the second output.
14. Repeat steps 2 to 12 for this second output.

7.2 Examples of raw data of interference measurement

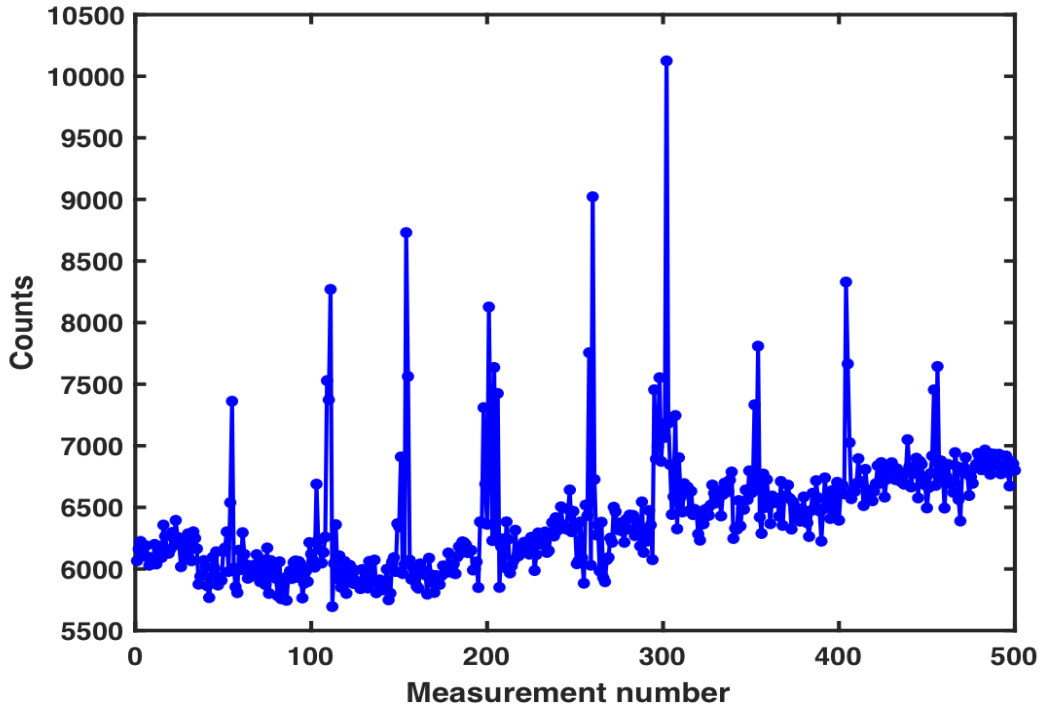

Figure (7.1) This figure shows how the power measured by the spectrometer when one of the input beams is blocked and only the input beam which passes through the thin piece of glass is measured. One can clearly identify the points where the glass has been rotated as this causes sharp peaks in the counts measured by the spectrometer. This indicates that the position of the input beam is off centre to the glass and why another form of external phase shifter had to be identified.

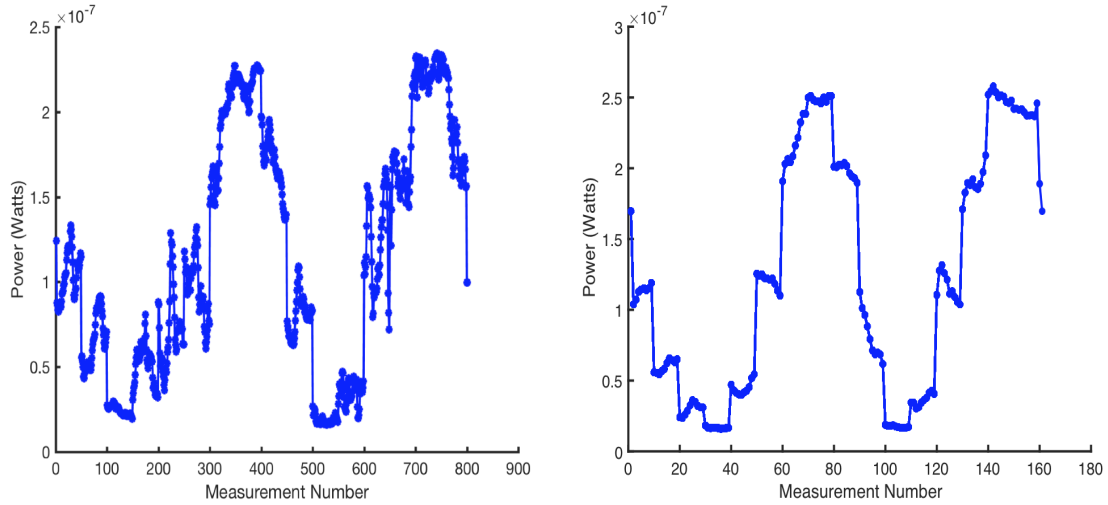

Figure (7.2) This figure shows raw data of two different interference measurements where one took 50 measurements at each different applied voltage to the piezo mirror and the other one took only 10. One can see that there is far less power drift when only 10 measurements are taken rather than 50.

7.3 Different devices table Chip 2

Device number	Difference in Waveguide width [nm]	Initial gap size [nm]	coupling length [μm]
73	0	150	35
74	0	124	35
79	2	100	35
80	2	80	35
82	4	80	35
87	6	100	35
90	8	124	35
96	10	80	35

Table (7.1) This table shows the design parameters of the devices tested for this project where both types of phase experiments were performed.

7.4 Method of analysing phase experiment measurement for extracting voltage induced phase shift

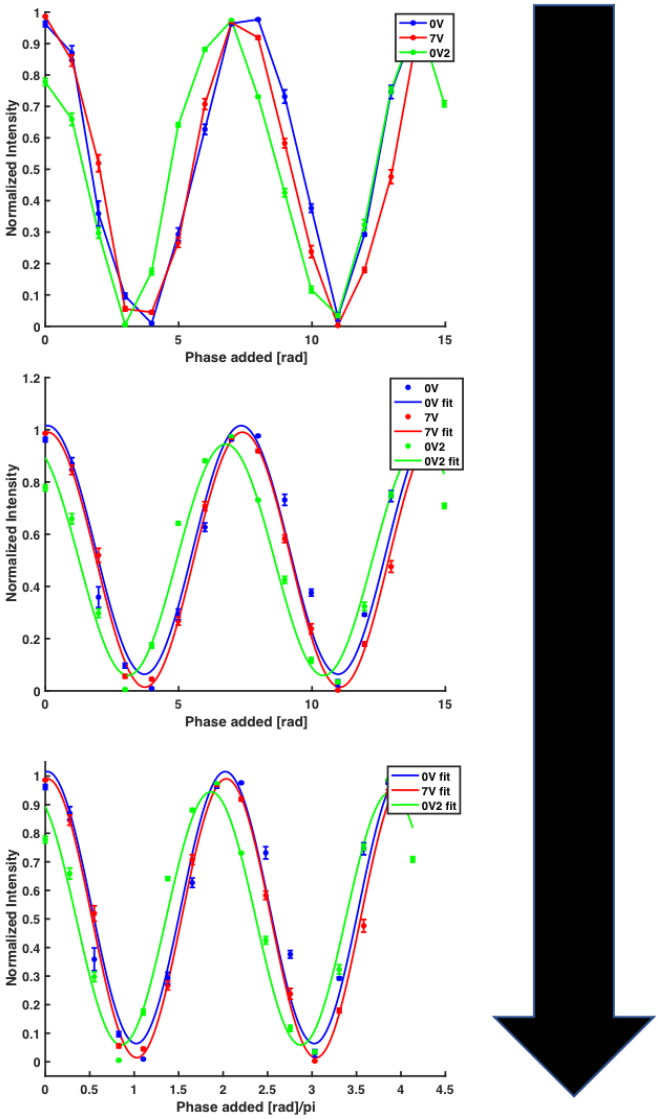

Figure (7.3) This figure shows a step-by-step guide of the method used to extract the phase shifts listed in Table 5.1 from raw data collected during an interference measurement like that shown in 7.2. The first step was to take the average value of the spectrum measurements taken at each of the applied voltages to the piezo mirror for each of the interference measurements performed at voltage applied to the chip. A relation between voltage applied to the piezo mirror and the phase added as a result to the input beam was used to plot the interference curves consisting of the averaged intensities as a function of phase added. These points were then fitted with a sin curve as shown in the second figure which was then renormalized as shown in the third figure. It was from this third plot that the peaks of the sin curves were found and the phase shift was extracted.

7.5 QQ plots for phase measurements

This section shows the qq plots plotted for the different data sets collected when conducting the different phase shift measurements in this project. These plots were used to demonstrate that the data sets were not normally distributed and hence limited the possible statistical tests that could be used to test if the voltage applied to the devices induce a phase shift which is statistically significantly larger than the phase drift in the setup. The test used in the project based on these qq plots was the Wilcoxon rank sum test.

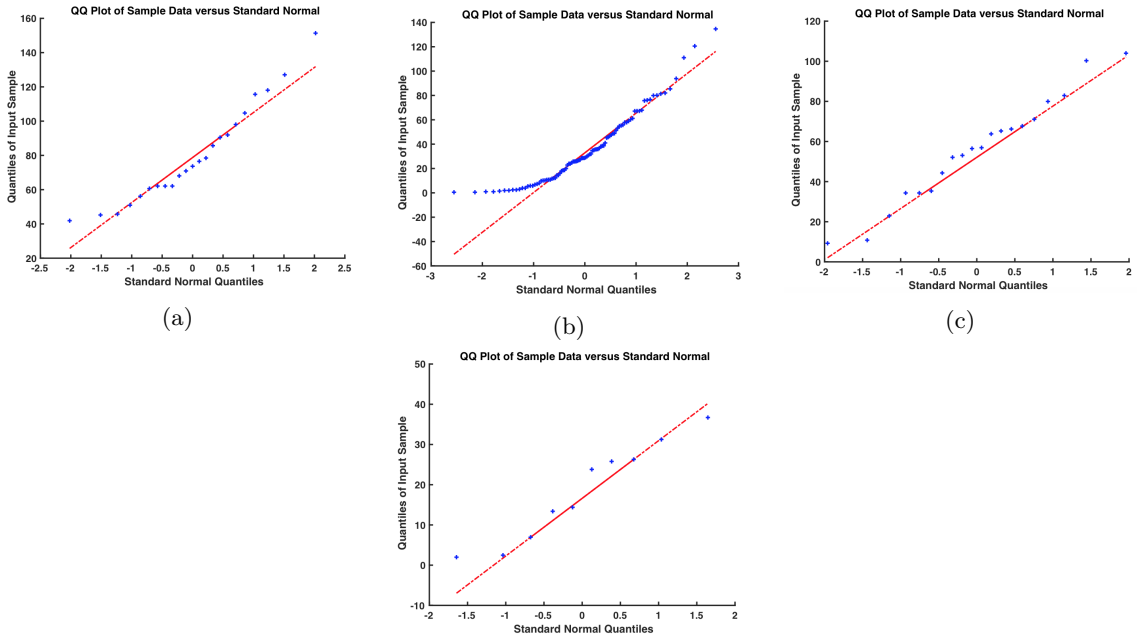

Figure (7.4) (a) QQ plot for phase shifts measured using phase experiment 2. (b) QQ plot for phase drift measured using phase experiment 2. (c) QQ plot for phase shifts measured using phase experiment 1. (d) QQ plot for phase shifts measured using phase experiment 1 when no voltage was applied for the duration of the experiment.

7.6 Transmission spectrum of a nanobeam

From the transmission of light through a nanobeam, it is possible to more easily observe why the transmission wavelengths below 930nm and above 970nm could be discarded in the transmission and reflection measurement analysis for calculating the SR of the devices tested in this project.

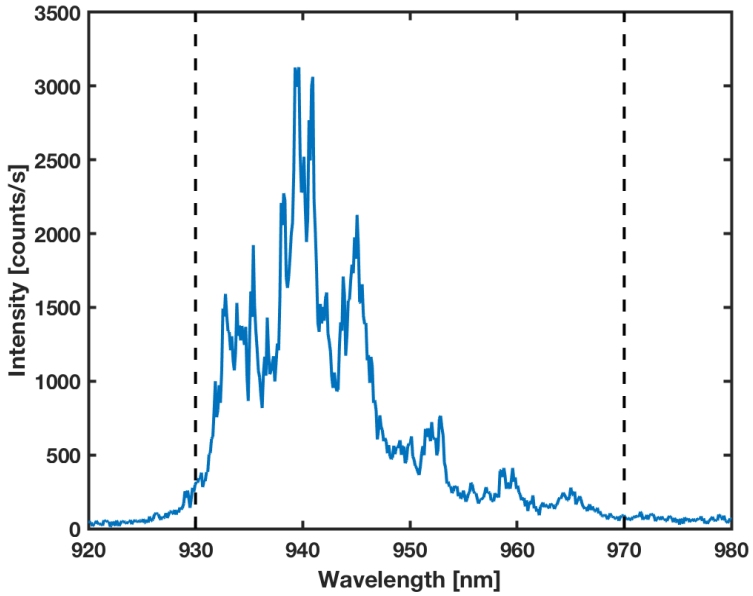

Figure (7.5) This figure shows the transmission through a nanobeam present on chip 2, and how there is limited transmission through the grating of the devices when the wavelength of light is either less than 930nm or more than 970nm, and thus, why these two wavelengths can act as cut off points for the SR analysis in section 5.2

7.7 Second derivative of SR for an asymmetric directional coupler

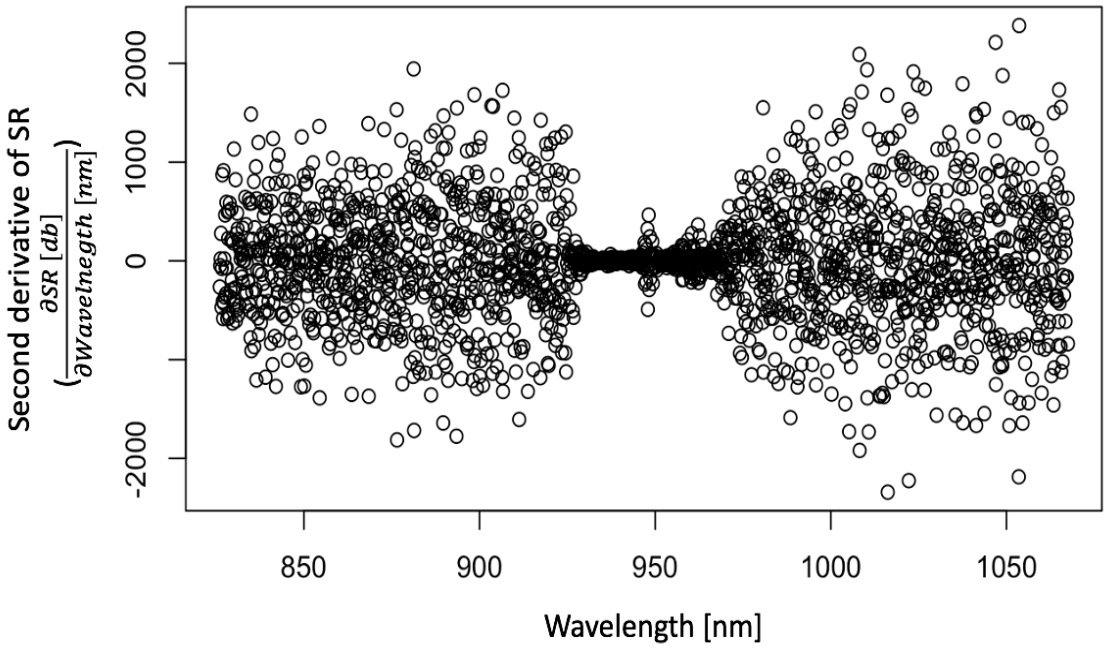

Figure (7.6) This figure shows the second derivative of an asymmetric directional coupler plotted as a function of wavelength. It is clear from this plot that only SR data within the wavelengths 930nm and 970nm should be considered in this project when the analysing devices.

Bibliography

[1] F. Arute, K. Arya, *et al.*, "Quantum supremacy using a programmable superconducting processor," *Nature*, vol. 574, 2019.

[2] M. Reck and A. Zeilinger, "Experimental realization of any discrete unitary operator," *Phys.Rev.Lett*, vol. 73, 1995.

[3] N. C. Harris, Y. Ma, *et al.*, "Efficient, compact and low loss thermo-optic phase shifter in silicon," *Opt.Express*, vol. 22, 2014.

[4] P. Lodahl, S. Mahmoodian, *et al.*, "Interfacing single photons and single quantum dots with photonic nanostructures," *Rev.Mod.Phys*, vol. 87, 2015.

[5] R. J. Warburton, "Single spins in self-assembled quantum dots," *Nature Mater*, vol. 12 483, 2013.

[6] C. L. Paolo Minzioni *et al.*, "Roadmap on all-optical processing (quantum-information processing with single photons generated by quantum dots)," *J.Opt.*, vol. 21, 2019.

[7] M.Bayer, G.Ortner, *et al.*, "Fine structure of neutral and charged excitons in self-assembled in(ga)as/(al)gaas quantum dots," *Phys.Rev.B*, vol. 65, 2002.

[8] C. Santori, D. Fattal, *et al.*, "Indistinguishable photons from a single-photon device," *Nature*, vol. 419, 2002.

[9] G. *Kiršanskė*, *Electrical control of excitons in semiconductor nanostructures: from quantum dots in photonic-crystal devices to the exciton Mott transition in coupled quantum wells*. PhD thesis, University of Copenhagen, 2016.

[10] L. Midolo, A. Schliesser, *et al.*, "Nano-opto-electro-mechanical systems," *Nature Nanotechnology*, vol. 13, 2018.

[11] M. Eichenfield, J. Chan, *et al.*, "Optomechanical crystals," *Nature*, vol. 462, 2009.

[12] C. Papon, X. Zhou, *et al.*, "Nanomechanical single-photon routing," *Optica*, vol. 6, 2018.

[13] H. A. Haus and W. Huang, "Coupled-mode theory," *Proceedings of the IEEE*, vol. 79, 1991.

[14] C. Papon, "Nano-electro-mechanical switches for quantum photonic applications: Fabrication and characterization," Master's thesis, University of Copenhagen, 2018.

[15] E. Hecht, *Optics (fifth edition) (Chapter 13)*. Harlow Essex England: Pearson, 2017.

[16] J. H. Milonni and P. W. Eberly, *Laser physics (Pages 282-285 and 320)*. New Jersey: John Wiley & Sons. Inc, 2010.

[17] C. C.Gerry, P. L.Knight, *et al.*, *Introductory Quantum Optics (Page 224)*. Shaftesbury Road Cambridge CB2 8BS United Kingdom: Cambridge University Press, 2005.

[18] Chin-Lin, *Foundations for Guided-Wave Optics (Chapter 6)*. New Jersey: John Wiley & Sons. Inc, 2007.

[19] K.F.Riley, *Mathematical methods for physics and engineering (Pages 297-300)*. Shaftesbury Road Cambridge CB2 8BS United Kingdom: Cambridge University Press, 2006.

[20] J.L.O ' Brien, G.J.Pryde, *et al.*, "Quantum process tomography of a controlled-not gate," *Phys.Rev.Lett*, vol. 93, 2004.

[21] A.M.Childs, I.L.Chuang, *et al.*, "Realization of quantum process tomography in nmr," *Phys.Rev.A*, vol. 64, 2001.

[22] M.W.Mitchell, C.W.Ellenor, *et al.*, "Diagnosis, prescription, and prognosis of a bell-state filter by quantum process tomography," *Phys.Rev.Lett.*, vol. 91, 2003.

[23] S. Rahimi-Keshari, M. A. Broome, *et al.*, "Direct characterization of linear-optical networks," *Optics Express*, vol. 21, 2013.

[24] P. Instrumente, "Displacement modes of piezoelectric actuators," Last accessed 2021-09-19. `https://www.piceramic.com/en/piezo-technology/properties-piezo-actuators/displacement-modes/`.

[25] Physik Instrumente, *PICA Thru Ring Actuators*, PI_Datasheet_P-010xxH-P-025xxH 2016.

[26] S. physics, "3900s cw tunable ti:sapphire lasers," Last accessed 2021-09-28. `https://www.spectra-physics.com/f/3900s-ti-sapphire-laser`.

[27] T. photonics, "Continuously tunable laser," Last accessed 2021-09-28. `https://www.toptica.com/products/tunable-diode-lasers/ecdl-dfb-lasers/ctl/`.

[28] NKT Photonics, *SUPERK FIANIUM-Pulsed white light laser platform*, SuperK FIANIUM_20210618 2021.

[29] F. Yang, G.-F. Wang, *et al.*, "Influence of surface energy on the pull-in instability of electrostatic nano-switches," *Journal of Computational and Theoretical Nanoscience*, vol. 10, 2012.

[30] D. LeBlanc, *Statistics: Concepts and Applications for Science (Chapter8)*. Sudbury Massachusetts: Jones and Bartlett Publishers, 2004.

[31] M. P. Fay and M. A. Proschan, "Wilcoxon-mann-whitney or t-test? on assumptions for hypothesis tests and multiple interpretations of decision rules," *Stat Surv*, vol. 4, 2010.